AB INITIO STUDY OF NITROGEN BASED SOLID ENERGETIC MATERIALS

Thesis submitted in partial fulfillment for the award of the degree of

DOCTOR OF PHILOSOPHY

By

RAMESH BABU KUNCHALA

ADVANCED CENTRE OF RESEARCH IN HIGH ENERGY MATERIALS

UNIVERSITY OF HYDERABAD, HYDERABAD 500046

ANDHRA PRADESH, INDIA

NOVEMBER 2013

DECLARATION

I Ramesh Babu Kunchala hereby declare that the matter embodied in the thesis entitled "Ab initio study of nitrogen based solid energetic materials" is the result of investigation carried out by me in the ACRHEM, University of Hyderabad, Hyderabad, India under the supervision of Dr. G. S. Vaitheeswaran. I also declare that it has not been submitted previously in part or in full to this university or any other university or institution for the award of any degree or diploma.

RAMESH BABU KUNCHALA

University of Hyderabad
07-November-2013.

UNIVERSITY OF HYDERABAD
Advanced Centre of Research in High Energy Materials (ACRHEM)

Dr. G. S. Vaitheeswaran
Assistant Professor

07th November 2013

CERTIFICATE

This is to certify that the thesis entitled "Ab initio study of nitrogen based solid energetic materials" by Ramesh Babu Kunchala in partial fulfillment of the requirements for the award of degree of Doctor of Philosophy is a bonafide research work carried out by him under my supervision and the same has not been submitted elsewhere for award of any degree or diploma.

Dr. G. S. Vaitheeswaran

(Supervisor)

Director

ACRHEM

UNIVERSITY OF HYDERABAD

Doctoral Thesis

AB INITIO STUDY OF NITROGEN BASED SOLID ENERGETIC MATERIALS

Author:
RAMESH BABU KUNCHALA

Supervisor:
Dr. G. S. VAITHEESWARAN

A thesis submitted in fulfilment of the requirements for the degree of Doctor of Philosophy

in the

Research Group Name
ACRHEM

November 2013

Declaration of Authorship

I, RAMESH BABU KUNCHALA, declare that this thesis titled, 'AB INITIO STUDY OF NITROGEN BASED SOLID ENERGETIC MATERIALS' and the work presented in it are my own. I confirm that:

- This work was done wholly or mainly while in candidature for a research degree at this University.
- Where any part of this thesis has previously been submitted for a degree or any other qualification at this University or any other institution, this has been clearly stated.
- Where I have consulted the published work of others, this is always clearly attributed.
- Where I have quoted from the work of others, the source is always given. With the exception of such quotations, this thesis is entirely my own work.
- I have acknowledged all main sources of help.
- Where the thesis is based on work done by myself jointly with others, I have made clear exactly what was done by others and what I have contributed myself.

Signed: _____

Date: _____

Declaration of Authorship

I, RAMESH BABU KUNCHALA, declare that this thesis titled, 'AB INITIO STUDY OF NITROGEN BASED SOLID ENERGETIC MATERIALS' and the work presented in it are my own. I confirm that:

- This work was done wholly or mainly while in candidature for a research degree at this University.
- Where any part of this thesis has previously been submitted for a degree or any other qualification at this University or any other institution, this has been clearly stated.
- Where I have consulted the published work of others, this is always clearly attributed.
- Where I have quoted from the work of others, the source is always given. With the exception of such quotations, this thesis is entirely my own work.
- I have acknowledged all main sources of help.
- Where the thesis is based on work done by myself jointly with others, I have made clear exactly what was done by others and what I have contributed myself.

Signed: _____

Date: _____

Thanks to "The Nature"

Ramesh Babu Kunchala

Acknowledgements

It is great pleasure for me to acknowledge the people whose blessings and support made to complete my doctoral studies. I express my sincere thanks to each one who had helped me directly or indirectly towards my successful educational career over these years.

First of all, I would like to express deep and sincere gratitude to my thesis supervisor **Dr. G. S. Vaitheeswaran** for his guidance throughout the research period. I sincerely appreciate his support, suggestions and constant encouragement throughout these years. I have learnt the true colours of life both academically and socially from him over these years. It gives me immense pleasure to feel proud and honour for me to be his direct first Ph.D student in ACRHEM. Thank You Sir.

I am grateful to Prof. Surya P. Tewari, former Director of ACRHEM, for his ceaseless encouragement towards my research work. I am extremely thankful to him for sharing his vast knowledge on the subject of quantum mechanics. The kind of motivation he has given over these years is unforgettable. The great teacher I have ever seen in my educational career. Thank You very much Sir.

At this moment, I take the opportunity to thank my Doctoral Committee member Prof. K. P. N. Murthy, School of Physics, for fruitful suggestions and appreciation during the DC meetings. I am extremely happy to extend my humble thanks to Dr. V. Kanchana, IITHyderabad, for her valuable suggestions and motivation towards my scientific enlightenment. Thank You very much Madam for being source of inspiration. I thank Prof. C. S. Sunandana, School of Physics and Prof. M. C. Valsa Kumar, School of Engineering Sciences and Technology for their critical suggestions on subject and the scientific communications.

I am extremely happy and gifted to have wonderful ACRHEM faculty members. My sincere thanks to Dr. P. Prem Kiran, Dr. G. Manoj Kumar, Dr. B. Ashok, Dr. S. VenuGopal Rao, Dr. Anil K. Chaudhary, Dr. K. Muralidharan for inculcating scientific thoughts during course work. I thank Dr. D. K. Setuva, Director ACRHEM for providing the necessary facilities and constant encouragement.

My sincere thanks to Dr. S. Lebègue, Centre National de la Recherche Scientifique France, Prof. A. Svane, Aarhus University Denmark and Prof. S. Auluck, National Physical Laboratory Delhi for their valuable scientific discussions.

It is great pleasure to express my sincere thanks to the office staff of ACRHEM Mr. Sadik Hussain, Assistant Registrar, Mr. G. Subhash, Mr. T. Satya Narayana Rao, Librarian, Mr. K. Venkata Subbaiah, PA to Director, Mr. D. Prabhakar, Mr. G. Mahesh, Mr. Sk. Rafi, Mr. A. Anantha Rao, Mr. K. Ramakrishna, Mr. V. Sai, Mr. G. Nagaraj for their support on office related matters during these years. Thank You all the people.

The financial support for my research work in ACRHEM through DRDO is gratefully acknowledged.

I am lucky to have good friends who really supported me and encouraged to complete my Ph.D successfully. I would like to express my whole hearted thanks to my friends Ch. Anjaneyulu, Dr. G. Srinivasa Rao, B. Venkata Ramaiah, K. Srinivasa Nehru, Dr. B. Kiran Kumar, Allu Rambabu, Dr. A. Rambabu, P. V. Anil Kumar, B. Babu, Dr. M. Bala Murali Krishna, Bala Gangadhar, Suresh and Soma sekhar.

I take the opportunity to recollect the wonderful moments shared with my friends Dr. V. V. Gopala Krishna Inavalli, Dr. V. Sri Ramulu, Dr. M. Durga Rao, K. Mohan Kumar, Dr. Ch. Bheema Lingam, Dr. Vikas D Ghule, Dr. Sudha Nirmala, Dr. M. Hanumantha Rao, Debasis Swain, S. Sreedhar, P. T. Anusha, P. Gopala Krishna, M. Venkatesh, M. Ashwin Kumar, N. Tarun Bharath, Rajesh, Kishore, Naveen and Seshadri during the stay in UoH over these years.

I extend my thanks to lab mates in ACRHEM and IITHyderabad friends for their help in so many occasions.

Thanks to my friends B. Suresh Raju, P. Srinivasa Reddy, B. Raghu, Dr. U. Paul Kumar, Dr. Purna Chandra Rao, Ch. L. Rajesh, KCS Anand for their constant support.

I thank Sri Manam Papa Rao garu, Sri Nuvvula Krishnamurthy garu, Sri. Ravipudi Anjaneyulu garu for their unending support, affection and motivation to complete

my doctoral study. I pay my humble honours to these great visionaries who really helped for overall my educational career development.

How can I forget the fine dinging at Vaitheeswaran Sir's home and the cherished and joyful moments with cuties Sriya, Sraddha. Thank You Sriya and Sraddha you made the most awesome moments in my Ph.D days. I also express my humble honours to parents of Sir and Madam for their warm affection towards me.

At this moment I express my deep thanks to my brothers Ravi Kunchala, Rambabu Kunchala and my elder father Sri Ankamma Kunchala, my younger father Sri Rama Rao Kunchala, nephew Vasu, mavayya Srinivasa Rao Bandi, Kanya Akka, Kalyani Kunchala, Anjamma Chinnamma, Srinu Anna, Vijaya Akka and Venkata Swamy mavayya from Nellore for their unconditional love and support at hard times during these years.

I reminiscent the cherished moments with little angels Nandini, Sanjana, Bhavya, Mani, Bala and Surya.

My heart deepens to recollect the memories she had left, my niece Sujatha. With wet heart I take the cheers and joy we had throughout my life. Miss you Suja.

My sisters Malathi, Vijaya Lakshmi and brother-in-laws Sambasiva Rao, Koteswara Rao for their warm affection and caring. My parents **Lakshavamma** and **Narayana**. This endeavor becomes not worthy because my Father is now not with me to see the success of his knowledge. Nanna physically you may not with me but you are there in each step of my life.

Ramesh Babu Kunchala

Contents

List of Figures

List of Tables

To my Father

Chapter 1

Introduction

Abstract

In this chapter we present the current scenario of environmental concerns of the globe. The classification of energetic materials and the importance of eco-friendly energetic materials is briefly discussed. The success of density functional theory in handling the energetic materials especially under high pressure is presented. The objective and the chapter wise out line of the thesis are also presented.

Energetic materials are those which contain both fuel and oxidizer and reacts readily with the release of huge chemical energy stored within their molecular structures upon external stimulus such as heat, impact, shock, electric spark etc [1]. The amount of energy released from an energetic material within a short time is considerably large when compared to the normal materials. Depending upon their behavior towards external stimuli and their burning characteristics, energetic materials can be classified into the following four categories: Primary explosives, secondary explosives or high explosives, propellants, and pyrotechnics [2]. Primary explosives are substances which show a very rapid transition from burning to detonation. These materials are more sensitive towards heat, impact, or friction. On detonation, primary explosives generate tremendous amount of heat and/or shock that can be used to initiate the secondary explosive materials. Therefore primary explosive materials can be used as initiating devices. Lead azide, lead styphnate, tetrazene, are typical examples of primary explosives. Secondary explosives are substances which can generate huge amounts of heat energy on detonation that is greater than primary explosives. But, secondary explosives are less sensitive than primary explosives as they cannot be detonated readily by heat or shock. RDX, HMX, TNT, CL-20 are some of the prominent examples of secondary explosives. Propellants are combustible materials containing all the oxygen needed for their combustion. Propellants can be initiated by a flame or spark and charge. Black powder and ammonium nitrate based explosives come under this category. Pyrotechnics are those that can undergo self contained and self sustained chemical reactions by themselves with the release of large amounts of gas. Oxygen candles, heavy metals such as Barium (Ba) are the examples for this class of compounds.

For any country, it is highly recommendable to have huge amount of energetic materials because of their wide range of applications in various sectors. For example, energetic materials are used in agriculture, mining, building demolition, pyrotechnics, coal blasting, tunneling, welding etc. They can be even used in fracturing kidney and gall bladder stones. Most importantly they are used in fire fighting in war heads and as rocket boosters in aero space applications [1–3]. The performance characteristics of any energetic material can be assessed by looking at its sensitivity towards detonation by external stimulus, heat of explosion, detonation velocity, detonation pressure, thermal stability, crystal density

and crystal morphology [1, 2]. It is also required to look at the nature of the detonation products of the energetic material. The detonation products of most of the energetic materials are water vapour, carbon monoxide CO, and carbon-di-oxide CO_2. These are well known green house gases and are responsible for tremendous warming apart from other dangerous gases such as methane, nitrous oxide, sulfur di-oxide. This scenario would lead to increase in temperature of the atmosphere leading to the warming of the earth's surface. According to Intergovernmental Panel on Climate Change (IPCC), the average global temperature will rise by 0.7 F to 2.2 F by the year 2030 and by 10.4 F over the next 100 years [4, 5]. The major threats that the human kind would meet due to the global warming are: rise in sea levels and melting of ice at poles, floods and droughts will become more common and acid rains will occur frequently, eco system will change, which would greatly affect the agriculture and vegetation in a negative way. Therefore, the human kind on this planet faces a great challenge of overcoming the problem of global warming. Most importantly, the world requires alternate energy materials that only generate green energy products such as N_2, H_2. Nitrogen rich and hydrogen storage materials would meet these demands quite well.

Nitrogen-rich compounds in general possess a high energy content, high thermal stability, and low sensitivity [6]. Most importantly, the detonation products of the nitrogen based energetic materials are pure nitrogen gas which is environment friendly. The high energy content of nitrogen rich energetic materials comes from the presence of adjacent nitrogen atoms to form nitrogen molecule N≡N. These transformations are accompanied with an enormous amount of energy release due to the wide difference in the energies of N-N (160 kJ/mol) and N≒N (418 kJ/mol) bonds when compared to N≡N (954 kJ/mol). Moreover, the nitrogen rich energetic materials generate large volume of nitrogen gas which enables them to be used as clean burning gas generators. In addition, high nitrogen content materials in general possess large heats of formation due to the presence of large number of N-N bonds. These properties project the nitrogen based energetic materials as good replacements for the currently used toxic high energy materials such as RDX, HMX and CL-20 [6]. Polymeric nitrogen, in which the nitrogen atoms are attached in single bonded networks, is considered to be an ultimate high green energy density

material whose energy is three to four times greater than that of known high energetic materials such as RDX, HMX, CL-20 [7, 8]. Inorganic metal azides, especially alkali metal azides which are relatively stable compounds when compared to other metal azides, have been found as potential candidates to synthesize polymeric nitrogen at elevated pressures. By using NaN_3 as a starting material, Eremets et al. have synthesized the polymeric networks of nitrogen by combined high pressure X-ray powder diffraction and Raman spectroscopic techniques. Their study concluded that double bonded N atoms of the azide ion become single bonded N atoms at a pressure of around 120 GPa [9]. The discovery of polymeric form of nitrogen has created a new path in the field of high pressure science of inorganic metal azides [10–19]. Besides this, nitrogen rich secondary explosive compounds are also synthesized with performance characteristics comparable to that of known energetic materials such as RDX (1,3,5-Trinitroperhydro-1,3,5-triazine, $C_3H_6N_6O_6$), HMX (Octahydro-1,3,5,7-tetranitro-1,3,5,7-tetrazocine, $C_4H_8N_8O_8$) etc [6]. On the other hand, solid state hydrogen storage materials received tremendous attention towards the efficient storage of hydrogen and kinetics of the hydrogen release [20]. They are widely used as an important component in solid rocket propellants [21]. Among the solid state hydrogen storage materials, nitrogen based alkali metal amides are of particular interest as they possess potential reversible hydrogen storage applications [6].

In this thesis we have considered the green energy generating materials namely alkali metal azides, alklai-earth metal azides whose end products are pure nitrogen gas and also alkali metal amides whose end products are hydrogen gas only. Apart from these energetic compounds we have also studied the nitrogen rich secondary energetic material Guanidinium-2-methyl-5-nitraminotetrazolate. For any energetic system, the knowledge of crystal structure and the structure dependent properties are quite important to understand the decomposition phenomena and its high pressure behavior. In addition, the electronic band structure and optical properties are required to gain insights into the electronic processes that occur in solid energetic materials. In this present work, we aim to investigate theoretically these fundamental physical and chemical properties of the above mentioned energetic materials.

Density Functional Theory (DFT) is a successful tool in simulating and predicting the physical and chemical properties of a wide spectrum of materials [23–26]. In many cases the results obtained through the DFT calculations are in reasonable agreement with experimental data. However, most of the energetic materials have complicated crystal structures with weak inter molecular interactions and hence the investigation of different physical and chemical properties of energetic materials through DFT is really a challenging task [27]. Byrd et al. have applied DFT to predict the structural properties of various energetic materials at ambient conditions [28]. However, the predicted lattice parameters had large errors relative to the experiments. This is due to the fact that the usual DFT based exchange-correlation functional obtained within the local density approximation (LDA) and generalized gradient approximation (GGA) are not accurate enough to describe the systems having very small electronic overlap between the constituent atoms. Nevertheless, DFT can predict the lattice parameters of the energetic materials that are in close agreement with experiments [29] provided the exchange-correlation functionals are corrected to describe the weak intermolecular interactions. The advances in DFT methods and increase in computer resources in recent years has enabled us to describe materials that range from simple to complex solids with weak dispersive interactions. The dispersion corrected DFT methods proposed by Grimme (G06) [30], Tkatchenko and Scheffler, TS [31], and Ortmann, Bechstedt, and Schmidt, OBS [32] have been widely tested for various kinds of materials that include layered materials, molecular crystals [33, 34] and some energetic materials [29].

In this present work, we apply standard DFT methods and also dispersion corrected DFT methods to study the structural, electronic, bonding, optical, vibrational and thermodynamic properties of alkali metal azides, alkaline-earth metal azides, alkali metal amides and crystalline G-MNAT. The main goals of the thesis are the following:

- Study of role of van der Waals interactions in describing the crystal structure of alkali and alkaline-earth metal azides, alkali metal amides and G-MNAT.
- Understanding the electronic band structures and optical properties of alkali and alkaline-earth metal azides and alkali metal amides.

- Mechanical stability of alkali and alkaline-earth metal azides and alkali metal amides through elastic constants.
- High pressure study of alkali metal azides Lithium azide and Potassium azide.
- Study of equation of state and vibrational properties of nitrogen rich crystalline G-MNAT.

The thesis describes the above mentioned objectives with a total of eight chapters, this chapter is being the first. The details of the remaining chapters are as follows:

Chapter 2: This chapter deals with the quantum mechanical many-body problem and the methods to solve it. We have presented a short over view of density functional theory and different approximations such as local density approximation, generalized gradient approximation. The concept of pseudopotential theory is introduced and the two different pseudopotentials namely norm-conserving pseudopotential and ultrasoft pseudopotentials is explained briefly. We also discussed about the Cambridge sequential total energy package and the full potential linearized augmented plane wave method which are used in the present work. The van der Waals corrected density functional theory is also discussed.

Chapter 3: The results on structural, elastic, electronic, vibrational and thermodynamic properties of layered structure energetic alkali metal azides LiN_3, NaN_3, KN_3, RbN_3 and CsN_3 are presented in this chapter. All the calculations are carried out by means of plane wave pseudopotential method with and without including van der Waals interactions. The calculated ground state structural properties are improved to a greater extent by the inclusion of dispersion corrections, particularly with Grimme functional in generalized gradient approximation (PBE+G06), implies that the van der Waals interactions play a major role in determining the physical properties of these systems. The elastic constants and the related bulk mechanical properties for the monoclinic LiN_3, NaN_3 and tetragonal KN_3, RbN_3 and CsN_3 have been calculated using both the methods and found that the compounds are mechanically stable. A correlation has been proposed to relate the calculated elastic constants to the decomposition phenomena for the metal azides.

Electronic band structures are calculated and found that the metal azides are direct band gap insulators. The optical properties such as optical absorption and photo conductivity are calculated and the prominent peaks are analyzed through the corresponding interband transitions. The experimentally reported vibrational frequencies at the gamma point are exactly reproduced by the present calculations.

Chapter 4: In this chapter we discuss the physical and chemical properties of alkaline-earth metal azides $Ca(N_3)_2$, $Sr(N_3)_2$ and $Ba(N_3)_2$. Since PBE+G06 functional gives good results when compared to other dispersion corrected density functionals for alkali metal azides, we adopted PBE+G06 functional in addition to the general PBE functional for all the calculations. By using the optimized crystalline geometries using two methods, we computed the elastic constants and vibrational frequencies of the metal azides. The computed results are in good comparison with the experimental data. The electronic band structures of the metal azides are calculated by using different exchange-correlation functionals to compute the exact band gap of the materials. Similar to alkali metal azides, these materials are also found to be photo sensitive hence the optical absorption and photoconductivity as a function of photon energy are calculated and the prominent peaks are analyzed through the corresponding interband transitions. The present study concludes that the alkaline-earth metal azides undergo photochemical decomposition under the action of ultra-violet light.

Chapter 5: The electronic structure, elastic and optical properties of nitrogen based solid hydrogen storage materials $LiNH_2$, $NaNH_2$, KNH_2, and $RbNH_2$ are presented in this chapter. The calculated ground state properties are in good agreement with experiment. Our calculations predict that $LiNH_2$ is stiffer among the metal amides. The calculated elastic constants show that all the compounds are mechanically stable. The melting temperatures of the materials follow the order $RbNH_2 < KNH_2 < NaNH_2 < LiNH_2$. The electronic band structure reveals that all the compounds are semiconductors with a considerable band gap. The $[NH_2]^-$ derived states are completely dominating in the entire valence band region while the metal atom states occupy the conduction band. The optical properties such as complex dielectric function, optical absorption, refractive index and photo conductivity are calculated. The calculated band structure is used to analyze the

different interband optical transitions found to occur between valence and conduction bands. Our calculations show that these materials have considerable optical anisotropy.

Chapter 6:The high pressure behavior of alkali metal azides, monoclinic LiN_3 and tetragonal KN_3 is addressed in this chapter. All the calculations are performed with and with out inclusion of vander Waals interactions. We find that both LiN_3 and KN_3 are structurally stable up to the studied pressure range of 60 GPa for LiN_3 and 20 GPa for KN_3 respectively. The compressibility of both the crystals is anisotropic which is in good agreement with experiment. Under the application of pressure the magnitude of the electronic band gap value decreases, indicating that the system has the tendency to become semi conductor at high pressures. The optical properties such as refractive index, absorption spectra and photo conductivity along the three crystallographic directions are calculated at ambient as well as at high pressures. The calculated refractive index shows that the system is optically anisotropic and the anisotropy increases with increase in pressure. The observed peaks in the absorption and photo conductivity spectra are found to shift towards the higher energy region as pressure increases which imply that in LiN_3 and KN_3 decomposition is favored under pressure with the action of light. The vibrational frequencies for the internal and lattice modes of LiN_3 at ambient conditions as well as at high pressures are calculated from which we predict that the response of the lattice modes towards pressure is relatively high when compared to the internal modes of the azide ion. In the case of KN_3, as pressure increases the E_g mode gets softened as observed in the experiment. Despite the softening of E_g mode, the enhancement of intramolecular interactions keeps the lattice stable.

Chapter 7: In this chapter, we present the crystal structure, equation of state and vibrational properties of nitrogen rich solid energetic material G-MNAT. The ground state structural properties calculated with dispersion corrected density functionals (PBE+G06 and PBE+TS) are in good agreement with experiment. The computed equilibrium crystal structure is further used to calculate the equation of state and zone-center vibrational frequencies of the material. We found that the compressibility of G-MNAT is anisotropic and the lattice is more compressible along the a-axis and least compressible along b-axis. The calculated vibrational

frequencies are found to be in good agreement with the available experimental data.

Chapter 8: Thesis summary and future scope of the work is discussed in this chapter.

References

[1] Thomas M Klapötke, Chemistry of High Energy Materials, ISBN-10: 3110227835, 2011.

[2] J. Akhavan, The Chemistry of Explosives, Royal Society of Chemistry: Cambridge, UK ISBN-10: 1849733309, 2011.

[3] Z. Chen, M. W. Foster, J. Zhang, L. Mao, H. A. Rockman, T. Kawamoto, K. Kitagawa, K. I. Nakayama, D. T. Hess, J. S. Stamler, Proc. Nat. Acad. Sci. 102 (2005) 12159.

[4] W. J. Botzen, J. M. Gowdy, J. C. J. M. Vanden, Climate Policy, 8 (2008) 569.

[5] IPCC (2007d). "6.1 Observed changes in climate and their effects, and their causes". 6 Robust findings, key uncertainties. Climate Change 2007: Synthesis Report. A Contribution of Working Groups I, II, and III to the Fourth Assessment Report of the Intergovernmental Panel on Climate Change (IPCC). Geneva, Switzerland: IPCC.

[6] T. Fendt, N. Fischer, T. M. Klapötke, J. Stierstorfer, Inorg. Chem. 50 (2011) 1447.

[7] M. I. Eremets, A. G. Gavriliuk, I. A. Trojan, D. A. Dzivenko, , R. Boehler, Nat. Mater. 3 (2004) 558.

[8] M. I. Eremets, R. J. Hemley, H. K. Mao, E. Gregoryanz, Nature 411 (2001) 170.

[9] M. I. Eremets, M. Yu. Popov, I. A. Trojan, V. N. Denisov, R. Boehler, R. J. Hemley, J. Chem. Phys. 120 (2004) 10618.

[10] S. A. Medvedev, I. A. Trojan, M.I. Eremets, T. Palasyuk, T.M. Klapotke, J. Evers, J. Phys.: Condens. Matt. 21 (2009) 195404.

[11] Cheng Ji, Fuxiang Zhang, Dongbin Hou, Hongyang Zhu, Jianzhe Wu, Ming-ChienChyu, Valery I.Levitas, YanzhangMaa, J. Phys. Chem. Solids. 72 (2011) 736.

[12] S. A. Medvedev, T. Palasyuk, I. A. Trojan, J. Evers, T. M. Klapötke and M. I. Eremets, Private communications (2011).

[13] D. Hou, F. Zhang, C. Li, T. Hannon, H. Zhu, J. Wu, V. Levitas, Y. Ma, J. App. Phys. 110 (2011) 023524.

[14] D. Hou, F. Zhang, C. Li, T. Hannon, H. Zhu, J. Wu, Y. Ma, Phys. Rev. B 84 (2011) 064127.

[15] C. Li, R. Zhang, D. Hou, H. Zhu, J. Wu, M. Chyu, Y. Ma, J. App. Phys. 111 (2012) 112613.

[16] H. Zhu, F. Zhang, C. Ji, D. Hou, J. Wu, T. Hannon, and Y. Ma, J. App. Phys. 113 (2013) 033511.

[17] M. Zhang, H. Yan, Q. Wei, H. Wang, Z. Wu, Euro. Phys. Lett. 101 (2013) 26004.

[18] X. Wu, H. Cui, J. Zhang, R. Cong, H. Zhu, Q. Cui, App. Phys. Lett. 102 (2013) 121902.

[19] M. Zhang, K. Yin, X. Zhang, H. Wang, Q. Li, Z. Wu, Solid State Comm. 161 (2013) 13.

[20] S. Orimo, Y. Nakamori, J. R. Eliseo, A. Züttel, C. M. Jensen, Chem. Rev. **2007** 107, 4111.

[21] Charles S. Woodson, R. H. Grubbs, R. W. Humble, US Patent US 2003/0164215 A1 (2003).

[22] P. Chen, Z. Xiong, J. Luo, J. Lin, KL. Tan, Nature **2002**, 420, 302.

[23] I. I. Oleynik, M. Conroy, S. V. Zybin, L. Zhang, A. C. van Duin, W. A. Goddard III, C. T. White, CP 845, Shock Compression of Condensed Matter (2005) 573.

[24] R. O. Jones, O. Gunnarsson, Rev. Mod. Phys. 61 (1989) 689.

[25] M. C. Payne, M. P. Teter, D. C. Allan, T. A. Arias, J. D. Joannopoulos, Rev. Mod. Phys. 64 (1992) 1045.

[26] G. Onida, L. Reining, A. Rubio, Rev. Mod. Phys. 74 (2002) 601.

[27] E. F. C. Byrd, B. M. Rice, J. Phys. Chem. C 111 (2007) 2787.

[28] E. F. C. Byrd, G. E. Scuseria, C. F. Chabalowski, J. Phys. Chem. B 108 (2004) 13100.

[29] D. C. Sorescu, B. M. Rice, J. Phys. Chem. C 114 (2010) 6734.

[30] S. Grimme, J. Comp. Chem. 27 (2006) 1787.

[31] A. Tkatchenko, M. Scheffler, Phys. Rev. Lett. 102 (2009) 073005.

[32] F. Ortmann, F. Bechstedt, W. G. Schmidt, Phys. Rev. B 73 (2006) 205101.

[33] T. Bucko, J. Hafner, S. Lebègue, and Janos G. Angyan, J. Phys. Chem. A 114 (2010) 11814.

[34] V. Barone, M. Casarin, D. Forrer, M. Pavone, M. Sambi, A. Vittadinin, J. Comp. Chem. 30 (2009) 934.

Chapter 2

Theoretical Methods

Abstract

In this chapter, we discuss briefly the quantum mechanical many-body problem and the methods to solve it. We present a short over view of density functional theory and different approximations such as local density approximation, generalized gradient approximation. The concept of pseudopotential theory is introduced and the two different pseudopotentials namely norm-conserving pseudopotentials and ultrasoft pseudopotentials is explained briefly. We also discuss about the Cambridge sequential total energy package and the full potential linearized augmented plane wave method.

2.1 Introduction

According to quantum mechanics, a solid can be considered as a system of nuclei and electrons in interaction whose exact ground state can be obtained by solving the many-body Schrödinger equation

$$\hat{H}\Psi = E\Psi \tag{2.1}$$

where $\hat{H}$ is Hamiltonian of the system given by sum of the operators for kinetic and potential energy for all particles of the system

$$\hat{H} = \hat{T}_n + \hat{T}_e + \hat{V}_{ne} + \hat{V}_{nn} + \hat{V}_{ee} \tag{2.2}$$

where $\hat{T}_n$ is the kinetic energy of the nuclei, $\hat{T}_e$ is the kinetic energy of the electrons, $\hat{V}_{ne}$ is the nuclear-electronic coulomb attraction potential, $\hat{V}_{nn}$ is the nuclear-nuclear coulomb repulsion potential and $\hat{V}_{ee}$ is the electron-electron coulomb repulsion potential. On substituting the corresponding expressions for each operator, the Hamiltonian now becomes,

$$\hat{H} = -\frac{\hbar^2}{2M_I}\sum_I \nabla_I^2 - \frac{\hbar^2}{2m_i}\sum_i \nabla_i^2 + \sum_{i,I}\frac{Z_I e^2}{|r_i - R_I|} + \frac{1}{2}\sum_{I\neq J}\frac{Z_I Z_J}{|R_I - R_J|} + \frac{1}{2}\sum_{i\neq j}\frac{e^2}{|r_i - r_j|} \tag{2.3}$$

Here m_i and M_I are the mass of i-th electron and I-th nucleus, ∇_i^2, and ∇_I^2 are the Laplacian operators of the i-th electron and I-th nucles respectively, Z_I and Z_J are the atomic number of nuclei I, J respectively, e is electron charge, $\hbar$ is reduced Planck's constant, r_i and R_I are the position vectors of i-th electron and I-th nucleus respectively. The distance between the i-th electron and I-th nucleus is given by $|r_i\text{-}R_I|$ whereas $|R_I\text{-}R_J|$ and $|r_i\text{-}r_j|$ are the distance between the I-th and J-th nucleus and i-th and j-th electrons respectively. Equation (2.3) is quite difficult to solve for systems with more than two electrons and hence approximations are needed to solve the problem. The first approximation is Born-Oppenheimer approximation according to which the nuclei are many orders of magnitude more massive than the electrons and therefore they can be thought as stationary point particles surrounded by rapidly moving electrons. That means the nuclei are regarded as fixed and the electrons can be thought as moving in a static electric potential arising from the nuclei. Therefore the nuclei kinetic energy

term can be discarded from the equation and the total Hamiltonian can now be written as

$$\begin{aligned}\hat{H} &= \hat{T}_e + \hat{V}_{ne} + \hat{V}_{nn} + \hat{V}_{ee} \\ &= -\frac{\hbar^2}{2m_i}\sum_i \nabla_i^2 + \sum_{i,I}\frac{Z_I e^2}{|r_i - R_I|} + \frac{1}{2}\sum_{I\neq J}\frac{Z_I Z_J}{|R_I - R_J|} + \frac{1}{2}\sum_{i\neq j}\frac{e^2}{|r_i - r_j|} \quad (2.4)\end{aligned}$$

In the above equation, the second term is called as V_{ext} because it includes the potential due to the nuclei as well as any external potential. The last term can be treated as constant and it can be neglected. Therefore the electronic Hamiltonian can now becomes

$$\hat{H} = \hat{T}_e + \hat{V}_{ee} + \hat{V}_{ext} \quad (2.5)$$

By using this Hamiltonian, solving the Eqn. (2.1) to obtain the many body wave function Ψ is then enough to determine the observable properties such as ground state energy etc.

But, still it is computationally too expensive to solve. This fact readily suggests that more approximations are required to solve the problem. The most successful approaches to overcome this problem are Hartree-Fock approximation and the density functional theory (DFT). Hartree-Fock approximation was developed in the early days of quantum mechanics and is based on a guess of the form of many body wave function and with that the energy of the system and the related properties will be calculated. But, the wave function itself is a complicated quantity as it depends on 3N spatial variables where N is the number of electrons of the system together with the spin variable. This limits the application of this method to large systems, for example, solids with hundreds of atoms and large basis sets is too difficult to handle. On the other hand, DFT is a more recent approach which uses the ground state density as the basic variable rather than the many electron wave function of the system. The advantage of using electron density over wave function is the much reduced dimensionality. It does not matter how many electrons are there in the system but the density is always three dimensional. This enables DFT to be applied for larger systems with hundreds or even thousands of atoms become possible. There are a range of text books and review articles available on authoritative and comprehensive discussions of DFT [1–6].

2.2 Density Functional Theory

Density functional theory rests on two fundamental mathematical theorems proved by Hohenberg and Kohn [7] and the derivation of set of equations given by Kohn and Sham. The first theorem states that *there exists a one to one mapping between external potential and electron density.* That means the ground state energy can be expressed as a unique functional of electron density, E[n(r)], where n(r) is the electron density. Although the first Hohenberg-Kohn theorem rigorously proves that a functional of the electron density exists that can be used to solve the Schrödinger equation, the theorem says nothing about what is the functional actually. The second Hohenberg-Kohn theorem defines an important property of the functional and it states that *the density that minimizes the energy of the over all functional is the true electron density corresponding to the full solution of the Schrödinger equation.* Therefore we can get the ground-state energy by minimizing the energy functional,

$$E[n] = F[n] + \int V_{ext}(r)n(r)dr \tag{2.6}$$

where

$$F[n] = -\frac{\hbar^2}{2m_i}\sum_i \langle\Psi[n]|\nabla_i^2|\Psi[n]\rangle + \frac{e^2}{2}\sum_{i\neq j}\langle\Psi[n]|\frac{1}{|r_i - r_j|}|\Psi[n]\rangle \tag{2.7}$$

is called a universal functional of $n(r)$ as it is only dependent on $n(r)$ and independent from any external potential $V_{ext}(r)$.

Although this theorem provided a proof in principle that the total energy could be obtained from the ground state density but it was not yet known how to obtain $n(r)$ and thereby the functional F[$n(r)$]. This difficulty was solved by Kohn-Sham formulation [8] according to which the right electron density can be found by considering non-interacting one electron orbitals and approximate the kinetic energy of the system. The central equation in Kohn-Sham DFT has the form given by

$$\Big[-\frac{\hbar^2}{2m_i}\nabla_i^2 + e^2\int\frac{n(r')}{|r-r'|}dr' + V_{XC}(r) + V_{ext}(r)\Big]\phi_i(r) = \epsilon_i\phi_i(r) \tag{2.8}$$

here ϕ_i are the Kohn-Sham orbitals with the electron density expressed by

$$n(r) = \Sigma_i^N \mid \phi_i^2 \mid \tag{2.9}$$

and ϵ_i is the energy of the Kohn-Sham orbital. There are three potentials on the left-hand side of the Kohn-Sham equation given in Eqn. (2.8) along with the kinetic energy of the non-interacting system being the first term. The first potential is called the Hartree potential, which describes the Coulomb repulsion between the electron being considered in one of the Kohn-Sham equations and the total electron density defined by all other electrons in the system. The second potential defines the exchange and correlation contributions to the single electron Kohn-Sham equation and it can be formally defined as a "functional derivative" of the exchange-correlation energy

$$V_{XC}(r) = \frac{\delta E_{XC}[r]}{\delta n(r)} \tag{2.10}$$

where E_{XC} is the exchange-correlation functional. The third potential is the external potential which defines the interaction between the electron and the collection of atomic nuclei. Now we can define an effective potential (υ_{eff}) as

$$\upsilon_{eff} = e^2 \int \frac{n(r')}{|r - r'|} dr' + V_{XC}(r) + V_{ext}(r) \tag{2.11}$$

and this allows to write the Eqn. (2.8) as

$$\Big[-\frac{\hbar^2}{2m_i} \nabla_i^2 + \upsilon_{eff}(r) \Big] \phi_i(r) = \epsilon_i \phi_i(r) \tag{2.12}$$

To solve the Kohn-Sham equations we need to define the Hartree potential and to define the Hartree potential we must know the electron density. But, to find the electron density we must know the single electron Kohn-Sham orbitals and to know these we must solve the Kohn-Sham equations. Clearly, the Kohn-Sham equations must be solved by self-consistently. Once we know the final electron density then the total energy can be calculated from

$$E[n(r)] = \sum_i \epsilon_i - \frac{e^2}{2} \int \frac{n(r) n(r')}{\mid r - r' \mid} + E_{XC}[n(r)] - \int V_{XC}(r) n(r) dr \tag{2.13}$$

but it is too difficult to find the exchange-correlation functional exactly and hence required approximations to handle it. In the case of homogeneous electron gas, where the electron density is constant at all points in space, this functional can be derived exactly. Using this the E_{XC} can be approximated for any real material as

$$E_{XC}[n(r)] = \int n(r)\epsilon_{XC}^{hom}[n(r)]dr \tag{2.14}$$

where ${\epsilon_{XC}}^{hom}[n(r)]$ is the exchange-correlation density of a homogeneous electron gas with density n(r). This approximation for E_{XC} is called as local density approximation (LDA). Since LDA is based on homogeneous electron gas it is expected to be accurate only for systems in which the electron density varies slowly. The most common implementation of LDA is the parametrization scheme proposed by Ceperley and Alder [9, 10]. It is not suitable to the systems where the electron density undergoes rapid changes. To overcome this deficiency another approximation for exchange-correlation functional E_{XC} has been developed and it is called as generalized gradient approximation (GGA) [11]. This method takes into account the inhomogeneity of the electron density by adding information about the gradient of the density, $\nabla n(r)$, to the exchange-correlation functional. The general form of E_{XC} in GGA is expressed as

$$E_{XC}[n(r)] = \int n(r)\epsilon_{XC}^{hom}[n(r)]\nabla n(r)dr \tag{2.15}$$

The most recent implementation of GGA is the parametrization scheme proposed by Perdew-Burke-Ernzerhof (PBE) [12]. Beyond the LDA and GGA functionals there are some other functionals also called as "hybrid functionals" and the most popular one is B3LYP hybrid functional developed by Stephens et al [13].

2.3 Plane waves

In the case of solids, the Kohn-Sham equations are still intractable because of the infinite number of non-interacting electrons. For each electron, the electronic wave function extends over the entire lattice and thus the basis set required to expand the Kohn-Sham orbital is also infinite. But, when dealing with a crystal, which can be described as spatially repeated unit cells that only contain a small number

of nuclei and electrons. This leads to the use of periodic boundary conditions through the Bloch theorem. According to Bloch's theorem, the solution of the single particle Schrödinger equation in the presence of a periodic potential U(r) with U(r+R)=U(r) must have the form given by

$$\phi_i(\vec{k},\vec{r}) = e^{i\vec{k}\vec{r}}u_i(\vec{k},\vec{r}) \tag{2.16}$$

where $u_i\ (\vec{k},\ \vec{r}) = u_i\ (\vec{k},\ \vec{r}+\vec{R})$ is the cell-periodic part of the wave function for all Bravias lattice vectors $\vec{R}$ and $\vec{k}$ is the wave vector of the electron in first Brillouin zone. This implies

$$\phi_i(\vec{k},\vec{r}+\vec{R}) = \phi_i(\vec{k},\vec{r})e^{i\vec{k}\vec{R}} \tag{2.17}$$

On substituting this in Eqn. (2.8) for each given $\vec{k}$, a new set of eigen equations is found.Thus, each electron occupies an electronic state of definite wave vector $\vec{k}$. Therefore the problem of solving for an infinite number of electrons within the extended system is converted to solving for a finite number of electronic bands at an infinite number of k-points within the single reciprocal unit cell. The occupied states at each k-point contribute to the electronic potential, so that in principle an infinite number of calculations are needed. However, the wave function at k-points that are very close together will be almost identical. Therefore, one can represent the wave functions over a small region of reciprocal space around one k-point by the wave function at this k-point. In this case only a finite number of k-points are needed.

In order to solve the Kohn-Sham equations numerically, the Kohn-Sham orbitals needed to be expanded by well defined basis sets. Although there are many choices of basis sets available, the plane wave basis set is a common choice. The Kohn-Sham orbitals $\phi_i(\vec{k},\ \vec{r})$ can be expanded using the plane wave basis set as

$$\phi_i(\vec{k},\vec{r}) = e^{i\vec{k}\vec{r}}u_i(\vec{k},\vec{r}) = \frac{1}{\sqrt{V}}\sum_G C_{i,\vec{K}+\vec{G}}e^i(\vec{K}+\vec{G})\vec{r} \tag{2.18}$$

where 'G' is the reciprocal lattice vector, $C_{\vec{K}+\vec{G}}$ is the coefficient of the expansion. In principle, an infinite basis set of $\vec{G}$ should be used to expand the Kohn-Sham orbital $u_i\ (\vec{k},\ \vec{r})$. In practice it is possible to truncate the infinite basis set to

include only plane waves that have kinetic energies less than a define cut-off

$$\frac{1}{2} \mid \vec{K} + \vec{G} \mid^2 < E_{cut-off}. \tag{2.19}$$

Here the truncation of the plane wave basis set will introduce some error in the calculated energy. It is possible to reduce the magnitude of the error in a systematic way by increasing the value of the cut-off energy. In principle, the cut-off energy should be increased until the calculated total energy converges within the required tolerance.

2.4 Pseudopotentials

The core electrons are tightly bound to the nuclei and thus their wave functions are much localized in the regions near the nuclei. To expand the localized wave functions, a very high energy cut-off must be required to include large set of plane waves. Since the wave functions of the valence electrons are orthogonal to the core wave functions, they must oscillate in the regions where the core wave functions exist. But expanding the oscillating wave functions requires a very large number of plane waves. It is well known that the energies of the core electrons are usually much negative than those of the valence electrons. Therefore the chemical properties of the solid depends almost solely on the valence electrons. And also, the oscillations of valence wave functions in the core regions have very little influence to the electronic structure as they interact very little with neighbouring atoms. This fact lead to pseudopotential approximation in which the core electrons and the ionic potential are removed and replaced by a pseudopotential that acts on a set of pseudo wave functions instead of the true valence wave functions. In plane wave approximation only the valence electrons out side the core region are explicitly considered, therefore the pseudo wave functions need not be orthogonal to the core wave functions and can be represented by a node less function inside the core regions. This leads to the fewer plane waves in the expansion of pseudo wave functions. The most common general form of a pseudopotential is

$$V_{ps} = \sum_{lm} |Y_{lm}\rangle V_l(r) \langle Y_{lm}| \tag{2.20}$$

where Y_{lm} are the spherical harmonics. There are two important class of pseudopotentials namely norm-conserving pseudopotential [14] and ultrasoft pseudopotentials [15]. Norm-conserving pseudopotentials were first introduced by Haman, Schlüter, and Chiang [14]. In this method, inside a certain core radius, the many electron wave function is replaced by a soft nodeless pseudo wave function with the restriction that pseudo wave function must have the same norm as the many-electron wave function within the chosen core radius, out side the core radius the two wave functions are identical. In order to accurately reproduce the charge distribution and moments of many-electron wave functions, the core radius must be about as large as the outer most maximum of the many-electron wave function. Therefore in the case of strongly localized orbitals the resulting pseudopotentials require a large basis set which leads to computations very expensive. This problem was resolved by Vanderbilt by introducing the ultrasoft pseudopotentials [15]. In this method localized atom-centered augmentation charges are introduced to overcome the norm-conservation constraint. These augmentation charges are defined as the charge density difference between the many-electron and the pseudo wave function and are all generally treated on a regular grid in real space. A small cut off radius must be applied to all augmentation charges in order to restore the moments and the charge distribution of the many-electron wave function accurately. Nevertheless, ultrasoft pseudopotentails are good enough to get accurate results with less computational cost.

2.5 CAmbridge Sequential Total Energy Package

CAmbridge Sequential Total Energy Package, CASTEP, is a state-of-the-art quantum mechanics based program specially designed for solid state materials science [16]. CASTEP employs plane wave pseudopotential method to perform first principles density functional theory based calculations to explore the properties of crystalline materials. CASTEP can be used to calculate structural properties, band structure, total and partial density of states, elastic and optical properties of solid materials. In addition, the vibrational properties such as phonon dispersion, phonon density of states, thermodynamic properties can also be calculated

using linear response theory or finite displacement technique as implemented in CASTEP code. Here we briefly discuss about the tasks that can be performed using the code.

For all first principles based calculations it is mandatory to have a theoretical equilibrium crystal structure. This can be achieved by performing *Geometry Optimization* task in CASTEP. The geometry optimization is based on reducing the magnitude of calculated forces and stresses until they become smaller than defined convergence tolerances. After the completion of geometry optimization, the properties task allows to calculate the electronic eigen values along high symmetry directions in the Brillouin zone and also on a fine Monkhorst-Pack grid non-self consistently for both valence and conduction bands using electronic charge densities and potentials generated during the simulation, which results in electronic band structure and density of states respectively. The electron density difference with respect to either a linear combination of atomic densities or a linear combination of the densities of sets of atoms contained in the structure can be calculated. Elastic constants can be calculated using finite strain technique according to which a homogeneous strain will be applied to the lattice and then calculate the resulting stress. Matrix elements for electronic interband transitions can be calculated. The analysis dialogue allows to generate grid and chart documents of measurable optical properties. The evaluation of the second-order change in the total energy induced by atomic displacements will be used to calculate the dynamical matrix for a set of q-vectors. These set of dynamical matrices obtained in these calculations can be used to construct the force constant matrix through Fourier transformation. A full review of the capability of CASTEP can be found else where in ref [16].

2.6 Dispersion corrections to the DFT

In the case of molecular solids, the standard DFT techniques based on LDA and GGA will tend to give large errors in calculated structural parameters when compared to experiments due to the lack of description of van der Waals (vdW) interactions [5]. Most of the energetic materials are molecular solids with weak

dispersive interactions between the molecules and the standard DFT methods are inadequate to treat them effectively. Therefore, to treat vdW interactions efficiently, we have used the vdW correction to the exchange-correlation functional of standard density functional theory at semi empirical level. According to semi-empirical dispersion correction approach, the total energy of the system can be expressed as

$$E_{total} = E_{DFT} + E_{Disp} \tag{2.21}$$

with

$$E_{Disp} = s_i \Sigma_{i=1}^{N} \Sigma_{j>i}^{N} f(S_R R_{ij}^0, R_{ij}) C_{6,ij} R_{ij}^{-6}. \tag{2.22}$$

Here $C_{6,ij}$ is called dispersion coefficient between any atom pair i and j which solely depends upon the material and R_{ij} is the distance between the atoms i and j respectively. In the present work we have used the recently developed schemes by Ortmann, Bechstedt, and Schmidt (OBS) [17] in LDA and Grimme (G06) [18], Tkatchenko and Scheffler (TS) [19] approaches in GGA as implemented in CASTEP. These semi-empirical approaches provide the best compromise between the cost of first principles evaluation of the dispersion terms and the need to improve non-bonding interactions in the standard DFT description.

2.7 Full Potential Linearized Augmented Plane Wave (FP-LAPW) method

It is possible to solve the Kohn-Sham equations by avoiding an artificial core-valence separation of electrons as described by the pseudopotential. These methods are called all-electron methods in which all electrons are explicitly used in the computation. The linearized augmented plane wave method is the most accurate all-electron method for performing the electronic structure calculations for crystalline solids [20]. In this method the unit cell is divided into two types of regions namely (i) non-overlapping atomic spheres (centered at the atomic sites) (ii) an interstitial region. In side the atomic sphere of radius R, a linear combination of radial functions times spherical harmonics $Y_{lm}(r)$ is used

$$\phi_{kn} = \sum_{lm} [A_{lm,kn} u_l(r, E_l) + B_{lm,kn} \dot{u}_l(r, E_l)] Y_{lm}(\hat{r}) \tag{2.23}$$

where $u_l(r, E_l)$ is the regular solution of the radial Schrödinger equation for energy E_l chosen normally at the center of the corresponding band with l-like character and the spherical part of the potential inside the sphere, $\dot{u}_l(r, E_l)$ is the energy derivative of u_l evaluated at the same energy E_l. A linear combination of these two functions, which can be obtained by numerical integration of the radial Schrödinger equation of a radial mesh inside the sphere constitute the linearization of the radial function. The coefficients A_{lm} and B_{lm} are functions of k_n where $k_n = k+K_n$, K_n are the reciprocal lattice vectors and k is the wave vector inside the first Brillouin zone determined by requiring that this basis function matches each plane wave with the corresponding basis function of the interstitial region. In the interstitial region (ii), a plane wave expansion is used

$$\phi_{kn} = \frac{1}{\sqrt{\omega}} e^{ik_n r} \tag{2.24}$$

Each plane wave is augmented by an atomic-like function in every atomic sphere. The solutions to the Kohn-Sham equations are expanded in this combined basis set of linearized augmented plane waves according to the linear variation method

$$\psi_k = \sum_n c_n \phi_{kn} \tag{2.25}$$

here the coefficients c_n are determined by the Rayleigh-Ritz variation principle method. The convergence of this basis set is controlled by a cutoff parameter $R_{mt}K_{max} = 6$ to 9, where R_{mt} is the smallest atomic sphere radius in the unit cell and K_{max} is the magnitude of the largest K vector in the above equation.

In this present work we have used the Tran and Blaha modified Becke-Johnson exchange potential [21] that allows the calculation of band gaps with an accuracy similar to very expensive GW calculations. It is a semi-local approximation to an atomic "exact-exchange" potential and a screening term. This is just a exchange-correlation potential and not a exchange-correlation energy functional, thus E_{XC} is taken from either LDA or GGA and the forces cannot be used with this option.

References

[1] R. M. Martin, Electronic Structure: Basic theory and practical methods Cambridge University Press ISBN 0-521-78285-6 (2004)

[2] J. Kohanoff, Electronic structure calculations for solids and molecules: theory and computational methods Cambridge University Press ISBN- 10 0-521-81591-8 (2006)

[3] R. G. Parr and W. Yang, Density Functional Theory of Atoms and Molecules New York: Oxford University Press. ISBN 0-19-509276-7 (1989)

[4] M. C. Payne, M. P. Teter. D. C. Allan. T. A. Arias and J. D. Joannopoulos, Rev. Mod. Phys. 64 (1991) 1045.

[5] R. O. Jones and O. Gunnarsson, Rev. Mod. Phys 61 (1989) 689.

[6] P. Geerlings, F. D. Proft, and W. Langenaeker, Chem. Rev 103 (2003) 1793.

[7] P. Hohenberg and W. Kohn, Phys. Rev. 136 (1964) B684.

[8] W. Kohn and L. J. Sham Phys. Rev. 140 (1965) A1133.

[9] D. M. Ceperley, B. J. Alder, Phys. Rev. Lett. 45 (1980) 566.

[10] J. P. Perdew, A. Zunger, Phys. Rev. B. 23 (1981) 5048.

[11] J. P. Perdew, Y. Wang, Phys. ReV. B 45 (1992) 13244.

[12] J. P. Perdew, K. Burke, M. Ernzerhof, Phys. Rev. lett. 77 (1996) 3865.

[13] P. J. Stephens, F. J. Devlin, C. F. Chabalowski, M. J. Frisch, J. Phys. Chem. 98 (1994) 11623-11627.

[14] D. R. Hamann, M. Schlüter, C. Chiang, Phys. Rev. lett. 43 (1979) 1494.

[15] D. Vanderbilt, Phys. Rev. B. 41 (1990) 7892.

[16] M. Segall, P. Lindan, M. Probert, C. Pickard, P. Hasnip, S. Clark, M. J. Payne, J. Phys:. Cond. Matt. 14 (2002) 2717.

[17] F. Ortmann, F. Bechstedt, W. G. Schmidt, Phys. Rev. B 73 (2006) 205101.

[18] S. Grimme, J. Comp. Chem. 27 (2006) 1787.

[19] A. Tkatchenko, M. Scheffler, Phys. Rev. Lett 102 (2009) 073005.

[20] P. Blaha, K. Schwarz, G. K. H. Madsen, D. Kvasnicka, and J. Luitz, WIEN2K, An Augmented plane wave plus Local orbitals Programe for Calculating Crystal Properties, Karlheinz Schwarz, Techn. Universitat Wien, Austria, 2001.

[21] F. Tran and P. Blaha, Phys. Rev. Lett. 102 (2009) 226401.

Chapter 3

Alkali Metal Azides

Abstract

We report a detailed first principles study on the structural, elastic, vibrational and thermodynamic properties of layered structure energetic alkali metal azides LiN_3, NaN_3, KN_3, RbN_3 and CsN_3. All the calculations are carried out by means of plane wave pseudopotential method with and without including van der Waals interactions. The calculated ground state structural properties are improved to a greater extent by the inclusion of dispersion corrections, implies that the van der Waals interactions play a major role on the physical properties of these systems. The elastic constants and the related bulk mechanical properties for the monoclinic LiN_3, NaN_3 and tetragonal KN_3, RbN_3 and CsN_3 have been calculated using both the methods and found that the compounds are mechanically stable systems. The magnitude of the calculated elastic constants increases in the order CsN_3 < RbN_3< KN_3< NaN_3< LiN_3 implying higher elastic stiffness for LiN_3, the fact also confirmed by the higher values of bulk, shear and Young's moduli of LiN_3 over the other azides. The electronic band structure reveals that all the compounds are direct band gap insulators. The optical properties such as absorption and photoconductivity are calculated. The calculated band structure is used to analyze the different interband optical transitions occur between valence and conduction bands. The experimentally reported vibrational frequencies at the gamma point are exactly reproduced by the present calculations.

3.1 Introduction

Alkali metal azides are chemically and structurally simple compounds which find wide practical importance as explosives, gas generators, and also as photographic materials at low temperatures [1–5]. The structural simplicity of these compounds serve us to understand the complex chemical phenomena such as decomposition and detonation that occur in solid state energetic materials [4, 5]. Alkali metal azides, similar to other inorganic metal azides, show variation in stability towards heat, light and shock. They undergo decomposition into metal atom and nitrogen gas under the action of suitable wave length of light (ultra-violet light) and even detonation may occur when the temperature is close to their melting point. The decomposition reaction is as follows:

$$2MN_3 \rightarrow 2M + 3N_2 \tag{3.1}$$

where 'M' is the metal atom. Since the final decomposition product is pure nitrogen gas, these materials can also be used in automobile air bags [2].

Among the alkali metal azides, lithium azide and the low temperature phase of sodium azide are iso-structural and crystallize in monoclinic structure with *C2/m* space group [6]. The unit cell contains two formula units with metal cation occupies the site with fractional co-ordinates (0, 0, 0), central nitrogen atom of the azide occupies the (0, 0.5, 0.5) site whereas the end nitrogen atom is situated at (0.1048, 0.5, 0.7397) for LiN_3 and at (0.1016, 0.5, 0.7258) for NaN_3 respectively. The other alkali metal azides KN_3, RbN_3 and CsN_3 crystallize in a body-centered tetragonal structure with space group I4/mcm (140). The unit cell contains four molecules per unit cell with metal cation occupies the site with fractional co-ordinates (0, 0, 0.25), central nitrogen atom of the azide occupies the (0, 0.5, 0) site and the end nitrogen atom is situated at (0.1358, 0.6358, 0) for KN_3, (0.1315, 0.6315, 0) for RbN_3 and (0.1324, 0.6324, 0) for CsN_3 respectively. The crystal structure of the alkali metal azides clearly shows that the arrangements of the atoms are in layers as the azide ions are sandwiched between the metal atom layers as shown in Figure 3.1(a) and 3.1(b) [7]. This structural anatomy leads to a strong bonding between these two layers whereas there also exists a non-bonded interactions between the non-bonded nitrogen atoms of the azide ion also called as

van der Waals interactions as shown in Figure 3.1(a) and 3.1(b). Thus, the crystal structure of the metal azides involve both bonded and non-bonded interatomic interactions.

It is a known fact that decomposition and detonation are the collective properties of materials which depends on intermolecular interactions, molecular arrangements and thereby the crystal structure of the solid state. Alkali metal azides undergo rapid decomposition with evolution of large amounts of pure nitrogen gas at temperatures close to their melting points. In addition the metal azides show variation in impact sensitivity towards mechanical shock, for example, KN_3 is not sensitive to impact or friction whereas RbN_3 is more sensitive to mechanical shock and which compares with the impact sensitivity of trinitrotoluene (TNT) [4]. Thus, it is crucial to know the basic crystal structure and also the structure-related properties such as elastic, vibrational and thermodynamic properties of these materials.

There are some theoretical studies available on the electronic band structure of these materials [8, 9]. The structural properties, electronic band structure and optical properties of alkali metal azides were reported by using the usual density functional theory calculations [10–13]. These studies did not take account of van der Waals interactions in the calculations and also the calculated band gaps through usual DFT functionals would lead an error of 30-40% when compared to experimental values. To the best of our knowledge, there are no reports available on the comparative study of crystal structure and related properties such as elastic constants, vibrational properties and thermodynamic properties of the alkali metal azides based on density functional calculations with and without accounting the vdW interactions. In addition, the accurate band gap of the metal azides and thereby the optical properties have not been explored yet.

In this chapter, we present the effect of vdW interactions on ground state structural, elastic, vibrational and thermodynamic properties of the alkali metal azides. The calculated elastic constants are used to understand the sensitivity of the metal azide crystal lattice to the external stress. We have also studied the electronic band

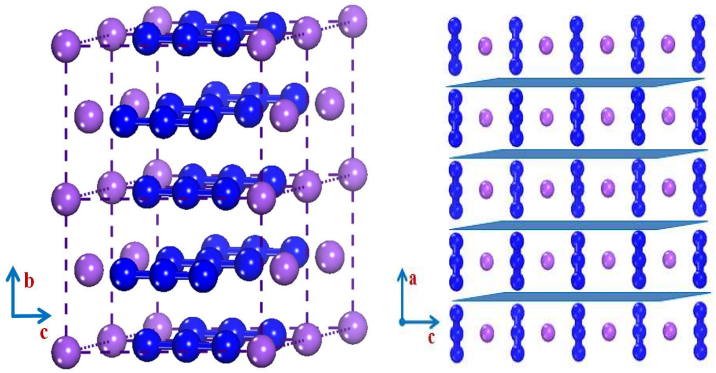

(a) (b)

FIGURE 3.1: (a) Crystal structure of MN_3 (M= Li or Na) (b) Layered structure of metal azide MN_3 (M= K or Rb or Cs). In both the figures, violet ball indicates metal atom and blue ball indicates nitrogen atom, respectively.

structures and nature of bonded interactions from density of states and bond population analysis. The calculated band structures are used to analyze the optical absorption and photoconductivity spectra of the metal azides. The computed vibrational frequencies and phonon density of states are used to calculate the thermodynamic properties such as heat capacity and free energy of the azides.

3.2 Computational details

First-principles density functional theory calculations are performed with the Cambridge Sequential Total Energy Package (CASTEP) program [14, 15], using Vanderbilt-type ultrasoft pseudo potentials [16] and a plane wave expansion of the wave functions. The electronic wave functions are obtained using density mixing scheme [17] and the structures are relaxed using the Broyden, Fletcher, Goldfarb and Shannon (BFGS) method [18]. The exchange-correlation potential of Ceperley and Alder [19] parameterized by Perdew and Zunger (CA-PZ) [20] in the local density approximation (LDA) and also the generalized gradient approximation (GGA) in Perdew-Burke-Ernzerhof (PBE) [21] is used to describe the exchange-correlation potential. The pseudo atomic calculations are performed for Li $1s^2\ 2s^1$, Na $2p^6\ 3s^1$, K $3s^2\ 3p^6\ 4s^1$, Rb $4s^2\ 4p^6\ 5s^1$, Cs $5s^2\ 5p^6\ 6s^1$ and N $2s^2\ 2p^3$. The Monkhorst-Pack scheme k-point sampling is used for integration over the Brillouin zone [22]. It is

well known that the cut-off energy and k-point mesh influences the convergence of calculations. Hence we tested the dependence of energy cut-off and k-point grid and found that for 520 eV plane wave cut-off energy and 5x8x5 k-point mesh, the change in total energy is less than 1 meV. We have then chosen these plane wave cut-off energy and k-point mesh for all the calculations. In the geometry relaxation, the self-consistent convergence on the total energy is $5x10^{-7}$ eV/atom and the maximum force on the atom is found to be 10^{-4} eV/Å. Elastic constants are calculated using finite strain technique as implemented in CASTEP code.

All the dynamical calculations are carried out by using the density functional perturbation theory as implemented in the CASTEP code [23, 24]. To study the effect of van der Waals interactions, we have used the recently developed schemes by Ortmann, Bechstedt and Schmidt (OBS) [25] in LDA and Grimme (G06) [28], Tkatchenko and Scheffler (TS) [27] approaches in GGA. These semiempirical approaches provide the best compromise between the cost of first principles evaluation of the dispersion terms and the need to improve non-bonding interactions in the standard DFT description. For the computation of electronic properties, we have used the linearized augmented plane wave (LAPW) method as implemented in WIEN2k package [28, 29]. We have used Engel-Vosko functional [30] and recently developed Tran Blaha-modified Becke Johnson potential [31] within GGA to get the accurate band gaps of the compounds in addition to the usual CA-PZ and PBE functionals.

3.3 Results and discussion

3.3.1 Crystal structure

As a first step we computed the equilibrium crystal geometries of the alkali metal azides LiN_3, NaN_3, KN_3, RbN_3 and CsN_3 by allowing the full lattice and atoms to relax and then computed the total energies. The structures with minimum total energy were considered as the optimized crystal structures and are used for further calculations. Although these materials are analogous to simple alkali halides but the presence of linear azide ion makes the crystal structure complex

with weak dispersion interactions between the azide ion layers. Hence, to handle effectively the vdW interactions, we have used the recently developed dispersion corrected functionals LDA (OBS), GGA (PBE+TS) and GGA (PBE+G06) in addition to the LDA (CA-PZ), GGA (PBE) functionals in order to check their virtue in describing the crystal structure of the alkali metal azides. For CsN_3, we have not carried out the calculations with dispersion corrected functionals due to the non-existence of dispersion corrected parameters for Cs atom.

The calculated values of the lattice parameters of the metal azides within the density functionals of LDA (CA-PZ), GGA (PBE) and dispersion corrected functionals LDA (OBS), GGA (PBE+TS) and GGA (PBE+G06) along with experimental data [6, 7] are shown in Table 3.1 for monoclinic LiN_3, NaN_3 and in Table 3.2 for tetragonal KN_3, RbN_3 and CsN_3 . When compared to the experimental data, our LDA calculations underestimate the lattice volume by -11.4 % and -9.5 % respectively for LiN_3 and NaN_3 and also -12.7% for KN_3, -10.6% for RbN_3 and -22.6% for CsN_3 whereas our GGA calculations overestimate the same by 5.7 % for LiN_3, 7.9 % for NaN_3, 4.6% for KN_3, 6.7% for RbN_3 and 9.5% for CsN_3 as shown in Table 1. This discrepancy can be expected for general density functional theory calculations using LDA and GGA [32]. Therefore in order to get the exact equilibrium crystal structures that are comparable with the experiment, we have carried out the crystal structure optimization calculations with the dispersion corrected functionals, CA-PZ+OBS in LDA and PBE+TS and PBE+G06 in GGA. Among the three dispersion corrected functionals, PBE+G06 gives the theoretical equilibrium volume that is very close to the experimental results (see Table 3.1). The theoretical volume obtained using PBE+G06 functional results with an underestimation of -1.8 % for LiN_3, -0.08 % for NaN_3, -2.2% for KN_3 and -0.04% for RbN_3 respectively. Whereas the LDA (OBS), GGA (PBE+TS) functionals give the theoretical results that are smaller than the measured values by -19.1 %, -4.3 % for LiN_3, -15.6 %, -0.8 % for NaN_3, -17.9%, -12.9% for KN_3 and -14.8%, -16.3% for RbN_3 respectively. Therefore among the three dispersion corrected functionals, the crystal volume calculated with PBE+G06 functional gives best agreement with that of the experimental volume.

TABLE 3.1: Ground state structural properties of monoclinic LiN_3 and NaN_3 calculated using various exchange-correlation functionals.

LiN_3 XC functional	a (Å)	b (Å)	c (Å)	β^0	N	V (Å^3)
LDA (CA-PZ)	5.328	3.199	4.727	102.6	(0.1244 0.5 0.7456)	78.6
GGA (PBE)	5.761	3.376	5.094	108.6	(0.1005 0.5 0.7490)	93.9
LDA (OBS)	5.158	3.074	4.615	100.9	(0.1288 0.5 0.7459)	71.8
GGA (PBE+TS)	5.541	3.296	4.796	104.3	(0.1174 0.5 0.7490)	84.9
GGA (PBE+G06)	5.686	3.219	4.884	102.7	(0.1094 0.5 0.7257)	87.2
Expt [6]	5.627	3.319	4.979	107.4	(0.1048 0.5 0.7397)	88.8
NaN_3 XC functional	a (Å)	b (Å)	c (Å)	β^0	N	V (Å^3)
LDA (CA-PZ)	5.868	3.568	5.081	102.5	(0.1148 0.5 0.7277)	103.8
GGA (PBE)	6.446	3.748	5.473	110.3	(0.0930 0.5 0.7350)	123.9
LDA (OBS)	5.670	3.483	4.981	100.2	(0.1219 0.5 0.7235)	96.8
GGA (PBE+TS)	6.243	3.616	5.269	106.8	(0.1055 0.5 0.7329)	113.8
GGA (PBE+G06)	6.217	3.647	5.229	104.7	(0.1094 0.5 0.7257)	114.7
Expt [6]	6.211	3.658	5.323	108.4	(0.1016 0.5 0.7258)	114.8

The predicted lattice parameter 'a' which involves the non-bonded interactions i.e., vdW forces between the layers as shown in Figure 3.1(a) and 3.1(b), using the conventional LDA (CA-PZ) and GGA (PBE) functionals result in large errors when compared to the experimental values. The computed lattice parameter 'a' of LiN_3 and NaN_3 is underestimated by -5.3 % and -5.5 % respectively using CA-PZ functional while the same is overestimated by 2.3 % (3.7 %) using PBE functional. Within the dispersion corrected functionals, the OBS functional results in large underestimation of the lattice constant 'a' while the other two functionals PBE+TS and PBE+G06 results in good accuracy with the measured value of the lattice parameter. In particular, PBE+G06 functional predicted the lattice constant with high accuracy of 0.5 % for monoclinic alkali metal azides.

In the case of tetragonal alkali metal azides, the predicted lattice parameter 'a' using the conventional LDA (CA-PZ) and GGA (PBE) functionals result in large errors when compared to the experimental values by -3.5%, 1.5% for KN_3 and -3.1%, 2.1% for RbN_3 respectively as shown in Table 3.2. The predicted lattice constant 'a' using the dispersion corrected functionals show large variations in terms of functionals where the LDA (OBS) and GGA (PBE+TS) underestimate by 4.8%, 8.1% for KN_3 and also by 4.2%, 8.7% for RbN_3 respectively. This readily tells

TABLE 3.2: The ground state structural properties of tetragonal KN_3, RbN_3 and CsN_3 calculated using LDA (CA-PZ), GGA (PBE), LDA (OBS), GGA (PBE+TS) and GGA (PBE+G06) functionals.

KN_3 XC functional	a(Å)	c(Å)	N	V (Å)
LDA (CA-PZ)	5.898	6.653	(0.1449 0.6449 0)	231.38
GGA (PBE)	6.205	7.207	(0.1388 0.6388 0)	277.54
LDA (OBS)	5.817	6.430	(0.1468 0.6468 0)	217.6
GGA (PBE+TS)	5.620	7.309	(0.1525 0.6525 0)	230.8
GGA (PBE+G06)	6.102	6.961	(0.1411 0.6411 0)	259.16
Expt [7]	6.113	7.094	(0.1358 0.6358 0)	265.09
RbN_3				
LDA(CA-PZ)	6.115	7.161	(0.1401 0.6401 0)	267.75
GGA(PBE)	6.445	7.691	(0.1338 0.6338 0)	319.54
LDA (OBS)	6.042	6.979	(0.1415 0.6415 0)	254.8
GGA (PBE+TS)	5.761	7.541	(0.1488 0.6488 0)	250.3
GGA(PBE+G06)	6.359	7.407	(0.1361 0.6361 0)	299.49
Expt [7]	6.310	7.519	(0.1315 0.6315 0)	299.37
CsN_3				
LDA(CA-PZ)	6.365	7.741	(0.1401 0.6401 0)	267.75
GGA(PBE)	6.445	7.691	(0.1274 0.6274 0)	379.07
Expt [7]	6.541	8.091	(0.1268 0.6268 0)	346.17

that these functionals are not suitable for description of crystal structures of the metal azides. In comparison with experimental results, the functional PBE+G06 underestimates the value of 'a' by -0.1% for KN_3 and overestimates by 0.7% for RbN_3. However, the results obtained by the dispersion corrected functionals are consistent with the trend reported in previous literature on molecular solids [33]. For the case of lattice parameter 'c', the functionals followed their general trends with LDA (OBS) results in large errors of about -9.3% for KN_3 and -7.1% for RbN_3. Both GGA (PBE) and GGA (PBE+G06) predicted the lattice constant 'c' with error of about 1.5%, -1.8% for KN_3 and 2.2%, -1.4% for RbN_3, respectively.

Overall, the best qualitative agreements between the experimental results and theory for the lattice parameters of alkali metal azides is achieved by the PBE+G06 functional. Therefore from the present study of crystal structures of the metal azides using various functionals we propose that PBE+G06 functional give best

results and it can be employed for the structural description of the other metal azides also for future studies [34–36].

3.3.2 Elastic properties

Elastic constants are the most important entities in describing the mechanical response of materials. In particular, they are of great importance to understand the response of energetic materials towards the external stimuli such as mechanical shock and thereby their initial step of decomposition or detonation phenomena. Moreover, the knowledge of elastic constants is essential to understand the high pressure behavior of the materials. Since the elastic properties are strongly related to the lattice parameters optimization results, we use the PBE+G06 functional for the calculation of the elastic constants and compare the results with usual PBE calculations. According to Hooke's law, for a given small strain applied to the lattice the stress components can be calculated using,

$$\sigma_{ij} = C_{ijkl}\epsilon_{kl} \tag{3.2}$$

where σ_{ij} is the stress tensor, ϵ_{kl} is the strain tensor and C_{ijkl} is the elastic stiffness tensor. By following the Voigt's notation [37], this equation can be reduced to

$$\sigma_i = C_{ij}\epsilon_j \quad with \quad i = 1-6, j = 1-6 \tag{3.3}$$

where *xx, yy, zz, yz, xz, xy* replaced by 1, 2, 3, 4, 5, 6 respectively and therefore C_{ij} form a 6x6 matrix.

Due to the structural symmetry, the maximum number of independent parameters can be reduced to thirteen for the monoclinic lattice namely C_{11}, C_{22}, C_{33}, C_{44}, C_{55}, C_{66}, C_{12}, C_{13}, C_{15}, C_{23}, C_{25}, C_{35}, and C_{46} and six for tetragonal structure C_{11}, C_{12}, C_{13}, C_{33}, C_{44}, and C_{66}. We have calculated thirteen independent elastic constants of monoclinic LiN_3 and NaN_3 as well as the six elastic constants of tetragonal KN_3, RbN_3 and CsN_3 systems using PBE and PBE+G06 functionals and are presented in Table 3.3 and 3.4 respectively. Clearly, the calculated elastic constants follow the Born-Huang mechanical stability criterion for a monoclinic

system and tetragonal system [38] indicating that all the compounds are mechanically stable. The present results are in good agreement with those calculated from the rigid ion model [39] as well as the ultrasonic measurements on KN_3 [40]. There are no experimental data available to compare the calculated elastic constants of monoclinic LiN_3, NaN_3 and tetragonal RbN_3, CsN_3.

TABLE 3.3: Single crystal elastic constants C_{ij}, in GPa, of monoclinic LiN_3 and NaN_3 calculated using PBE and PBE+G06 functionals.

Compd	PBE+G06	PBE
LiN_3	C_{11}=92.2, C_{22}=77.3, C_{33}=116.6, C_{44}=13.3, C_{55}=36.3, C_{66}=22.3 , C_{12}=21.4, C_{13}=37.9, C_{15}=19.9, C_{23}=30.2, C_{25}=2.9, C_{35}=41.4, C_{46}=-6.1	C_{11}=56.1, C_{22}= 48.1, C_{33}=102.9, C_{44}=9.6, C_{55}=15.2, C_{66}=19.6, C_{12}=19.6, C_{13}=27.9, C_{15}=6.1, C_{23}=19.5, C_{25}=2.6, C_{35}=41.1, C_{46}=-1.7
NaN_3	C_{11}=64.6, C_{22}=31.2, C_{33}=62.1, C_{44}=7.2, C_{55}=21.9, C_{66}=8.6, C_{12}=10.8, C_{13}=27.8, C_{15}=21.3, C_{23}=16.5, C_{25}=1.9, C_{35}=18.6, C_{46}=-2.9	C_{11}=38.1, C_{22}=30.9, C_{33}=65.2, C_{44}=5.7, C_{55}=12.9, C_{66}=8.8, C_{12}=10.4, C_{13}=25.1, C_{15}=5.4, C_{23}=16.3, C_{25}=0.4, C_{35}=17.3, C_{46}=-3.1

For crystals with vdW interactions, one can correlate the elastic constant values with the structural properties of the crystal. The elastic constants C_{11}, C_{22}, and C_{33} can be directly relate to the crystallographic a, b and c-axes respectively [34]. From the calculated elastic constants of alkali metal azides it can be noticed that there is a considerable elastic anisotropy among the principal crystallographic

TABLE 3.4: Single crystal elastic constants, C_{ij} in GPa, of MN_3 (M=K, Rb, Cs) calculated using PBE and PBE+G06 functionals.

Method	C_{11}	C_{12}	C_{13}	C_{33}	C_{44}	C_{66}
			KN_3			
GGA(PBE)	39.4	15.3	7.5	31.7	7.3	18.6
GGA(PBE+G06)	54.5	23.1	16.4	37.3	15.3	20.2
Expt[40]	49.5	13.9	11.7	32.3	8.8	13.1
			RbN_3			
GGA(PBE)	30.4	12.4	7.7	27.4	6.8	13.1
GGA(PBE+G06)	43.3	17.8	17.6	36.3	15.1	13.1
			CsN_3			
GGA(PBE)	23.2	10.6	7.7	24.3	5.7	9.5

TABLE 3.5: The minimum non-bonded distance (Å) of M-M, M-N, and N-N (M=Li, Na, K, Rb and Cs) of alkali metal azides calculated using PBE (PBE+G06) functionals.

Bond	LiN_3	NaN_3	KN_3	RbN_3	CsN_3
$M-M$	3.334 (3.258)	3.727 (3.571)	3.604 (3.481)	3.846 (3.706)	4.124
$M-N$	2.314 (2.200)	2.563 (2.488)	3.002 (2.982)	3.164 (3.078)	3.356
$N-N$	3.334 (3.258)	3.727 (3.571)	3.169 (3.096)	3.338 (3.255)	3.540

TABLE 3.6: Polycrystalline elastic moduli namely Bulk moduli B, Shear moduli G, Young's moduli E (in GPa) of alkali metal azides calculated using PBE and PBE+G06 functionals.

Compd	B_V	B_R	B_H	G_V	G_R	G_H	E
PBE+G06							
LiN_3	51.7	38.8	45.2	27.5	19.1	23.3	59.7
NaN_3	29.8	22.1	25.9	14.4	8.9	11.7	30.5
KN_3	28.6	27.2	27.9	16.2	15.7	15.9	40.1
RbN_3	25.4	25.2	25.3	13.3	13.1	13.2	33.7
PBE							
LiN_3	36.1	25.7	30.9	18.6	10.7	23.3	59.7
NaN_3	26.4	20.8	23.6	10.9	7.3	14.6	–
KN_3	19.0	18.4	18.7	11.9	10.4	11.2	28.0
RbN_3	15.9	15.8	15.9	9.4	8.7	9.1	22.9
CsN_3	13.6	13.6	13.6	7.2	6.8	7.0	17.9

directions due to the fact that $C_{11} \neq C_{22} \neq C_{33}$ for monoclinic LiN_3 and NaN_3 azides whereas $C_{11} \neq C_{33}$ for the tetragonal azides KN_3, RbN_3 and CsN_3. In the case of LiN_3 and NaN_3, the calculated values of these three constants follows the order $C_{33} > C_{11} > C_{22}$, which implies that the elastic constant C_{22} is the weakest in these systems. This reveals the fact that a relatively low number of lattice interactions are present along the crystallographic 'b'-axis and therefore the lattice would respond first along b-axis to the external mechanical perturbation in these azides. From the calculated elastic constants of tetragonal KN_3, RbN_3 and CsN_3 one can clearly notice that C_{11} is the largest among all the other elastic constants. This reflects the fact that the presence of stronger inter molecular interactions along the a-direction or the presence of lowest number of interactions along the c-axis. Therefore it is c-axis that responds first to external mechanical perturbation in these azides [36].

Over all from the calculated elastic constants of alkali metal azides C_{11}, C_{22}, and C_{33}, one can notice that the magnitude of the elastic constants follows the order of CsN_3 < RbN_3< KN_3< NaN_3< LiN_3, which implies that LiN_3 is mechanically stiffer system compared to other azides. The possible reason for this is as follows: the calculated minimum non-bonded distances between M-M, M-N (M=Li, Na, K, Rb and Cs) and N-N using PBE and PBE+G06 are presented in Table 3.5. From the calculated values, one can find that the distances between the atoms increase from LiN_3 to CsN_3, which implies that the interactions among the atoms are weakened as the size of the metal atom increases, hence the stiffness decreases from LiN_3 to CsN_3 [36]. As a matter of fact, it is worth to describe the mechanical response of polycrystalline materials. The calculated elastic constants of the alkali metal azides will be useful to obtain the macroscopic mechanical properties via Voigt-Reuss-Hill approach [41]. The obtained values of bulk moduli (B), shear moduli (G) and Young's moduli (E) both in PBE and PBE+G06 functional are tabulated in Table 3.6. The macroscopic elastic moduli of LiN_3 is larger than those of other alkali metal azides implying that Lithium azide is stiffer material among the alkali azides.

Recently Haycraft et al. [42] made a correlation of elastic constants of secondary explosives RDX and HMX with their detonation. Their study reveals that RDX has larger elastic constants over HMX implying that RDX is more stiffer system compared to HMX and therefore concluded that HMX is more sensitive towards mechanical shock than that of RDX. This is in very good agreement with the fact that HMX is more sensitive towards shock initiated detonation than RDX. In the case of PETN and RDX, the elastic constants of PETN crystal [43] are found to be much smaller than those of RDX and PETN is found to be more sensitive than RDX towards shock initiation. Moreover, among the elastic constants of PETN, C_{11} is found to be the stiffest elastic constant (larger in magnitude) and thereby the detonation is less sensitive along the [1 0 0] direction [44]. By taking the reference of these studies on correlation of elastic constants with the detonation sensitivity of solid energetic materials, in this present work we have made an attempt to understand the decomposition of the metal azides under present study. From the calculated elastic constants of the metal azides, it was found that the elastic constants of LiN_3 are larger compared to those of other azides NaN_3, KN_3,

RbN_3 and CsN_3. They follows the order of CsN_3 < RbN_3< KN_3< NaN_3< LiN_3, implying that LiN_3 is mechanically stiffer system than the other metal azides. This fact also supported from the calculated bulk elastic moduli namely E, B, G of the azides. In addition, the monoclinic azides are found to be stiffer along c-axes followed by a and b-axes whereas tetragonal azides are stiffer along a-axis followed by c-axis. Therefore the lattice can be easily compressed along b-axes over other axes for LiN_3 and NaN_3 and it is c-axis for KN_3 > RbN_3 > CsN_3. This clearly shows that the lattices are most sensitive towards the external stimuli along the [0 1 0] and [0 0 1] crystallographic direction in these azides. Over all from our study based on elastic constants and different elastic moduli reveals that CsN_3 is more sensitive towards the mechanical shock initiation over other alkali metal azides [36].

3.3.3 Electronic band structure

In the case of metal azides it is quite necessary to know about the electronic structure and related properties as they give important information regarding the electronic processes that are responsible for the decomposition and initiation of the metal azides [2]. The electronic band structure of alkali metal azides calculated within PBE+G06 functional are shown in Figure 3.2 and 3.3. The band structure of monoclinic alkali metal azides, LiN_3 and NaN_3 clearly shows that the top of the valence band and the bottom of the conduction band occurs at Z-point in the Brillouin zone indicating the materials are direct band gap materials with a separation of 3.48 eV for LiN_3 [35] and 3.36 eV for NaN_3 [34] within PBE+G06 functional as shown in Figure 3.2(a) and 3.2(b) respectively. Whereas the tetragonal alkali metal azides KN_3, RbN_3 and CsN_3 are also found to be direct band gap materials [36] as the top of the valence band and the bottom of the conduction band occurs at Γ-point in the Brillouin zone as shown in Figure 3.3(a), 3.3(b) and 3.3(c) respectively. The calculated band gap values within PBE and PBE+G06 functionals are shown Table 3.7. However, it is very well known that the usual density functional calculations result in underestimation of band gap by 30-40 % [14]. To overcome the band gap problem, recently developed TB-mBJ functional in WIEN2k package has been widely used in the literature [45] as it takes less computational time when compared to the very expensive GW calculations [46].

TABLE 3.7: Band gap, in eV, of MN_3 (M=Li, Na, K, Rb, Cs) calculated within GGA (PBE) and GGA (PBE+G06), EV, TB-mBJ functionals.

Compd	PBE	PBE+G06	EV	TB-mBJ
LiN_3	3.32	3.48	4.39	4.98
NaN_3	3.69	3.36	4.27	5.38
KN_3	4.06	4.08	4.78	5.95
RbN_3	3.99	4.07	4.68	5.98
CsN_3	4.07	–	4.57	5.67

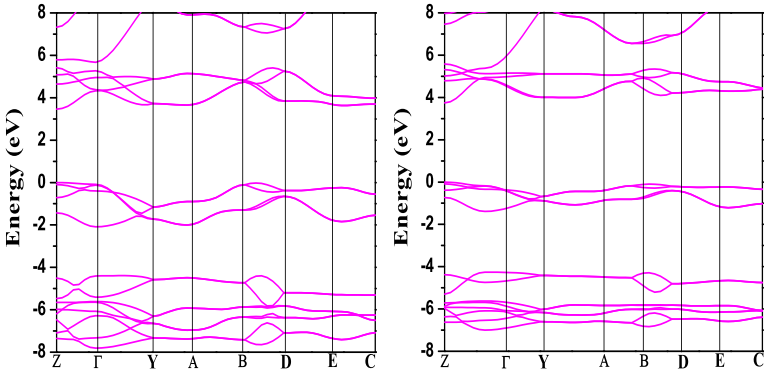

(a) (b)

FIGURE 3.2: Energy band structure of monoclinic alkali metal azides (a) LiN_3 (b) NaN_3 calculated within PBE+G06 functional at theoretical equilibrium volume.

In this present study, we have calculated the band gap energies of alkali metal azides by using TB-mBJ functional in addition to the other exchange-correlation functionals that are available in WIEN2k package. The calculated band gap values are presented in the Table 3.7 along with those calculated from CASTEP package.

There are no experimental band gap values to compare the present band gap values. However, it is well known that the TB-mBJ functional provides the band gap values that are in close agreement with the experiments [45], we expect our present values will be useful for further studies on these compounds. As the band gap lies in Ultra-Violet (UV) region, the compounds release N_2 gas when they irradiated with the UV light.

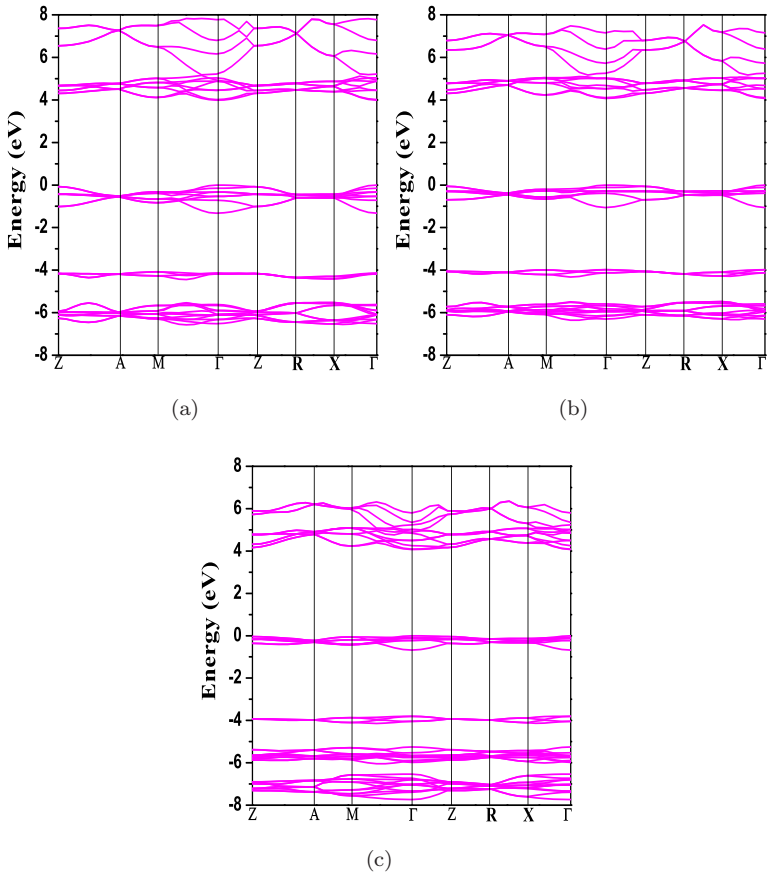

FIGURE 3.3: Energy band structure of tetragonal alkali metal azides (a) KN_3 (b) RbN_3 (c) CsN_3 calculated within PBE+G06 functional at theoretical equilibrium volume.

3.3.4 Total and partial density of states

The nature of bonding can be well understood by the knowledge of total and partial density of states as they clearly gives the idea of the origin of various bands in terms of atoms and orbitals. Moreover, alkali metal azides are photosensitive and undergo decomposition under the action of suitable wave length of light and the essential step in the photo chemical decomposition involves the promotion of a valence electron from the valence band to the conduction band, therefore it would be necessary to know the information about the type of states that are present in both valence and conduction bands.The total and partial density of states of the metal azides calculated using PBE+G06 functional are shown in Figure 3.4 and 3.5. The valence band spectra and the conduction band spectra of the metal azides show similar features. In the valence band region, there are three regions

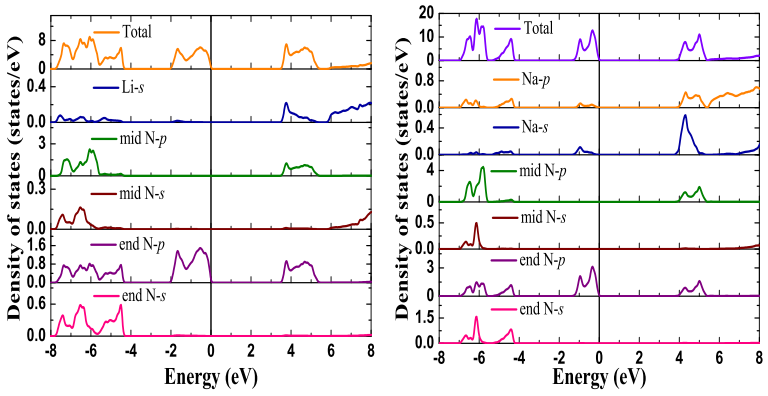

(a) (b)

FIGURE 3.4: Total and partial density of states of monoclinic alkali metal azides (a) LiN_3 (b) NaN_3 calculated within PBE+G06 functional at theoretical equilibrium volume.

of bands separated by large gaps which is also evidenced from the energy band structure of the metal azides. There is a strong hybridization between the mid nitrogen atom states and the end nitrogen atom states in the lower energy region of the valence band i.e., from -4 eV to -6.5 eV. This indicates that the nitrogen atoms are in strong covalent bonding in the azide ion whereas the metal atom states are dominant in the conduction band and there is low overlap of the states with the nitrogen atom states in the valence band, a feature that ionic bonding preserves between the metal atom and the nitrogen atoms. At the Fermi level, the '*p*'-states of the end nitrogen atom are only present implying that these states are responsible for decomposition of the azides for an external perturbation [34].

A quantitative picture of the bonded interactions can be obtained from the Mulliken bond population analysis [47]. The total overlap (bond) population for any pair of atoms in a molecule is in general made up of positive and negative contributions. If the total overlap population between two atoms is positive, they are bonded; if it is negative, they are anti-bonded. The computed Mulliken bond population of Li-N is -0.26, Na-N is -0.28, K-N is -0.38, Rb-N is -0.17 and that of Cs-N is -0.21 whereas the same for N-N is 1.18, 1.00, 1.31, 1.29 and 1.19 of LiN_3, NaN_3, KN_3, RbN_3 and CsN_3 respectively. The computed Mulliken charges for individual atoms are as follows: Li (0.98) and N (-0.56) for LiN_3, Na (0.92) and N (-0.48) for NaN_3, K (1.11) and N (-0.55) for KN_3, Rb (1.08) and N (-0.53) for RbN_3

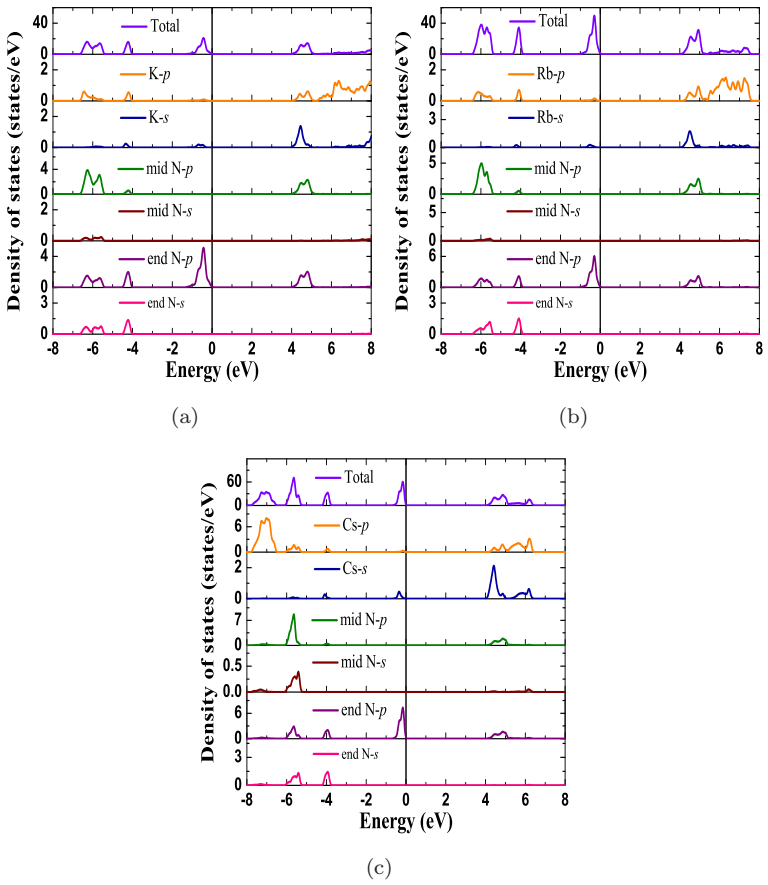

FIGURE 3.5: Total and partial density of states of tetragonal alkali metal azides (a) KN_3 (b) RbN_3 (c) CsN_3 calculated within PBE+G06 functional at theoretical equilibrium volume.

and for CsN_3 they are Cs (1.02) and N (-0.51). This indicates that alkali metal atoms are act as electron donors while the nitrogen atoms are act as electron acceptors. This feature can be expected due to the high electronegativity of N atom (3.04) and high electropositive alkali metal atoms. These results strongly suggest that all the metal azides are dominantly ionic in nature and the ionicity increases in the order $LiN_3 < NaN_3 < KN_3 < RbN_3 < CsN_3$.

3.3.5 Optical properties

Alkali metal azides become unstable and undergoes decomposition by the action of light. The photo chemical decomposition of the azides can be understood by the optical transitions from the valence band to the conduction band. From the

total and partial density of states (DOS) the states lying near the Fermi level are essentially the p states of azide ion, therefore the decomposition of the metal azides can be initiated by the formation of azide radicals in the following way.

$$N_3^- + h\upsilon \rightarrow N_3^* \tag{3.4}$$

$$N_3^* + E \rightarrow N_3 + e^- \tag{3.5}$$

where E is the thermal energy required to dissociate the azide radical $N_3{}^*$. The combination of two positive holes will give nitrogen gas with the liberation of energy Q and the electron trapped to the metal atom sites and thereby form the metal atom

$$2N_3 \rightarrow 3N_2 + Q \tag{3.6}$$

$$M^+ + e^- \rightarrow M \tag{3.7}$$

where 'M' is metal atom. Therefore in order to understand the photochemical decomposition phenomena it would be necessary to understand its optical properties that are resulting from the interband transitions. In general the optical properties of matter can be described by means of the complex dielectric function $\epsilon(\omega) = \epsilon_1(\omega) + i\epsilon_2(\omega)$, where $\epsilon_1(\omega)$ and $\epsilon_2(\omega)$ describes the dispersive and absorptive parts of the dielectric function. Normally there are two contributions to $\epsilon(\omega)$ namely intraband and interband transitions. The contribution from intraband transitions is important only for the case of metals. The interband transitions can further be split into direct and indirect transitions. The indirect interband transitions involve scattering of phonons. But the indirect transitions give only a small contribution to $\epsilon(\omega)$ in comparison to the direct transitions, so we neglected them in our calculations. The direct interband contribution to the absorptive or imaginary part $\epsilon_2(\omega)$ of the dielectric function $\epsilon(\omega)$ in the random phase approximation without allowance for local field effects can be calculated by summing all the possible transitions from the occupied and unoccupied states with fixed k-vector over the Brillouin zone and is given as [48]

$$\epsilon_2(\omega) = \frac{Ve^2}{2\pi\hbar m^2\omega^2} \int d^3k \sum |\langle\psi_C|p|\psi_V\rangle|^2 \delta(E_C - E_V - \hbar\omega) \tag{3.8}$$

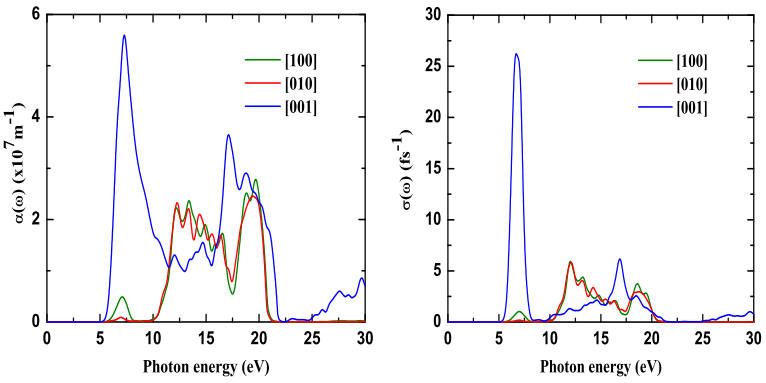

(a) (b)

FIGURE 3.6: Optical absorption spectra of LiN_3 (a) and Photoconductivity of LiN_3 (b) calculated within the PBE+G06 functional with a scissors operator of 1.5 eV.

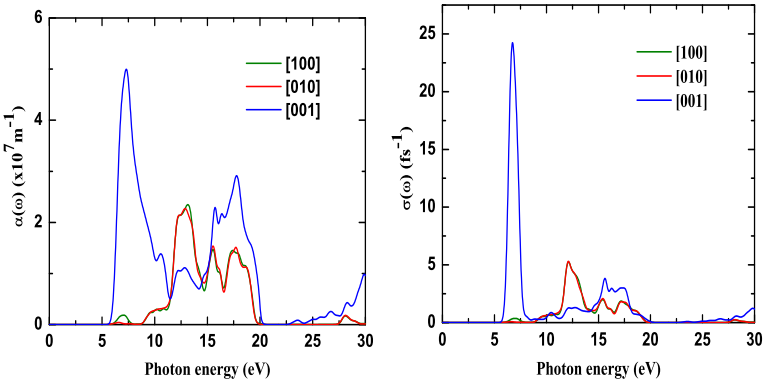

(a) (b)

FIGURE 3.7: Optical absorption spectra of NaN_3 (a) and Photoconductivity of NaN_3 (b) calculated within the PBE+G06 functional with a scissors operator of 2.02 eV.

here ψ_C and ψ_V are the wave functions in the conduction and valence bands, p is the momentum operator, ω is the photon frequency, and $\hbar$ is reduced Planck's constant. The real part ϵ_1 (ω) of the dielectric function can be evaluated from ϵ_2 (ω) by using the Kramer-Kroning relations.

$$\epsilon_1(\omega) = 1 + \frac{2}{\pi} P \int_0^{\infty} \frac{\epsilon_2(\omega')\omega' d\omega'}{(\omega')^2 - (\omega)^2} \tag{3.9}$$

where 'P' is the principle value of the integral. The knowledge of both the real and imaginary parts of the dielectric function allows the calculation of the important

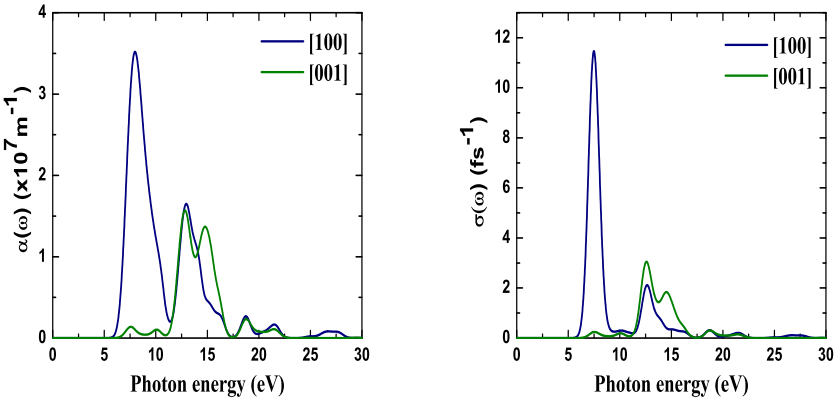

(a) (b)

FIGURE 3.8: Optical absorption spectra of KN_3 (a) and Photoconductivity of KN_3 (b) calculated within the PBE+G06 functional with a scissors operator of 1.87 eV.

optical properties such as refractive index $n(\omega)$, absorption $\alpha(\omega)$ and photoconductivity $\sigma(\omega)$ [48] through the following expressions

$$n(\omega) = \frac{1}{\sqrt{2}}\left[\sqrt{\epsilon_1(\omega)^2 + \epsilon_2(\omega)^2} + \epsilon_1(\omega)\right]^{\frac{1}{2}} \tag{3.10}$$

$$\alpha(\omega) = \sqrt{2}\omega\left[\sqrt{\epsilon_1(\omega)^2 + \epsilon_2(\omega)^2} - \epsilon_1(\omega)\right]^{\frac{1}{2}} \tag{3.11}$$

$$\sigma(\omega) = \frac{-i\omega}{4\pi}\left[\epsilon(\omega) - 1\right] \tag{3.12}$$

In Figure 3.6 (a), 3.7 (a), we have shown the calculated absorption spectra along [100], [010], and [001] directions for LiN_3, NaN_3 respectively and along [100], [001] directions for the rest of the azides in Figure 3.8 (a), 3.9 (a) and 3.10 (a) respectively. Our calculated results indicates that there is anisotropy in the calculated optical spectra. The peaks in the absorption spectra are due to the interband transitions from the occupied to unoccupied states. Since the 'p'-states of end nitrogen atom are dominating at the Fermi level, the transitions would be from 'p' of N to s states of metal atom that are present in the conduction band (N $p \rightarrow$ M

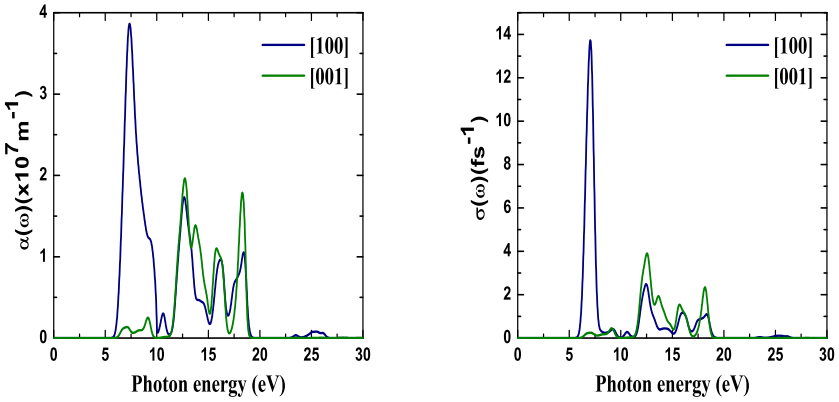

(a) (b)

FIGURE 3.9: Optical absorption spectra of RbN_3 (a) and Photoconductivity of RbN_3 (b) calculated within the PBE+G06 functional with a scissors operator of 1.91 eV.

s where M is alkali metal atom). For all the metal azides, the optical absorption starts at the band gap values. As the optical edge starts at 4.98 eV in LiN_3, at 5.38 eV in NaN_3, 5.95 eV in KN_3, 5.98 eV in RbN_3 and 5.67 eV in CsN_3 and also the absorption coefficient is of the order of 10^7 m^{-1} we conclude that lithium azide will undergo decomposition by the irradiation of Ultraviolet light with wave length of 248.9 nm, sodium azide with that of 230.5 nm, potassium azide with 208.4 nm, rubidium azide with 207.3 nm and cesium azide with 218.7 nm respectively [34].

Photoconductivity is due to the increase in number of free carriers when photons are absorbed. The photons must have sufficient energy to excite the electrons from the valence band to the conduction band. In the present case of alkali metal azides, the calculated photoconductivity show a wide photocurrent response in the absorption region of 4.9 to 20 eV as shown in Figure 3.6 (b), 3.7 (b) for LiN_3 NaN_3 and in Figure 3.8 (b), 3.9 (b) and 3.10 (b) for KN_3, RbN_3 and CsN_3 respectively. This implies that alkali metal azides are photosensitive materials. Especially the metal azides have strong photocurrent response in between 4.4 eV to 10 eV.

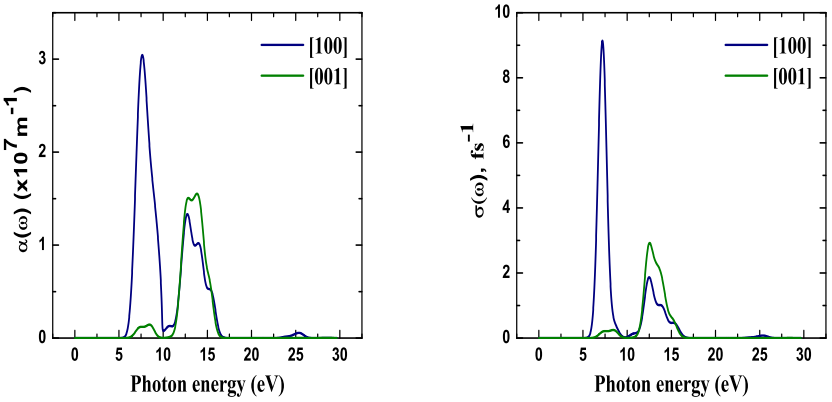

(a) (b)

FIGURE 3.10: Optical absorption spectra of CsN_3 (a) and Photoconductivity of CsN_3 (b) calculated within the PBE functional with a scissors operator of 1.6 eV.

3.3.6 Phonon density of states and Phonon frequencies at Γ-point

In this section we will discuss about the calculated phonon density of states and phonon frequencies at gamma point of the metal azides under study. The phonon density of states calculated through the density functional perturbation theory [23, 24]. In this method the force constants matrix can be obtained by differentiating the Hellmann-Feynman forces on atoms with respect to the ionic co-ordinates. This means that the force constant matrix depends on the ground state electron charge density and on its linear response to a distortion of atomic positions. By variational principle, the second order change in energy depends on the first order change in the electron density and this can be obtained by minimizing the second order perturbation in energy which gives the first order changes in the density, wave functions, and potential. In the present study, the dynamical matrix elements are calculated on the 5x8x5 grid of k-points using the linear response approach. The calculated phonon density of states for LiN_3, NaN_3 [34] are shown in Figure 3.11 (a) and 3.11 (b) respectively while those of KN_3, RbN_3 and CsN_3 are presented in Figure 3.12(a), (b) and (c) respectively. It can be seen that in all the metal azides, the lower frequency region states are dominated by the metal atom whereas the

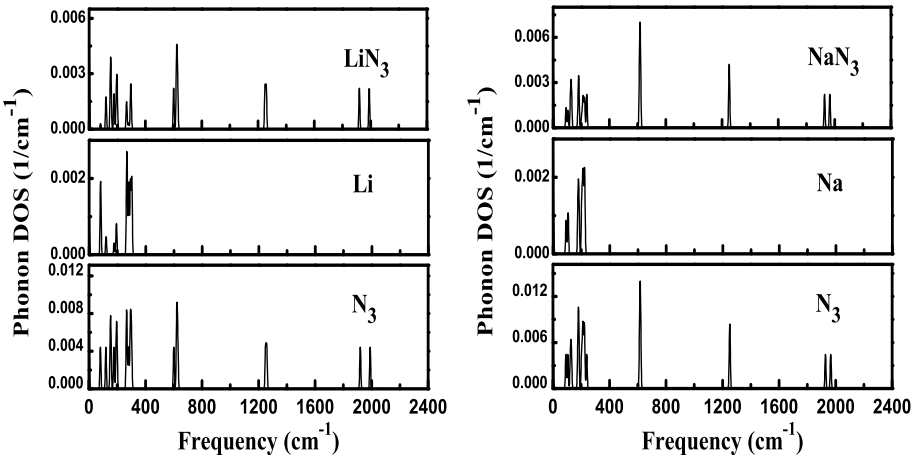

(a) (b)

FIGURE 3.11: Phonon density of states of (a) LiN_3 (b) NaN_3 calculated within PBE+G06 functional at theoretical equilibrium volume.

TABLE 3.8: The calculated vibrational frequencies of monoclinic LiN_3 and NaN_3 at ambient pressure calculated within PBE (PBE+G06) functionals. Values in parenthesis are from experiment.

Mode Symmetry	Frequency (cm^{-1})	Frequency (cm^{-1})
	LiN_3	NaN_3
B_u	138 (122.1)	120.7 (135.7)
B_g	191.6 (182.4)	147.4 (171.2)
A_g	212.2 (198.3)	157.6 (179.7)
A_u	220.7 (273.3)	160.4 (201.5)
B_u	264.6 (296.8)	188.1 (216.7)
B_u	645.4 (602.8)	612.1 (612.2)
A_u	661.3 (619.1)	612.3 (615.7)
A_g	1262.3 (1259.1)	1236.8 (1251.5)
B_u	2006.5 (1988.8)	1950.7 (1964.8)

higher frequency region are entirely due to the azide ion alone, the fact can be attributed to the difference in their individual masses.

The important point to be notice from the phonon density of states below 400 cm^{-1} is that the states of metal atom and azide ion are overlapping each other. This implies that the vibrations are due to the collective excitations of both metal and azide ion respectively. The calculated vibrational frequencies for monoclinic alklai metal azides and for the tetragonal metal azides at gamma point are shown in Table 3.8 and Table 3.9, 3.10, and 3.11 respectively. The group symmetry

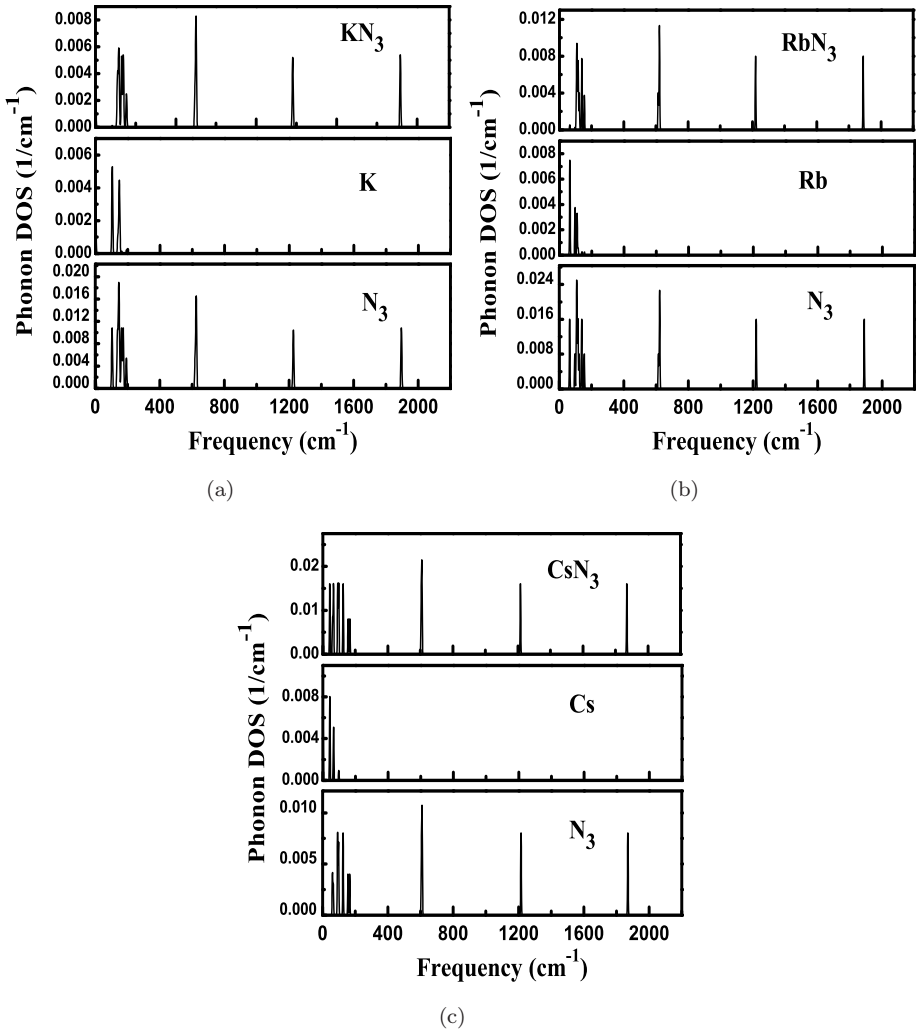

FIGURE 3.12: Phonon density of states of (a) KN_3 (b) RbN_3 (c) CsN_3 calculated within PBE+G06 functional at theoretical equilibrium volume.

decomposition into irreducible representations of the C2/m point group yields a sum of A_u+2B_u for three acoustic modes and 2A_g+1B_g+2A_u+4B_u for the 9 optical modes. The modes below 300 cm^{-1} involves the vibrations from the lattice (including both metal atom and azide ion) whereas modes above 600 cm^{-1} are entirely due to the azide ion. The B_u mode, which has the frequency 602.8 cm^{-1} for LiN_3 and 612.2 cm^{-1} for NaN_3, is due to the N_3 symmetric bending along b-axis and it is in good agreement with that of the experimental reported value [2]. The A_u mode, located at 619.1 cm^{-1} for LiN_3 and 615.7 cm^{-1} for NaN_3 originates from the asymmetric bending of azide ion along a-axis. Our calculated value of 1259.1 cm^{-1} for LiN_3 and 1251.5 cm^{-1} for NaN_3, which describes the symmetric

TABLE 3.9: The calculated vibrational frequencies (cm^{-1}) of tetragonal KN_3 at ambient pressure within PBE and PBE+G06 functionals. T and R corresponds to Translational and Rotational vibrations respectively. IA and RA infers the Infrared active and Raman active modes of KN_3.

Mode symmetry	Frequency (cm^{-1})		Expt
	PBE	PBE+G06	
E_g(T) (RA)	89.8	103.8	103[50]
$B_{1u}(T)$	104.9	136.5	
B_{1g}(R) (RA)	106.1	139.2	
A_{2u}(T) (IA)	109.6	144.1	138.2[49]
E_u(T) (IA)	114.7	146.2	
E_g(R) (RA)	131.5	149.4	145[50]
A_{2g}(T)	134.9	162.8	
E_u(T) (IA)	155.5	173.4	168[49]
A_{2g}(R)	162.3	192.2	
A_{2u} (IA)	617.2	618.2	627[53]
			643[54]
			624[55]
B_{1u}	623.1	625.3	
E_u	623.6	626.3	624[53]
			647[54]
			646[55]
B_{2g} (RA)	1219.1	1226.3	1339[50]
A_{1g} (RA)	1220.7	1228.5	1340[50]
E_u (IA)	1883.7	1896.1	2002.2[55]

stretching of azide ion is in good agreement with that of the experimental value of 1277 cm^{-1} [2]. The asymmetric stretching frequency of azide ion is found to be 1988.8 cm^{-1}, which is lower than that of experimental value 2092 cm^{-1}.

In the case of KN_3, RbN_3 and CsN_3, the primitive cell consists of eight atoms and hence they have 24 vibrational modes out of which three are acoustic modes and 21 are optical modes. According to the symmetry analysis of the point group D_{4h}, the acoustic and optical modes at the Γ point can be classified into the following symmetry species:

$\Gamma_{aco} = A_{2u} + 2E_u$

$\Gamma_{opt} = 2A_{2g} + 2A_{2u} + A_{1g} + 4E_g + 8E_u + B_{1g} + 2B_{1u} + B_{2g}$

TABLE 3.10: The calculated vibrational frequencies (cm^{-1}) of tetragonal RbN_3 at ambient pressure within PBE and PBE+G06 functionals. T and R corresponds to Translational and Rotational vibrations respectively. IA and RA infers the Infrared active and Raman active modes of RbN_3.

Mode symmetry	Frequency (cm^{-1})		Expt
	PBE	PBE+G06	
E_g(T) (RA)	56.2	64.8	66[50]
$B_{1u}(T)$	85.5	96.3	
B_{1g}(R) (RA)	104.8	105.9	
A_{2u}(T) (IA)	119.2	107.6	108[49]
E_u(T) (IA)	131.5	109.3	
E_g(R) (RA)	149.3	115.3	157[50]
A_{2g}(T)	153.8	122.6	
E_u(T) (IA)	155.2	139.2	168[49]
A_{2g}(R)	179.1	155.1	
A_{2u} (IA)	615.7	614.6	624.5[55]
B_{1u}	618.9	619.9	
E_u	621.4	621.8	643.5[55]
B_{2g} (RA)	1214.8	1219.1	–
A_{1g} (RA)	1215.8	1220.3	1333[50]
E_u (IA)	1877.9	1888.7	2008[55]

Out of these modes, the A_{2g} vibrations are silent as they do not cause a change in polarizability or dipole moment and therefore these modes are optically inactive. The modes A_{1g}, B_{2g}, and B_{1g} are Raman active (RA) whereas the A_{2u}, B_{1u}, and E_{1u} modes are infrared active (IA). The vibrational frequencies calculated at the theoretical equilibrium volume using PBE and PBE+G06 functionals are presented in Table 3.9 and 3.10 for KN_3 and RbN_3 respectively along with the experimental data. Since the metal azide crystal consists of tightly bounded azide ions which are loosely bounded to metal atoms, the vibrations involving the nitrogen atoms of azide ion could be labeled as internal vibrations and the external or lattice vibrations are those in which the azide ion move as rigid units along with the metal ion sub lattice. The calculated frequencies ranging from 89 cm^{-1} to 192 cm^{-1} of KN_3 and 56 cm^{-1} to 179 cm^{-1} of RbN_3 are due to lattice mode vibrations. In the case of KN_3 and RbN_3, the results of PBE+G06 functional are in fair agreement with experiment [49–52] than PBE values. This is because the intermolecular van der Waals forces strongly couples in lattice modes which PBE could not take into

TABLE 3.11: The calculated vibrational frequencies (cm^{-1}) of tetragonal CsN_3 at ambient pressure within PBE functional. T and R corresponds to Translational and Rotational vibrations respectively. IA and RA infers the Infrared active and Raman active modes of CsN_3.

Mode symmetry	Frequency (cm^{-1})	Expt
E_g(T) (RA)	43.2	
$B_{1u}(T)$	60.4	
B_{1g}(R) (RA)	64.7	
A_{2u}(T) (IA)	66.2	
E_u(T) (IA)	91.2	
E_g(R) (RA)	97.5	
A_{2g}(T)	124.9	
E_u(T) (IA)	155.1	
A_{2g}(R)	165.7	
A_{2u} (IA)	604.4	
B_{1u}	607.1	
E_u	610.1	638[2]
B_{2g} (RA)	1215.1	
A_{1g} (RA)	1215.5	1328.6[2]
E_u (IA)	1869.9	

account. But, for the bending mode frequencies of internal modes due to the azide ions, we find a very good agreement with experiment [53–55] using both PBE and PBE+G06 functionals. This might be due to the fact that these vibrations are purely due to the motion of individual N atoms of each azide ion which are covalently bonded with each other. Hence both the functionals give similar frequencies compared to experimental data. However, the stretching mode frequencies of the azide ion ranging from 1200 cm^{-1} to 1900 cm^{-1} are underestimated by 8.4% for A_{1g} and B_{1g} modes (both are due to the symmetric stretching of azide ion) and the E_u mode (asymmetric stretching of azide ion) is underestimated by 8.4% in both the metal azides. This might be due to the fact that our present calculations are performed through the linear response approach which is solely based on the harmonic approximation and therefore the anharmonicity present in the higher frequencies which are mainly due to the azide ion could not be dealt efficiently with the calculations [36]. The calculated vibrational frequencies of CsN_3 using PBE functional are presented in Table 3.11. The modes from 43.2cm^{-1} to 165cm^{-1} are due to the lattice vibrations. The calculated azide ion mode frequencies are

in good agreement with experiment as observed for the PBE values of KN_3 and RbN_3.

3.4 Conclusions

In conclusion, we have studied the structural, electronic, optical, elastic and vibrational properties of energetic molecular crystals namely alkali metal azides LiN_3, NaN_3, KN_3, RbN_3 and CsN_3 . We have focussed our attention more towards the effect of van der Waals interactions on the structural properties, elastic stiffness tensor and vibrational frequencies of the metal azides. We find that all properties are improved to a great extent by the inclusion of vdW interactions in the calculations. In particular, PBE+G06 functional gives good results compared to other dispersion corrected functionals. The calculated elastic constants suggest that the metal azides are mechanically stable systems under normal conditions. The elastic constants of LiN_3 are larger in magnitude than the rest of alkali metal azides, implying that lithium azide is mechanically stiffest material among the alkali metal azides. This fact is also confirmed by the higher values of bulk modulus, shear modulus and Young's modulus of LiN_3. Overall from the study of elastic constants we can come to a conclusion that CsN_3 is more sensitive towards a mechanical shock as the compound has lower elastic moduli than KN_3. The absorption spectra and photo conductivity spectra have been calculated and found that the absorption peaks are in the ultra-violet energy region. Therefore we conclude that the decomposition of alkali metal azides is more favorable by the action of light (ultra violet). The vibrational frequencies, in particular the frequencies of lattice modes are well reproduced by the present van der Waals corrected density functional calculations. Whereas, the higher frequency modes which are entirely due to the vibration of azide ion are well described by both the standard DFT and van der Waals corrected DFT functionals.

References

[1] Audrieth, Chem. Rev. 15 (1934) 169.

[2] B. L. Evans, A. D. Yoffe, P. Gray, Chem. Rev. 59 (1959) 515.

[3] P. Gray, Q. Rev. Chem. Soc. 17 (1963) 441.

[4] H. D. Fair, and R. F. Walker, Energetic Materilas, vol 1, (1977) Plenum Press, New York.

[5] F. P. Bowden, A. D. Yoffe, Fast Reactions in Solids, Butterworth Scientific Publications, (1958) London, UK.

[6] G. E. Pringle, D. E. Noakes, Acta Cryst. B 24 (1968) 262.

[7] U. Z. M*ü*ller, Z. Anorg. Allg. Chem. 392 (1972) 159.

[8] M. Seel, A. B. Kunz, Int. J. Quantum. Chem. 39 (1991) 149.

[9] Ju Xuehai, Xiao Heming, Ji Guangfu, Chin. Sci. Bull. 47 (2002) 1180.

[10] A. B. Gordienko, Yu. N. Zhuravlev, A. S. Poplavnoi, Phys. Stat. Sol (b). 198 (1996) 707.

[11] A. B. Gordienko, Yu. N. Zhuravlev, A. S. Poplavnoi, Russ. Phys. J. 38 (1995) 1.

[12] Weihua Zhu, Jijun Xiao and Xiao Heming, Chem. Phys. Lett. 422 (2006) 117.

[13] Weihua Zhu, Jijun Xiao and Xiao Heming, J. Phys. Chem. B 110 (2006) 9856.

[14] M. C. Payne, M. P. Teter, D. C. Allan, T. A. Arias, J. D. Joannopoulos, Rev. Mod. Phys. 64 (1992) 1045.

[15] M. Segall, P. Lindan, M. Probert, C. Pickard, P. Hasnip, S. Clark, M. J. Payne, J. Phys:. Cond. Matt. 14 (2002) 2717.

[16] D. Vanderbilt, Phys. Rev. B. 41 (1990) 7892.

[17] G. Kresse, J. Furthmuller, Phys. Rev. B. 54 (1996) 11169.

[18] T. H. Fischer, J. Almolf, J. Phys. Chem. 96 (1992) 9768.

[19] D. M. Ceperley, B. J. Alder, Phys. Rev. Lett. 45(1980) 566.

[20] J. P. Perdew, A. Zunger, Phys. Rev. B. 23 (1981) 5048.

[21] J. P. Perdew, K. Burke, M. Ernzerhof, Phys. Rev. lett. 77 (1996) 3865.

[22] H. J. Monkhorst, J. Pack, Phys. Rev. B. 13 (1976) 5188.

[23] X. Gonze, Phys. Rev. B. 55 (1997) 10337.

[24] K. Refson, P. R. Tulip, S. J. Clarke, Phys. Rev. B. 73 (2006) 155114.

[25] F. Ortmann, F. Bechstedt, W. G. Schmidt, Phys. Rev. B 73 (2006) 205101.

[26] S. Grimme, J. Comp. Chem. 27 (2006) 1787.

[27] A. Tkatchenko, M. Scheffler, Phys. Rev. Lett 102 (2009) 073005.

[28] D. J. Singh and L. Nordstrom, Planewaves, Pseudopotentials, and the LAPW Method, 2nd ed. (Springer Verlag, Berlin, 2006).

[29] P. Blaha, K. Schwarz, G. Madsen, D. Kvasnicka, and J. Luitz, WIEN2k, An Augmented Plane Wave + Local Orbitals Program for Calculating Crystal Properties (K. Schwarz, Tech. Univ. Wien, Austria, 2001).

[30] E. Engel, S.H. Vosko, Phys. Rev. B 47 (1993) 13164.

[31] F. Tran and P. Blaha, Phys. Rev. Lett. 102 (2009) 226401.

[32] R.O. Jones, O. Gunnasson, Rev. Mod. Phys 61 (1989) 689.

[33] Ch. Bheema Lingam, K. Ramesh Babu, Surya P. Tewari, G. Vaitheeswaran, J. Comp. Chem 33 (2012) 987.

[34] K. Ramesh Babu, G. Vaitheeswaran, Chem. Phys. Lett. 586 (2013) 44.

[35] K. Ramesh Babu, G. Vaitheeswaran, 2013, Solid State Sciences, , 23, 17.

[36] G. Vaitheeswaran, K. Ramesh Babu, J. Chem. Sci 124 (2012) 1391.

[37] J. Nye, Oxford University Press, (1985) USA.

[38] M. Born and K. Huang, Dynamical Theory of Crystal Lattices (Oxford: Oxford University Press)(1998).

[39] Piotr Zielh'lskia and Christian Marzluf, J. Chem. Phys. 96 (1992) 1735.

[40] S. Haussuhl, Z. fur. Krist. 21 (1998) 155.

[41] R. Hill, Proc. Phys. Soc. Lond. A 65 (1952) 349.

[42] J. J. Haycraft, L. L. Stevens, and C. J. Eckhardt, J. Chem. Phys. 124 (2006) 024712.

[43] J. M. Winey and Y. M. Gupta, J. Appl. Phys 90 (2001) 1669.

[44] C. S. Yoo, N. C. Holmes, P. C. Souers, C. J. Wu, F. H. Ree, and J. J. Dick, J. Appl. Phys 88 (2000) 70.

[45] J. A. Camargo-Martinez and R. Baquero, Phys. Rev. B 86 (2012) 195106.

[46] Ch. B. Lingam, K. R. Babu, Surya P. Tewari, G. Vaitheeswaran, S. Lèbegue, Phys. Stat. Sol. Rap. Res. Lett. 5 (2011) 10.

[47] R. S. Mulliken, J. Chem. Phys 23 (1955) 1833.

[48] K. Ramesh Babu, Ch. Bheema Lingam, S. Auluck, Surya P. Tewari, G. Vaitheeswaran, J. Solid State Chem. 184 (2011) 343.

[49] N. E. Massa, S. S. Mitra, H. Prask, R. S. Singh, S. F. Trevino, J. Chem. Phys 67 (1977) 173.

[50] C.E. Hathaway, P. A. Temple, Phys. Rev. B 3 (1971) 3497.

[51] J. Bryant, R. L. Brooks III, J. Chem. Phys 43 (1965) 880.

[52] J. GovindaRajan, T. M. Haridasan, Phys. Lett. 28A 10 (1969) 701.

[53] R. T. Lamoureux, D. A. Dows, Spectrochimica Acta 31A (1979) 1945.

[54] Z. Iqbal, J. Chem. Phys 57 (1972) 2422.

[55] H. A. Papazian, J. Chem. Phys, 34 (1961) 1614.

Chapter 4

Alkaline-Earth Metal Azides

Abstract

In this chapter we present a detailed first principles study on the structural, elastic, electron and optical properties of energetic alkaline-earth metal azides $Ca(N_3)_2$, $Sr(N_3)_2$ and $Ba(N_3)_2$. All the calculations are carried out by means of plane wave pseudopotential method with and without including van der Waals interactions. The calculated ground state structural properties are improved to a greater extent by the inclusion of dispersion corrections, implies that the van der Waals interactions play a major role on the physical properties of these systems. The elastic constants and the related bulk mechanical properties of $Ca(N_3)_2$, $Sr(N_3)_2$ and $Ba(N_3)_2$ have been calculated and found that the compounds are mechanically stable systems. The magnitude of the calculated elastic constants increases in the order $Ba(N_3)_2 < Sr(N_3)_2 < Ca(N_3)_2$ implying higher elastic stiffness for $Ca(N_3)_2$, the fact also confirmed by the higher values of bulk, shear and Young's moduli of $Ca(N_3)_2$ than $Sr(N_3)_2$ and $Ba(N_3)_2$. A correlation has been proposed to relate the calculated elastic constants to the decomposition phenomena for the metal azides. The electronic band structures are calculated and found that the alkaline-earth metal azides are wide band gap insulators. The optical properties are calculated and analyzed through the electronic band structure.

4.1 Introduction

Inorganic metal azides show different kind of stability behaviour. Alkali metal azides are stable both to friction and to impact and undergo decomposition gently by heat at 300 to 400°C whereas heavy metal azides for example lead azide, copper azide, silver azide decompose with explosive violence when lightly struck or rubbed. Alkaline-earth metal azides are insensitive to friction and impact similar to alkali metal azides but undergo violent decomposition by heat at low temperatures below 110 to 160°C. One common feature in all these metal azides is they are sensitive to light because of the presence of azide anion. Alkaline-earth metal azides, $Sr(N_3)_2$ and $Ba(N_3)_2$ undergo photochemical decomposition into metal atom and nitrogen when they expose to ultra-violet light [1–3]. It is thus required to understand the basic physical and chemical properties of the alkaline-earth metal azides that govern the different phenomena occur in these solids.

The electronic band structure is quite essential to study the electron transfer mechanism that occur in alkaline-earth metal azides. Besides this the optical properties such as optical absorption and photoconductivity are necessary to address the photo response of these materials. In recent years much interest is focussed towards the high pressure behaviour of inorganic metal azides which are known as precursor materials to synthesize the polymeric nitrogen that contains single-bonded networks of nitrogen atoms [4–17]. Hence it is strongly required to know the mechanical stability of the metal azides and the elastic constants which give information about their compressibility behaviour.

In previous literature, there are limited number of studies available on the alkaline-earth metal azides. The electronic band structure and optical properties of $Sr(N_3)_2$ and $Ba(N_3)_2$ were reported through the first principles calculations with standard density functional methods [18]. But as we have seen in the case of alkali metal azides in chapter 3, the van der Waals (vdW) interactions play a major role on crystal binding and the related properties. Therefore the study of fundamental physical and chemical properties with dispersion corrected density functionals would thus require for proper description of the alkaline-earth metal azides. On the other hand, there are no studies available to explain the

mechanical stability and the elastic constants of alkaline-earth metal azides with and with out accounting the vdW interactions. Hence, in this chapter we aim to present a comparative study of structural, electronic, elastic and optical properties of alkaline-earth metal azides namely $Ca(N_3)_2$, $Sr(N_3)_2$ and $Ba(N_3)_2$.

4.2 Computational details

First-principles density functional theory calculations were performed with the Cambridge Sequential Total Energy Package (CASTEP) program [19, 20], using Vanderbilt-type ultrasoft pseudo potentials [21] and a plane wave expansion of the wave functions. The electronic wave functions were obtained using density mixing scheme [22] and the structures were relaxed using the Broyden, Fletcher, Goldfarb, and Shannon (BFGS) method [23]. The exchange-correlation potential of Ceperley and Alder [24] parameterized by Perdew and Zunger (CA-PZ) [25] in the local density approximation (LDA) and also the generalized gradient approximation (GGA) in Perdew-Burke-Ernzerhof (PBE) [26] was used to describe the exchange-correlation potential. The pseudo atomic calculations were performed for Ca $3s^2$ $3p^6$ $4s^2$, Sr $4s^2$ $4p^6$ $5s^2$, Ba $5s^2$ $5p^6$ $6s^2$ and N $2s^2$ $2p^3$. The Monkhorst-Pack scheme k-point sampling was used for integration over the Brillouin zone [27]. It is well known that the cut-off energy and k-point mesh influences the convergence of calculations. Hence we tested the dependence of energy cut-off and k-point grid and found that for 380 eV plane wave cut-off energy and 3x3x4 k-point mesh, the change in total energy is less than 1meV. We have then chosen these plane wave cut-off energy and k-point mesh for all the calculations. In the geometry relaxation, the self-consistent convergence on the total energy is $5\text{x}10^{-7}$ eV/atom and the maximum force on the atom is found to be 10^{-4} eV/Å. Elastic constants were calculated using finite strain technique as implemented in CASTEP code. We have used primitive cell that contains two molecules for the calculation of vibrational frequencies. To study the effect of van der Waals interactions, we have used the recently developed scheme by Grimme (G06) [28] approaches in GGA. These semiempirical approaches provide the best compromise between the cost of first principles evaluation of the dispersion terms and the need to improve non-bonding interactions in the standard DFT description. For the computation of electronic band gap, we use the recently developed Tran Blaha-modified Becke

Johnson potential [29] within linearized augmented plane wave (LAPW) method as implemented in WIEN2k package [30, 31].

4.3 Results and discussion

4.3.1 Crystal structure

Calcium azide and Strontium azide are isomorphous and crystallize in an orthorhombic structure with space group Fddd [32] and contain six molecules per unit cell as shown in Figure 4.1 (a). The crystal structure of Barium azide is monoclinic with space group P21/m [33] and contain two molecules per unit cell and is shown in Figure 4.1 (b). In the previous chapter on alkali metal azides we have used standard density functionals such as LDA(CA-PZ), GGA(PBE) and dispersion corrected density functionals CA-PZ+OBS, PBE+TS and PBE+G06 to study the structural properties. We found that PBE+G06 functional is efficient to describe the structural properties of metal azides. Therefore in this present study we use PBE+G06 functional to study the structural and related properties of alkali-earth metal azides. For the case of $Ba(N_3)_2$, there are no dispersion corrected functionals available for Ba atom hence we use PBE functional to describe the system. The calculated atomic fractional co-ordinates, bond lengths, equilibrium lattice parameters are presented in Table 4.1 together with the experimental data. The calculated values of lattice parameters are very close to experimental results.

The bulk modulus B_0 and its pressure derivative B_0' can be obtained from the equation of state fit of the calculated pressure-volume data of the crystal. In the present study we have calculated the P-V data of $Ca(N_3)_2$, $Sr(N_3)_2$, and $Ba(N_3)_2$ and are fitted to the Murnaghan's equation of state and the corresponding values are presented Table 4.1.

The bulk modulus B_0 and its pressure derivative $B_0\prime$ can be obtained from the equation of state fit of the calculated pressure-volume data of the crystal. In the present study we have calculated the P-V data of $Ca(N_3)_2$, $Sr(N_3)_2$, and $Ba(N_3)_2$

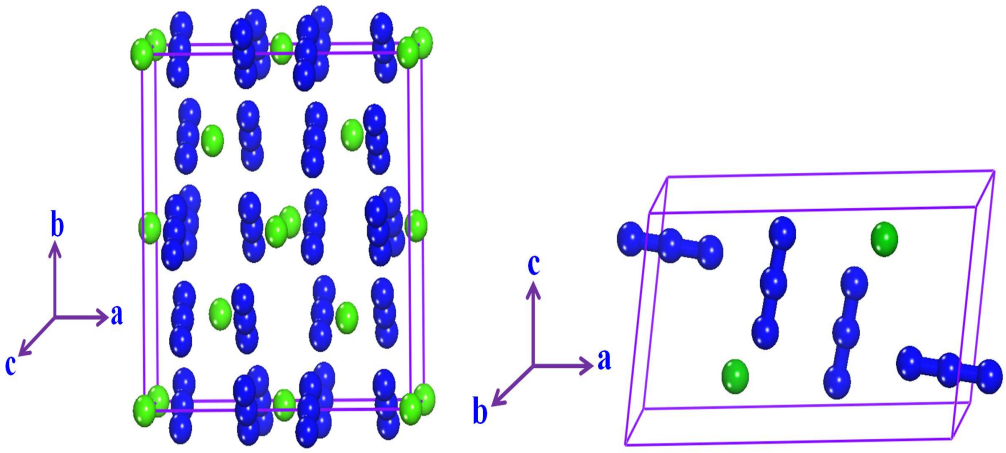

FIGURE 4.1: Crystal structure of $MN(_3)_2$ where M= Ca or Sr (a) and $BaN(_3)_2$ (b). In figure, green ball indicates, metal atom and blue ball indicates nitrogen atom, respectively.

and are fitted to the Murnaghan's equation of state and the corresponding values are presented Table 1.

TABLE 4.1: Ground state properties of $Ca(N_3)_2$, $Sr(N_3)_2$ and $Ba(N_3)_2$ calculated using various exchange-correlation functionals.

XC functional	a (Å)	b (Å)	c (Å)	β^0	V (Å^3)
$Ca(N_3)_2$					
PBE	11.5370	11.1479	6.0283		775.33
PBE+G06	11.2298	11.0735	6.0024		746.44
Expt [32]	11.620	10.920	5.660		718.20
$Sr(N_3)_2$					
PBE	12.2828	11.7055	6.2287		895.54
PBE+G06	11.8421	11.6504	6.1908		854.13
Expt [32]	11.820	11.470	6.080		824.98
$Ba(N_3)_2$					
PBE	9.8706	4.4437	5.5541	99.1497	240.52
Expt [33]	9.590	4.390	5.420	99.75	224.88
		B_0			B_0'
$Ca(N_3)_2$		48.9			3.217
$Sr(N_3)_2$		39.6			3.231
$Ba(N_3)_2$		30.6			4.698

4.3.2 Elastic properties

In order to understand the mechanical stability of the metal azides the single crystal elastic constants are calculated. Due to the orthorhombic crystal structure, both calcium and strontium azides have nine independent elastic constants while barium azide possess thirteen elastic constnats because of monoclinic symmetry. The computed elastic constants are presented in Table 4.2. Clearly, the elastic constants follow the elastic constants follow the Born-Huang mechanical stability criteria for orthorhombic and monoclinic systems [34] implying that the metal azides are mechanically stable systems. To the best of our knowledge there are no experimental or theoretical works available on the elastic constants of alkaline-earth metal azides to compare the present values.

In general, the elastic constants, C_{11}, C_{22} and C_{33} denote the elastic properties along the a, b and c-axes respectively. For the case of alkaline-earth metal azides the calculated elastic constants follows the order $C_{11} < C_{22} < C_{33}$ for orthorhombic $Ca(N_3)_2$ and $Sr(N_3)_2$ whereas $C_{33} > C_{11} > C_{22}$ for monoclinic $Ba(N_3)_2$. This merely tells the fact that the orthorhombic crystalline azides are relatively weaker along the a-axis and monoclinic $Ba(N_3)_2$ is weaker along b-axis. Therefore the orthorhombic lattices are more compressible along a-axis and b-axis is more compressible in monoclinic $Ba(N_3)_2$. This result is in good agreement with the experimental fact that monoclinic $Ba(N_3)_2$ is more compressible is along b-axis.

The knowledge of single crystalline elastic constants allow us to calculate the poly-crystalline mechanical properties through Voigt-Reuss-Hill approach [35]. The calculated properties are tabulated in Table 4.3. The bulk modulus represents the resistance to volume change against the external forces. The calculated elastic moduli are large for $Ca(N_3)_2$ than the other alkaline-earth metal azides. The calculated moduli follows the order $Ca(N_3)_2 > Sr(N_3)_2 > Ba(N_3)_2$ implying that calcium azides is the stiffer material among the alkaline-earth metal azides. In the case of alkali metal azides, we have correlated the elastic properties to the decomposition of the azides through the calculated elastic properties in chapter 3. In the present case, the calculated elastic moduli and elastic constants of $Ca(N_3)_2$ are larger than the other metal azide and they follow the order $Ca(N_3)_2 > Sr(N_3)_2$

TABLE 4.2: Single crystal elastic constants (C_{ij}, in GPa) of $Ca(N_3)_2$, $Sr(N_3)_2$ and $Ba(N_3)_2$ calculated within PBE and PBE+G06 functionals

Compd	PBE	PBE+G06
$Ca(N_3)_2$	C_{11}=56.8, C_{22}=83.4, C_{33}=108.9, C_{44}=33.9, C_{55}=15.9, C_{66}=16.1, C_{12}=22.3, C_{13}=22.1, C_{23}=51.2	C_{11}=56.7, C_{22}= 106.5, C_{33}=100.5, C_{44}=63.4, C_{55}=11.6, C_{66}=18.1, C_{12}=26.8, C_{13}=13.5, C_{23}=68.8
$Sr(N_3)_2$	C_{11}=24.4, C_{22}=59.1, C_{33}=74.7, C_{44}=26.4, C_{55}=7.9, C_{66}=11.8, C_{12}=18.6, C_{13}=15.4, C_{23}=37.9	C_{11}=43.1, C_{22}= 89.1, C_{33}=79.7, C_{44}=44.8, C_{55}=8.9, C_{66}=14.6, C_{12}=34.4, C_{13}=21.1, C_{23}=55.8
$Ba(N_3)_2$	C_{11}=48.4, C_{22}=44.2, C_{33}=67.9, C_{44}=14.4, C_{55}=10.3, C_{66}=8.6, C_{12}=22.4, C_{13}=15.6, C_{15}=1.4, C_{23}=25.3, C_{25}=0.4, C_{35}=-1.9, C_{46}=0.3	

TABLE 4.3: Polycrystalline elastic moduli (in GPa) of $Ca(N_3)_2$, $Sr(N_3)_2$ and $Ba(N_3)_2$ calculated within PBE and PBE+G06 functionals

Method	Compd	B_V	B_R	B_H	G_V	G_R	G_H	E
PBE	$Ca(N_3)_2$	48.9	42.6	45.8	23.4	20.8	22.1	57.1
	$Sr(N_3)_2$	33.6	23.1	28.4	14.9	11.6	13.3	34.5
	$Ba(N_3)_2$	31.9	31.2	31.6	13.1	11.7	12.4	32.8
PBE+G06	$Ca(N_3)_2$	53.5	42.4	47.9	28.9	19.6	24.3	62.3
	$Sr(N_3)_2$	48.3	36.8	42.6	20.4	14.4	17.4	45.9

$>$ $Ba(N_3)_2$. Therefore, $Ba(N_3)_2$ would be more sensitive to mechanical shock over the other alkaline-earth metal azides.

4.3.3 Electronic properties

Electronic band structure of metal azides is important as it gives the important information regarding the electronic process that are responsible for decomposition. The electronic band structure of alkaline-earth metal azides calculated within PBE+G06 functional for $Ca(N_3)_2$, $Sr(N_3)_2$ and with PBE functional for $Ba(N_3)_2$ are shown in Figure 4.2. The calculated band structure of alkaline-earth metal

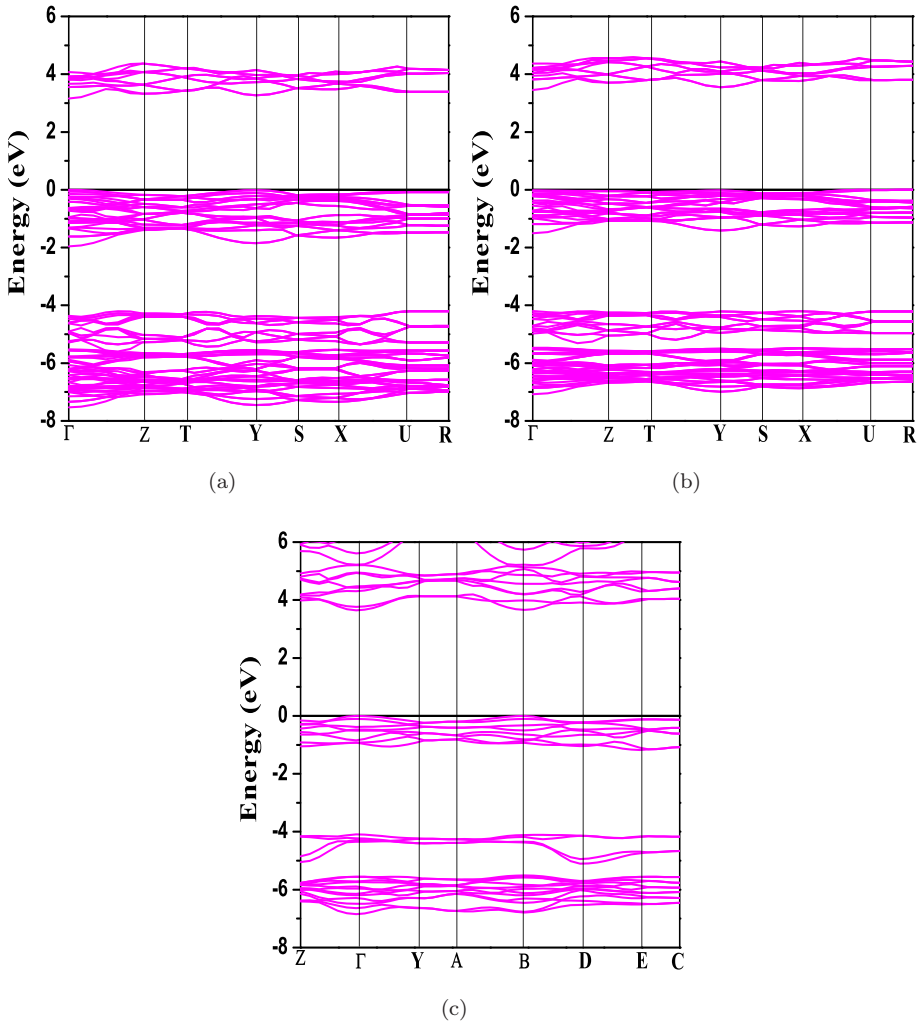

FIGURE 4.2: Electronic band structure of $Ca(N_3)_2$ (a) $Sr(N_3)_2$ (b) calculated at theoretical equilibrium volume within PBE+G06 functional and (c) $Ba(N_3)_2$ with PBE functional.

azides, $Ca(N_3)_2$, $Sr(N_3)_2$ and $Ba(N_3)_2$ clearly show that the top of the valence band and the bottom of the conduction band occurs at Γ-point in the Brillouin zone indicating that the materials are direct band gap materials with a separation of 3.16 eV for $Ca(N_3)_2$, 3.44 eV for $Sr(N_3)_2$ and 3.64 eV for $Ba(N_3)_2$ respectively.

This implies that these materials are insulators similar to alkali metal azides with considerable gaps. The calculated band gaps with other functionals such as EV [36] and TB-mBJ are listed in Table 4.4. The calculated band gap values within PBE and PBE+G06 functionals are in good agreement with earlier theoretical reports on $Sr(N_3)_2$ and $Ba(N_3)_2$ with PW91 functional.

TABLE 4.4: The band gap of $Ca(N_3)_2$, $Sr(N_3)_2$ and $Ba(N_3)_2$ calculated using various functionals

Method	$Ca(N_3)_2$	$Sr(N_3)_2$	$Ba(N_3)_2$
PBE	3.16	3.43	3.64
PBE+G06	3.16	3.44	–
EV-GGA	4.08	4.21	4.21
TB-mBJ	5.26	5.41	4.86

The states that are contributing to each energy level in the electronic band spectrum can be known by the total and partial density of states (DOS). The calculated total and partial DOS of $Ca(N_3)_2$, $Sr(N_3)_2$ and $Ba(N_3)_2$ are shown in Figure 4.3 (a), 4.3 (b) and 4.3 (c) respectively. The peaks that are present at the Fermi level are due to the end Nitrogen '*p*'-states while there are no metal atom states are present in the valence band region. This implies that the metal atoms are act as electron donors and nitrogen atoms act as electron acceptors. The states of mid nitrogen atom are situated at eV to eV. This indicates that there is a strong hybridization of states from end and mid nitrogen atoms this is a clear indication that the nitrogen atoms in azide ion are strongly covalent. The conduction band is fully dominated by the '*s*'-states of metal atom. These features clearly implies that the alkaline-earth metal azides are ionic materials.

4.3.4 Optical properties

According to experiments, $Ba(N_3)_2$ and $Sr(N_3)_2$ undergo photochemical decomposition into metal atom and nitrogen. This implies that the metal azides are photo sensitive. The photochemical decomposition can be understood by the optical transitions from the valence band to conduction band. The imaginary part of dielectric function $\epsilon(\omega)$ of the alkaline-earth metal azides is calculated and shown in Figure 4.4 (a), 4.4 (b) and 4.4 (c) respectively. The main peak in $\epsilon_2(\omega)$ is occur at 8.55eV for $Ca(N_3)_2$, 7.977eV for $Sr(N_3)_2$ and at 6.682eV for $Ba(N_3)_2$ along the three directions. The origin of this peak is due to the interband transitions from end N-'*p*' states of valence band to '*s*'-states of metal atom in the conduction band.

The reflectance experiments on $Sr(N_3)_2$ and $Ba(N_3)_2$ proved that the optical absorption starts at $1800\mathring{A}$ and $2600\mathring{A}$ respectively. The present theoretical study on the optical absorption of the metal azides as shown in Figure 4.4 (a), 4.4 (b) and

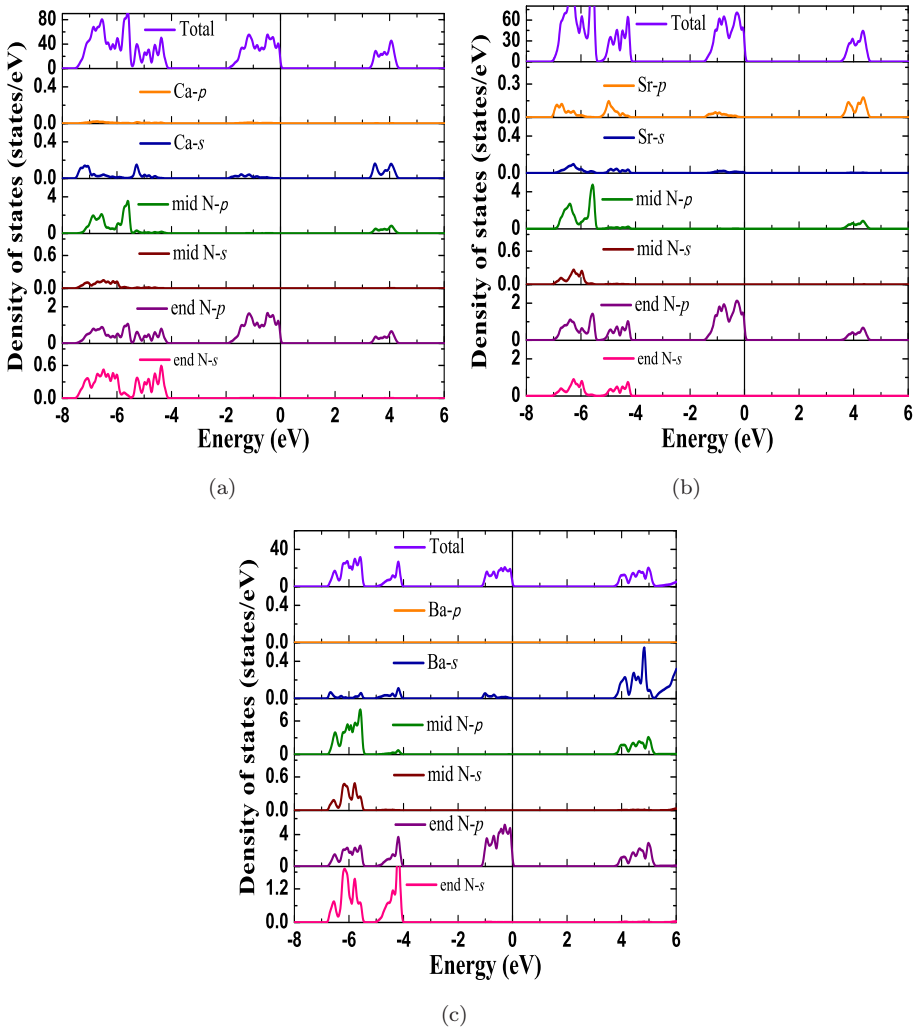

FIGURE 4.3: Total and partial density of states of $Ca(N_3)_2$ (a) $Sr(N_3)_2$ (b) calculated at theoretical equilibrium volume within PBE+G06 functional and (c) $Ba(N_3)_2$ with PBE functional.

4.4 (c) confirms that the optical absorption of $Ca(N_3)_2$ starts at 2354$\mathring{A}$, 2291$\mathring{A}$ and 2550$\mathring{A}$ for $Sr(N_3)_2$ and $Ba(N_3)_2$ respectively. The refractive index calculated as function of photon energy are shown in Figure 4.5 (a), 4.5 (b) and 4.5 (c) respectively for the azides $Ca(N_3)_2$, $Sr(N_3)_2$ and $Ba(N_3)_2$. Clearly these materials have optical anisotropy due to the fact the $n(\omega)$ is different in the three crystallographic directions. The calculated absorption coefficient of the three metal azides as shown in Figure 4.6 (a), 4.6 (b) and 4.6 (c) are larger of the order of $10^7 m^{-1}$ indicates that the compounds are photosensitive particularly to ultra-violet light. Photoconductivity is due to the increase in number of free carriers when photons are absorbed. The calculated photoconductivity as shown in Figure 4.7 (a), 4.7 (b)

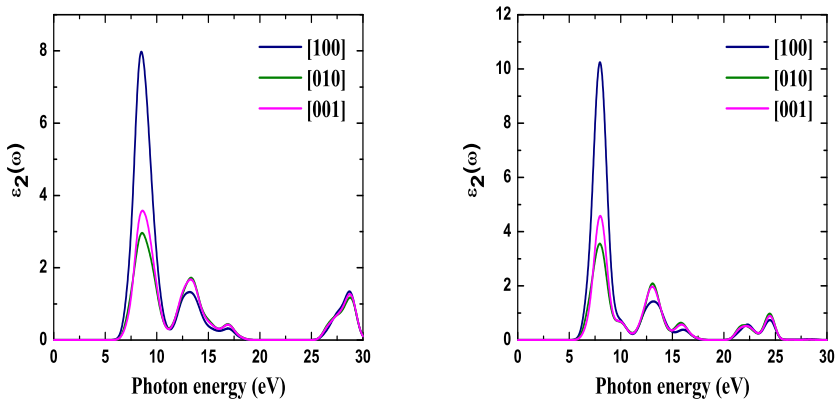

(a)

(b)

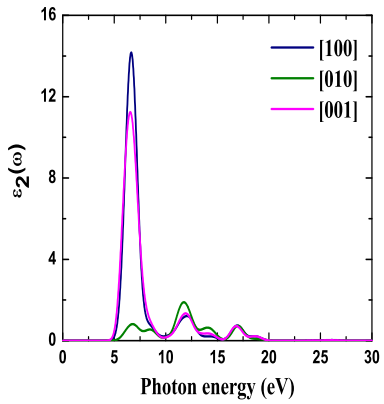

(c)

FIGURE 4.4: Imaginary part of the complex-di electric function of (a) $Ca(N_3)_2$ (b) $Sr(N_3)_2$ and (c) $Ba(N_3)_2$ calculated by using scissor operator of 2.10 eV for $Ca(N_3)_2$, 1.96 eV for $Sr(N_3)_2$ and 1.21 eV for $Ba(N_3)_2$ within PBE+G06 and PBE functional for $Ca(N_3)_2$, $Sr(N_3)_2$ and $Ba(N_3)_2$ respectively.

and 4.7 (c) the shows that all the three azides have broad photo current response in the fundamental absorption region ranging from 5 eV to 30 eV.

4.4 Conclusions

In conclusion, we have studied the structural, electronic, optical, elastic and vibrational properties of energetic molecular crystals namely alkaline-earth metal

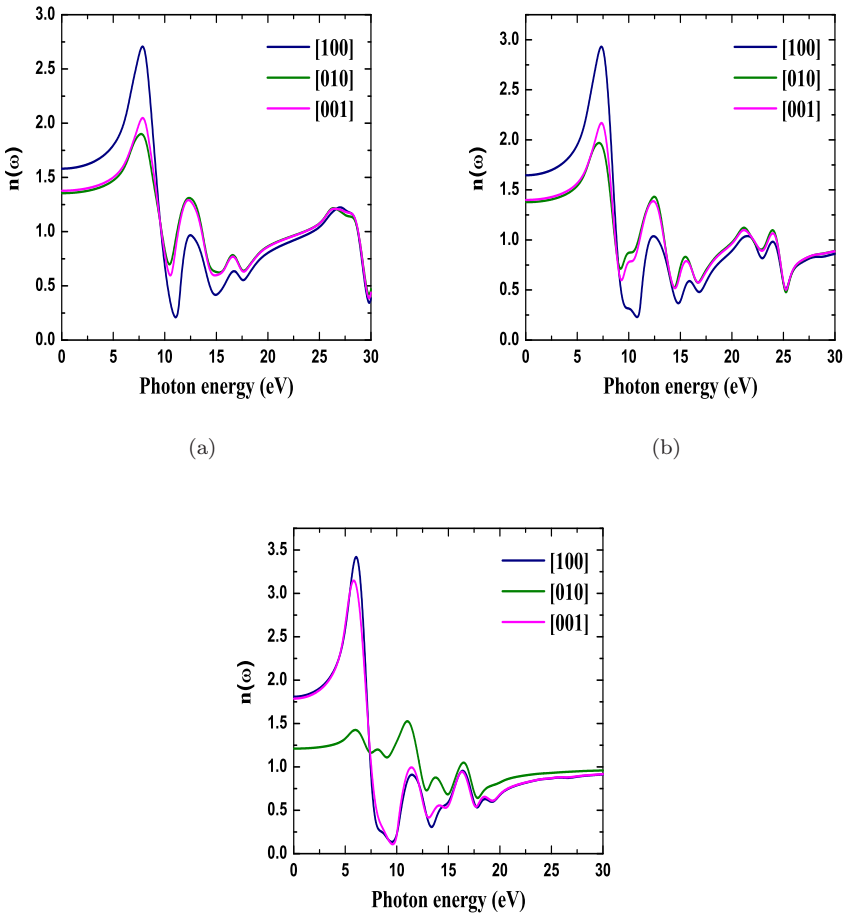

FIGURE 4.5: Refractive index of (a) $Ca(N_3)_2$ (b) $Sr(N_3)_2$ and (c) $Ba(N_3)_2$ calculated by using scissor operator of 2.10 eV for $Ca(N_3)_2$, 1.96 eV for $Sr(N_3)_2$ and 1.21 eV for $Ba(N_3)_2$ within PBE+G06 and PBE functional for $Ca(N_3)_2$, $Sr(N_3)_2$ and $Ba(N_3)_2$ respectively.

azides $Ca(N_3)_2$, $Sr(N_3)_2$ and $Ba(N_3)_2$. We have focussed our attention more towards the effect of van der Waals interactions on the structural properties, elastic stiffness tensor and vibrational frequencies of the metal azides. We find that all properties are improved to a great extent by the inclusion of vdW interactions in the calculations. In particular, PBE+G06 functional gives good results compared to other dispersion corrected functionals. The calculated elastic constants suggest that the metal azides are mechanically stable systems under normal conditions. The elastic constants of $Ca(N_3)_2$, are larger in magnitude than the rest of alkali metal azides, implying that lithium azide is mechanically stiffest material among

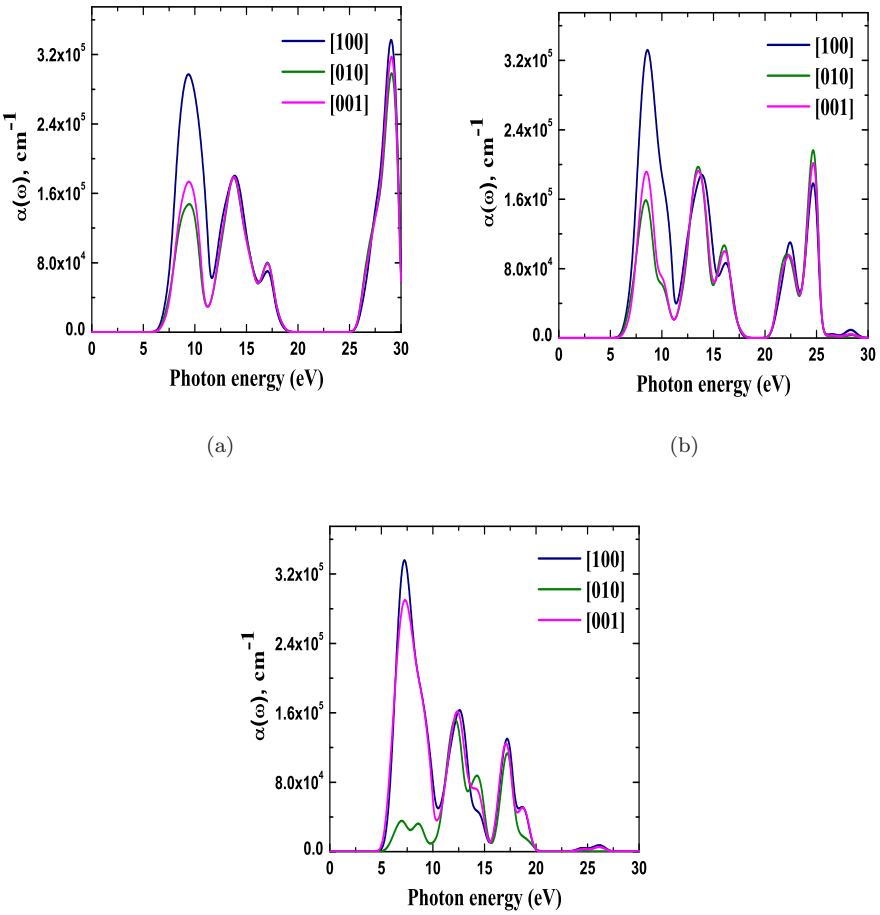

(a) (b)

(c)

FIGURE 4.6: Absorption of (a) $Ca(N_3)_2$ (b) $Sr(N_3)_2$ and (c) $Ba(N_3)_2$ calculated by using scissor operator of 2.10 eV for $Ca(N_3)_2$, 1.96 eV for $Sr(N_3)_2$ and 1.21 eV for $Ba(N_3)_2$ within PBE+G06 and PBE functional for $Ca(N_3)_2$, $Sr(N_3)_2$ and $Ba(N_3)_2$ respectively.

the alkali metal azides. This fact is also confirmed by the higher values of bulk modulus, shear modulus and Young's modulus of $Ca(N_3)_2$. Overall from the study of elastic constants we can come to a conclusion that $Ba(N_3)_2$ is more sensitive towards a mechanical shock as the compound has lower elastic moduli. The absorption spectra and photo conductivity spectra have been calculated and found that the absorption peaks are in the ultra-violet energy region. Therefore we conclude that the decomposition of alkali metal azides is more favorable by the action of light (ultra violet).

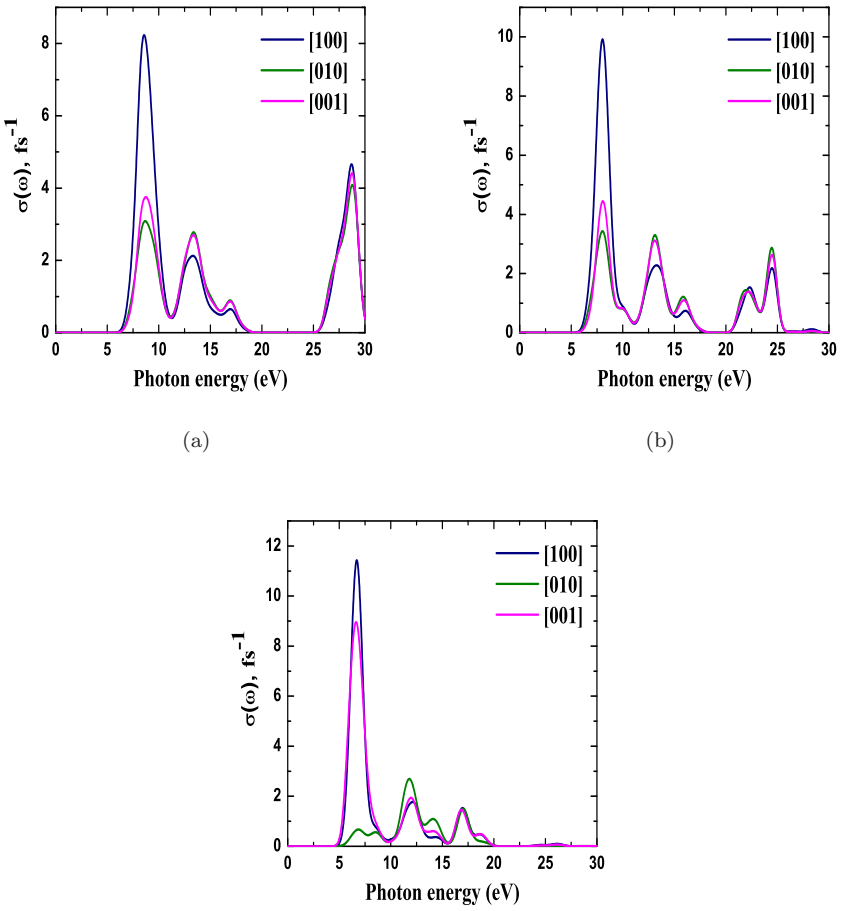

FIGURE 4.7: Photoconductivity of (a) $Ca(N_3)_2$ (b) $Sr(N_3)_2$ and (c) $Ba(N_3)_2$ calculated by using scissor operator of 2.10 eV for $Ca(N_3)_2$, 1.96 eV for $Sr(N_3)_2$ and 1.21 eV for $Ba(N_3)_2$ within PBE+G06 and PBE functional for $Ca(N_3)_2$, $Sr(N_3)_2$ and $Ba(N_3)_2$ respectively.

References

[1] H. D. Fair, and R. F. Walker, Energetic Materilas, vol 1, 1977, Plenum Press, New York.

[2] F. P. Bowden, A. D. Yoffe, Fast Reactions in Solids, Butterworth Scientific Publications, 1958, London, UK.

[3] B. L. Evans, A. D. Yoffe, P. Gray, Chem. Rev. 59 (1959) 515.

[4] M. I. Eremets, M. Yu. Popov, I. A. Trojan, V. N. Denisov, R. Boehler, R. J. Hemley, J. Chem. Phys. 120 (2004) 10618.

[5] S. A. Medvedev, I. A. Trojan, M.I. Eremets, T. Palasyuk, T.M. Klapotke, J. Evers, J. Phys.: Condens. Matt. 21 (2009) 195404.

[6] Cheng Ji, Fuxiang Zhang , Dongbin Hou, Hongyang Zhu, Jianzhe Wu, Ming-ChienChyu, Valery I.Levitas, YanzhangMaa, J. Phys. Chem. Solids, 72 (2011) 736.

[7] S. A. Medvedev, T. Palasyuk, I. A. Trojan, J. Evers, T. M. Klapötke and M. I. Eremets, Private communications (2011).

[8] D. Hou, F. Zhang, C. Li, T. Hannon, H. Zhu, J. Wu, V. Levitas, Y. Ma, J. App. Phys. 110 (2011) 023524.

[9] D. Hou, F. Zhang, C. Li, T. Hannon, H. Zhu, J. Wu, Y. Ma, Phys. Rev. B 84 (2011) 064127.

[10] C. Li, R. Zhang, D. Hou, H. Zhu, J. Wu, M. Chyu, Y. Ma, J. App. Phys. 111 (2012) 112613.

[11] H. Zhu, F. Zhang, C. Ji, D. Hou, J. Wu, T. Hannon, and Y. Ma, J. App. Phys. 113 (2013) 033511.

[12] M. Zhang, H. Yan, Q. Wei, H. Wang, Z. Wu, Euro. Phys. Lett. 101 (2013) 26004.

[13] X. Wu, H. Cui, J. Zhang, R. Cong, H. Zhu, Q. Cui, App. Phys. Lett. 102 (2013) 121902.

[14] M. Zhang, K. Yin, X. Zhang, H. Wang, Q. Li, Z. Wu, Solid State Comm. 161 (2013) 13.

[15] K. Ramesh Babu, Ch. Bheema Lingam, Surya P. Tewari, G. Vaitheeswaran, J. Phys. Chem. A 115 (2011) 4521.

[16] K. Ramesh Babu, G. Vaitheeswaran, Chem. Phys. Lett. 533 (2012) 35.

[17] G. Vaitheeswaran, K. Ramesh Babu, J. Chem. Sci 124 (2012) 1391.

[18] W. Zhu, X. Xu, H. Xiao, J. Phys. Chem. Solids 68 (2007) 1762.

[19] M. C. Payne, M. P. Teter, D. C. Allan, T. A. Arias, J. D. Joannopoulos, Rev. Mod. Phys. 64 (1992) 1045.

[20] M. Segall, P. Lindan, M. Probert, C. Pickard, P. Hasnip, S. Clark, M. J. Payne, J. Phys:. Cond. Matt. 14 (2002) 2717.

[21] D. Vanderbilt, Phys. Rev. B. 41 (1990) 7892.

[22] G. Kresse, J. Furthmuller, Phys. Rev. B. 54 (1996) 11169.

[23] T. H. Fischer, J. Almolf, J. Phys. Chem. 96 (1992) 9768.

[24] D. M. Ceperley, B. J. Alder, Phys. Rev. Lett. 45(1980) 566.

[25] J. P. Perdew, A. Zunger, Phys. Rev. B. 23 (1981) 5048.

[26] J. P. Perdew, K. Burke, M. Ernzerhof, Phys. Rev. lett. 77 (1996) 3865.

[27] H. J. Monkhorst, J. Pack, Phys. Rev. B. 13 (1976) 5188.

[28] S. Grimme, J. Comp. Chem. 27 (2006) 1787.

[29] F. Tran and P. Blaha, Phys. Rev. Lett. 102 (2009) 226401.

[30] D. J. Singh and L. Nordstrom, Planewaves, Pseudopotentials, and the LAPW Method, 2nd ed. (Springer Verlag, Berlin, 2006).

[31] P. Blaha, K. Schwarz, G. Madsen, D. Kvasnicka, and J. Luitz, WIEN2k, An Augmented Plane Wave + Local Orbitals Program for Calculating Crystal Properties (K. Schwarz, Tech. Univ. Wien, Austria, 2001).

[32] G. E. Pringle, D. E. Noakes, Acta. Crystallogr. B 24 (1968) 262.

[33] C. S. Choi, Acta. Crystallogr. B 25 (1969) 2638.

[34] M. Born and K. Huang, Dynamical Theory of Crystal Lattices (Oxford: Oxford University Press)(1998).

[35] R. Hill, Proc. Phys. Soc. Lond. A 65 (1952) 349.

[36] E. Engel, S.H. Vosko, Phys. Rev. B 47 (1993) 13164.

Chapter 5

Alkali Metal Amides

Abstract

We report first principles calculations on the electronic structure, elastic and optical properties of nitrogen based solid hydrogen storage materials $LiNH_2$, $NaNH_2$, KNH_2, and $RbNH_2$. The calculated ground state properties are in good agreement with experiment. Our calculations predict that among the metal amides, $LiNH_2$ is found to be stiffer material. The calculated elastic constants show that all the compounds are mechanically stable. The hydrogen decomposition temperatures are calculated and follows the order $RbNH_2 < KNH_2 < NaNH_2 < LiNH_2$. The electronic band structure reveals that all the compounds are semiconductors with a considerable band gap. The $[NH_2]^-$ derived states are completely dominating the entire valence band region while the metal atom states occupy the conduction band. The optical properties are calculated and analyzed through the band structure. The calculated band structure is used to analyze the different interband optical transitions occur between valence and conduction bands. Our calculations show that these materials have considerable optical anisotropy.

5.1 Introduction

Hydrogen, being most abundant element in the universe, considered to be the best choice as future energy source. The superior qualities of hydrogen such as light weight, high energy per unit mass and eco-friendly combustion products made it as a suitable replacement for current carbon based energy resources. Indeed, hydrogen fuel is believed to meet various applications such as fuel for automobiles and space jets, cooking gas, and also in production of electricity. However storage of hydrogen is a difficult problem. To store hydrogen as a compressed gas, high pressure tanks are required and the storage in liquid state needs insulated cryogenic tanks. Both these are not suitable for practical applications as storage in gaseous state leads to low energy density while safety and cost are major concerns for the storage in liquid state. Therefore solid state hydrogen storage is the only choice to look at the issue and which requires search for solid materials that can store hydrogen with volumetric densities greater than those of other states hydrogen storage [1–5].

Hydrides of light and heavy metals exhibit qualitative solid-state hydrogen storage properties such as high volumetric densities and low pressure desorptions. But, the slow absorption and desorption kinetics limits their practical use. On the other hand, complex hydrides consisting of light metal elements have been noticed as materials with fast hydrogen kinetics and most importantly they can store hydrogen in greater percentages over simple metal hydrides. Complex metal hydrides with potential solid state hydrogen storage applications are classified as alanates, borohydrides, and amides [3]. Among the complex metal hydrides, nitrogen based materials namely amides received much interest because of their high hydrogen storage capacity and low operating temperatures [5]. Most importantly, alkali metal amides gain lots of interest because of their potential reversible hydrogen storage applications [6].

The first report on alkali metal amides KNH_2 and $NaNH_2$ was appeared in the year 1809 by the authors Gay Lussac and Thenard [7]. Later in 1894, Titherley reported the synthesis of $LiNH_2$ [8]. These metal amides were traditionally used as reagents in organic synthesis [9, 10]. However, it is only in the year 2002, Chen

et al. discovered $LiNH_2$ as a potential candidate for reversible hydrogen storage applications and hence paved new insights into the hydrogen storage application of these materials [6]. In general for any solid state hydrogen storage system, the important characteristics are the following: the material should have high hydrogen gravimetric densities, fast hydriding and dehydriding characteristics, and suitable thermodynamic properties. It is a well known fundamental aspect that the hydrogen absorption and desorption properties can be well judged through the knowledge of electronic structure and bonding. Moreover, the fundamental physical properties such as the elastic and optical properties are much important to understand the mechanical stability and optical response of solid state hydrogen storage materials. In addition, these properties are necessary in determining the thermodynamic properties such as hydrogen releasing temperature (decomposition temperature) and Debye temperature [11].

Theoretical calculations based on density functional theory are accurate enough in predicting and reproducing the experimentally measured quantities. The electronic structure of $LiNH_2$ was reported by using first principles calculations and found that the material has non-metallic nature [12, 13]. Recently, the electronic structure of $LiNH_2$ was determined through XAS studies and the results are found to be compliment to the earlier theoretical reports [14]. Elastic constants of $LiNH_2$ were reported theoretically by using the density functional theory calculations [15]. The high pressure behaviour of $LiNH_2$ was reported by using the Raman spectroscopy technique and found that the system undergo a phase transition from ambient tetragonal α-$LiNH_2$ structure to high pressure β-$LiNH_2$ phase [16]. Theoretically the pressure-induced structural phase transitions of $LiNH_2$ was reported by using the ab-initio total energy calculations and evolutionary structure prediction simulations [17, 18]. By using combined synchrotron X-ray diffraction measurements and ab initio density functionals, the pressure-induced phase transition with large volume collapse (11%) in $LiNH_2$ was reported [19]. The high pressure behaviour of $NaNH_2$ was reported by using Raman and Infrared spectroscopies [20]. and also through evolutionary structure simulations [21]. To the best of our knowledge, there are no comparative studies available to explain the structural, electronic structure, bonding, elastic and optical properties of the alkali metal

amides $LiNH_2$, $NaNH_2$, KNH_2 and $RbNH_2$. Hence, in this present chapter we aim to study these properties by performing density functional theory calculations.

5.2 Computational details

The density functional calculations are carried out with the plane wave pseudopotential method [22] Vanderbilt type ultrasoft pseudopotentials used for the present calculations [23]. The electronic wave functions are obtained by using density mixing scheme and the structures are relaxed using the Broyden, Fletcher, Goldfarb, and Shannon (BFGS) method. The local density approximation with Ceperley-Alder [24] exchange-correlation potential parameterized by Perdew and Zunger [25] and also generalized gradient approximation proposed by Perdew-Burke-Ernzerhof [26] have been used to describe the exchange-correlation potential. The pseudo atomic calculations were performed for Li $2s^1$, Na $2s^2$ $2p^6$ $3s^1$, K $3s^2$ $3p^6$ $4s^1$, Rb $4s^2$ $4p^6$ $5s^1$, N $2s^2$ $2p^3$ and H $1s^1$, respectively. The cut-off energy for plane waves was set to 380 eV for $LiNH_2$, 400 eV for $NaNH_2$ and 320 eV for KNH_2, $RbNH_2$, respectively. Brillouin zone sampling was performed by using the Monkhorst-Pack scheme [27] with a k-point grid of 4x4x2 for $LiNH_2$, 4x3x4 for $NaNH_2$ and 4x4x4 for KNH_2, $RbNH_2$, respectively. The values of both plane wave cut-off energy and k-point grid were determined by performing total energy calculations to achieve the convergence of 1 meV. To treat the van der Waals interactions we have used the Grimme functional (PBE+G06) [28]. For the computation of electronic band gap, we use the recently developed Tran Blaha-modified Becke Johnson potential [29] within linearized augmented plane wave (LAPW) method as implemented in WIEN2k package [30, 31].

Starting from the optimized crystal structure all the dependent properties have been calculated. The elastic constants were calculated by using stress-strain method as implemented in CASTEP code. There are three tensile and three shear components resulting six components and thereby the elastic constants form a 6x6 symmetric matrix based on $\sigma_i = C_{ij}\epsilon_j$. All the dynamical properties have been calculated by using linear response theory.

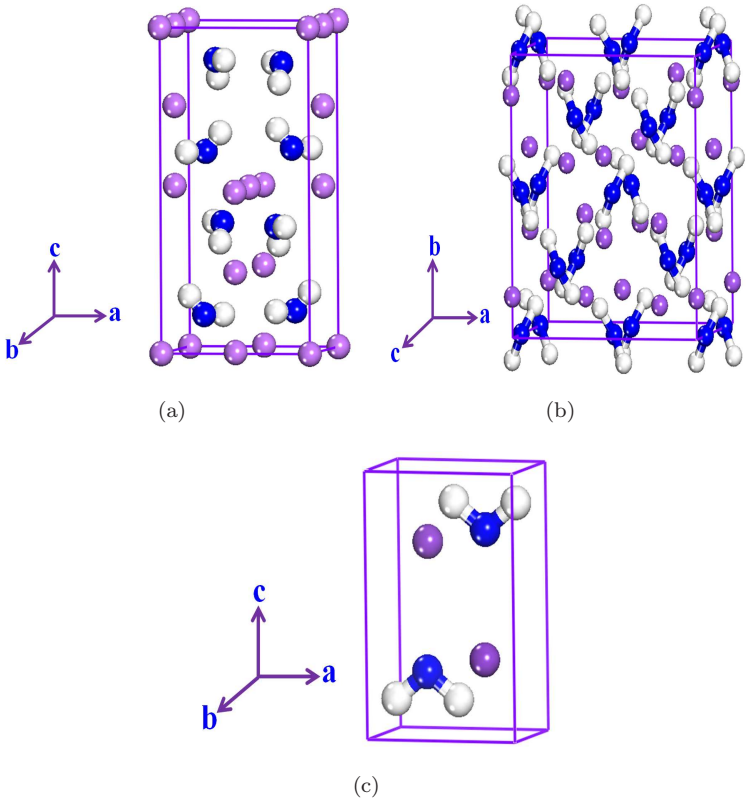

FIGURE 5.1: Crystal Structure of tetragonal $LiNH_2$ (a), orthorhombic $NaNH_2$ (b), and monoclinic KNH_2 and $RbNH_2$ (c). In figure, violet ball indicates metal atom, blue ball indicates nitrogen and white ball indicates hydrogen atom.

5.3 Results and discussion

5.3.1 Structural properties

At ambient conditions, $LiNH_2$ crystallizes in tetragonal structure with space group I-4 (82) (z=4) [32] and $NaNH_2$ crystallize in orthorhombic structure with space group Fddd (70) (z=16) [33] as shown in Figure 5.1 (a) and 5.1 (b) respectively. Whereas both KNH_2 and $RbNH_2$ crystallize in monoclinic structure with space group $P2_1/m$ (13) (z=2) [34] as shown in Figure 5.1 (c).

All the calculations were carried out by adopting the experimental crystal structures as the initial structures and they were relaxed to allow the ionic configurations, cell shape, and volume to change to predict the theoretical equilibrium crystal structure within LDA (CA-PZ) and GGA (PBE). The optimized lattice parameters are tabulated in Table 5.1 and Table 5.2 along with experiment. It can

TABLE 5.1: Structural properties of alkali metal amides calculated within LDA (CA-PZ), GGA (PBE) and GGA (PBE+G06).

	a (Å)	b (Å)	c (Å)	β (deg)	ρ (g/cc)	V (Å^3)
$LiNH_2$						
LDA (CA-PZ)	4.7689	–	10.0503	–	1.33	228.56
GGA (PBE)	5.1819	–	10.5111	–	1.081	282.25
GGA (PBE+G06)	5.0025	–	10.156	–	1.200	254.17
Expt [32]	5.037	–	10.278	–	1.169	260.76
$NaNH_2$						
LDA (CA-PZ)	8.8645	9.8277	7.4388	–	1.591	648.06
GGA (PBE)	8.9206	10.7291	8.4506	–	1.280	808.82
GGA (PBE+G06)	9.1038	9.5755	7.5898	–	1.56	661.63
Expt [33]	8.949	10.456	8.061	–	1.37	754.27
KNH_2						
LDA (CA-PZ)	4.3179	3.5767	5.9105	95.1	2.013	90.92
GGA (PBE)	4.668	3.8052	6.2872	96.3	1.649	110.99
GGA (PBE+G06)	4.5402	3.6664	6.0174	96.1	1.838	99.60
Expt [34]	4.586	3.904	6.223	95.8	1.6515	110.84
$RbNH_2$						
LDA (CA-PZ)	4.5898	3.7752	6.1700	96.7	3.174	106.17
GGA (PBE)	4.9112	4.042	6.5738	97.2	2.6029	129.49
GGA (PBE+G06)	4.7657	3.8123	6.2679	97.6	2.9857	112.89
Expt [34]	4.850	4.148	6.402	97.8	2.641	127.60

be seen that the calculated GGA values are in good agreement with experiment when compared to LDA results. We find that the dispersion interactions do not play prominent role in these systems as the volume computed with PBE+G06 functional results in large errors compared to PBE volume, except for the case of $LiNH_2$. Therefore, to calculate the elastic constants, electronic, bonding, and optical properties we adopted the GGA functional.

5.3.2 Elastic properties

Elastic properties of solid materials are important as they relate to various fundamental properties such as interatomic potentials, equation of state, and phonon spectra. Moreover, it was noticed that there is a correlation between the elastic constants and the melting temperatures of a solid. Orimo et al., successfully applied the concept of the melting temperatures of MBH_4 where M = Li, Na, K under hydrogen atmosphere can be regarded as an index of hydrogen decomposition

TABLE 5.2: Atomic positions of alkali metal amides calculated within GGA (PBE) and GGA (PBE+G06).

Compd	GGA (PBE)	GGA (PBE+G06)	Expt
$LiNH_2$			
Li1	(0 0 0)	(0 0 0)	(0 0 0)
Li2	(0 0.5 0.25)	(0 0.5 0.25)	(0 0.5 0.25)
Li3	(0 0.5 0.0028)	(0 0.5 0.0026)	(0 0.5 0.0042)
N	(0.2230 0.2494 0.1134)	(0.2366 0.2529 0.1170)	(0.2284 0.2452 0.1148)
H1	(0.2286 0.1299 0.1925)	(0.2282 0.1285 0.1983)	(0.226 0.149 0.172)
H2	(0.3961 0.3484 0.1203)	(0.4287 0.3289 0.1212)	(0.308 0.359 0.114)
$NaNH_2$			
Na	(0 0.1400 0)	(0 0.1531 0)	(0 0.1452 0)
N	(0 0 0.2291)	(0 0 0.2539)	(0 0 0.2365)
H	(0.0668 0.8347 0.2291)	(0.0603 0.8045 0.3531)	(0.0635 0.9034 0.3053)
KNH_2			
K	(0.222 0.25 0.3134)	(0.2239 0.25 0.3064)	(0.228 0.25 0.295)
N	(0.2714 0.25 0.7568)	(0.276 0.25 0.7709)	(0.289 0.25 0.778)
H	(0.3054 0.04 0.8628)	(0.3079 0.0312 0.8809)	(0.29 0.04 0.88)
$RbNH_2$			
Rb	(0.2147 0.250 0.3061)	(0.219 0.25 0.3033)	(0.203 0.25 0.295)
N	(0.2758 0.25 0.7585)	(0.2835 0.25 0.7786)	(0.28 0.25 0.79)
H	(0.3137 0.0516 0.8591)	(0.3195 0.0388 0.8838)	(– – –)

temperatures [35]. So, it is valuable to get the knowledge of elastic constants of alkali metal amides MNH_2 where M is the alkali metal atom for determining their thermodynamic properties, e.g. melting temperature (Tm). The calculated elastic constants C_{ij} of MNH_2 are displayed in Table 5.3. The present computed elastic constants of $LiNH_2$ are in good comparison with those of earlier theoretical reports based on GGA calculations [15]. For the case of $NaNH_2$, KNH_2 and $RbNH_2$ there are no experimental or theoretical reports available to compare the present values. The calculated C_{ij} satisfy the Born stability criteria for tetragonal, orthorhombic and monoclinic crystals [36]. Thus, the tetragonal $LiNH_2$, orthorhombic $NaNH_2$ and monoclinic KNH_2 and $RbNH_2$ are mechanically stable systems.

For complex hydrides, the elastic constants C_{11}, C_{22}, and C_{33} are important as they relate the deformation behavior and atomic bonding characteristics. For all the compounds we find that the elastic constants follow the order $C_{11} > C_{22} > C_{33}$ while it is $C_{11} = C_{22} > C_{33}$ for $LiNH_2$. This clearly indicates that the atomic

TABLE 5.3: The calculated single-crystal elastic constants C_{ij} in GPa of alkali metal amides.

Compound	SCE
$LiNH_2$	C_{11} = 47.4, C_{12} = 13.3, C_{13} = 17.7
	C_{33} = 45.7, C_{44} = 14.9, C_{66} = 20.7
$NaNH_2$	C_{11} = 53.2, C_{12} = 18.3, C_{13} = 9.6, C_{22} = 20.6
	C_{23} = 2.6, C_{33} = 20.1, C_{46} = 1.6, C_{55} = 10.6,
	C_{66} = 8.9
KNH_2	C_{11} = 31.3, C_{12} = 6.5, C_{13} = 6.1, C_{15} = 0.2
	C_{22} = 30.8, C_{23} = 6.2, C_{25} = 0.6, C_{33} = 22.4
	C_{35} = -1.6, C_{44} = 7.1, C_{46} = -0.1, C_{55} = 6.6
	C_{66} = 11.5
$RbNH_2$	C_{11} = 27.1, C_{12} = 6.1, C_{13} = 7.9, C_{15} = 1.5
	C_{22} = 21.6, C_{23} = 4.4, C_{25} = 1.8, C_{33} = 19.5
	C_{35} = -1.3, C_{44} = 7.1, C_{46} = -0.4, C_{55} = 5.2
	C_{66} = 9.7

TABLE 5.4: The calculated polycrystalline elastic constants in GPa of alkali metal amides.

Compound	$LiNH_2$	$NaNH_2$	KNH_2	$RbNH_2$
B_H	26.4	14.3	13.3	11.4
G_H	16.1	6.6	9.1	7.4

bonding along the (1 0 0) plane is strongest because of the intermolecular interactions among the amide anion units and which leads to the fact that the c-axis of the lattice will be more compressible when compared to other crystallographic axes. This fact is in good agreement with the recent experimental high pressure study of $LiNH_2$ where the authors found that the c-axis is more compressible over a-axis [19]. Moreover, we find that the elastic constants of $LiNH_2$ are larger than those of other alkali metal amides which can be understood by the fact that the interatomic bonding is stronger in $LiNH_2$ than the rest of the alkali metal amides. We have calculated the melting temperature (T_d) of the amides by using the elastic constants through the formula given by Fine et al [37]. T_m = 354 + 4.5 ($2C_{11}$ + C_{33})/3. Clearly, there is a correlation between the bulk modulus B and the decomposition temperature T_m of the alkali metal amides. The trend of calculated decomposition temperature T_m of MNH_2 follows, $RbNH_2$ (T_m = 464.6 K) < KNH_2 (T_m = 481.5 K) < $NaNH_2$ (T_m = 543.8 K) < $LiNH_2$ (T_m = 564.8 K) same as that of bulk modulus B of MNH_2 as $RbNH_2$ (B_0 = 11.4 GPa) < KNH_2 (B_0 = 13.3 GPa) < $NaNH_2$ (B_0 = 14.3 GPa) < $LiNH_2$ (B_0 = 26.4 GPa).

The calculated elastic constants allow us to obtain the macroscopic mechanical properties such as bulk moduli and shear moduli via Voigt-Reuss-Hill approach [38]. The calculated poly crystalline elastic properties of MNH_2 are presented in Table 5.4. We find that the poly crystalline bulk moduli B_H of the amides are much smaller than typical metals and intermetallic compounds, which indicates all MNH_2 are highly compressible materials. Further, the bulk modulus value decreases from Li to Rb amides, implies the higher hardness for $LiNH_2$. In general the hardness of a material depends on the resistance of the material towards the shear strain. Therefore an important factor of hardness is the strength of the interatomic bonds with respect to the shear deformation, which influences the mobility of dislocations in the solids. In the present case, the shear modulus of the metal amides increases in the following sequence $G_H(RbNH_2) < G_H(KNH_2) < G_H(NaNH_2) < G_H(LiNH_2)$. These results on the bulk moduli and shear moduli of MNH_2 follow the trend that was observed in the case of alkali borohydrides [39]. The calculated B and G are used to analyze the ductile-brittle nature of the metal amides through Pugh's criterion [40], according to which the critical value of B/G ratio that separates the ductile and brittle material is 1.75. If B/G>1.75, the material behaves in a ductile manner, otherwise the material behaves in a brittle manner. In the case of MNH_2 (A=Li, K, Rb), the B/G values are less than 1.75 indicating that these complex amides are brittle in nature. However, the B/G value of $NaNH_2$ is greater than 1.75 indicating that the material is ductile. Young's modulus (Y) provides a measure of the stiffness of the solid and if the magnitude of Y is large, then the material can be regarded as stiffer material. Among the four alkali metal amides, $LiNH_2$ is the stiffest material because of its high value of Y. However, when compared other complex hydrides such as $LiBH_4$ (Y=103.68 GPa), $LiNH_2$ has less stiffness.

5.3.3 Electronic band structure and Optical properties

The energy band structures of alkali metal amides are calculated by using PBE functional. The computed band structures are shown in Figure 5.2 (a), 5.2 (b), 5.2 (c) and 5.2 (d) respectively for $LiNH_2$, $NaNH_2$, KNH_2 and $RbNH_2$.

The overall band structure profiles are quite different from each other due to their different crystal geometries. The calculated band structure of $LiNH_2$ shows a

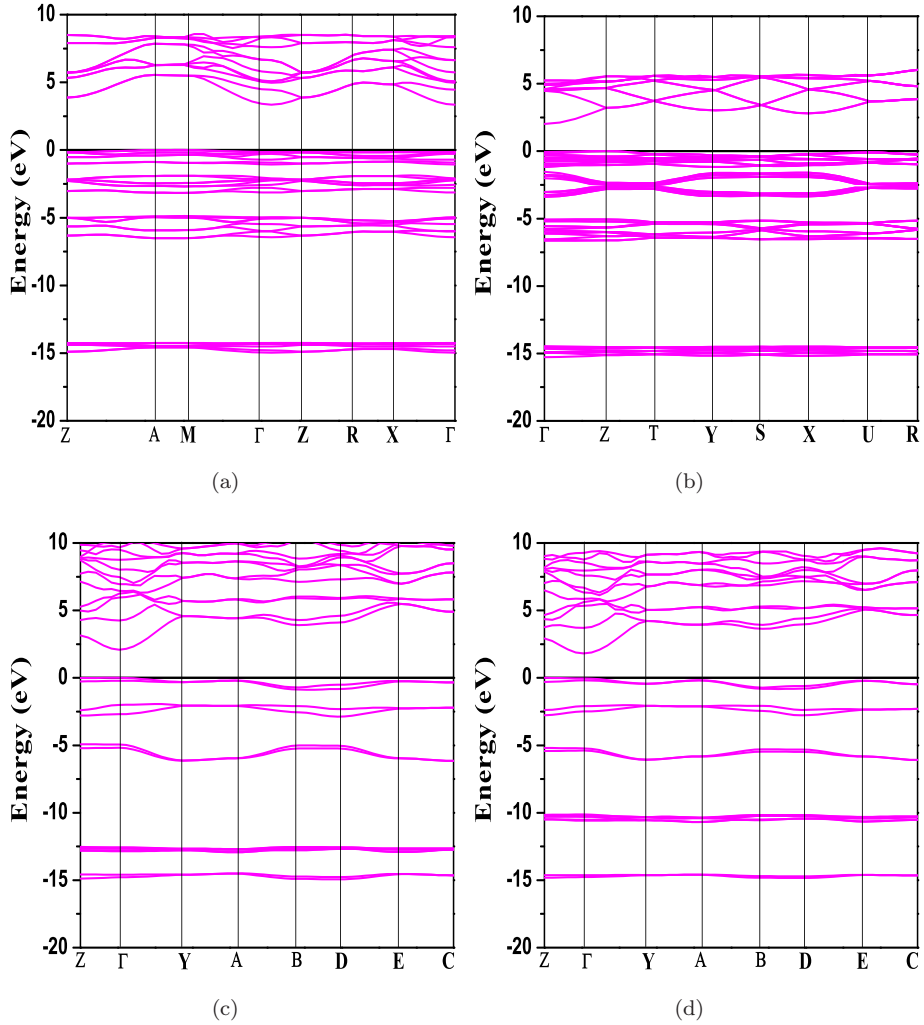

FIGURE 5.2: Electronic band structure of alkali metal amides $LiNH_2$ (a), $NaNH_2$ (b), KNH_2 (c) and $RbNH_2$ (d) calculated by using the PBE+G06 functional at theoretical equilibrium volume.

band gap of 3.34 eV with the maximum of valence band occurs at A-point and minimum of the conduction band occurs at Γ-point indicating that the compound is an indirect band gap semiconductor. The value of the band gap calculated with PBE is in good agreement with earlier theoretical reports using generalized gradient approximation (3.2 eV) [12]. In the case of orthorhombic $NaNH_2$, the calculated band structure shows a gap of 2.09 eV between Γ-Γ reveals that the material is a direct gap semiconductor. Both KNH_2 and $RbNH_2$ are also found to be indirect gap semiconductors with a gap of 2.07 eV and 1.80 eV occurs between Z and Γ respectively. However, these calculated band gaps with PBE functional are within the limitation of DFT. To achieve accurate band gaps that are in good

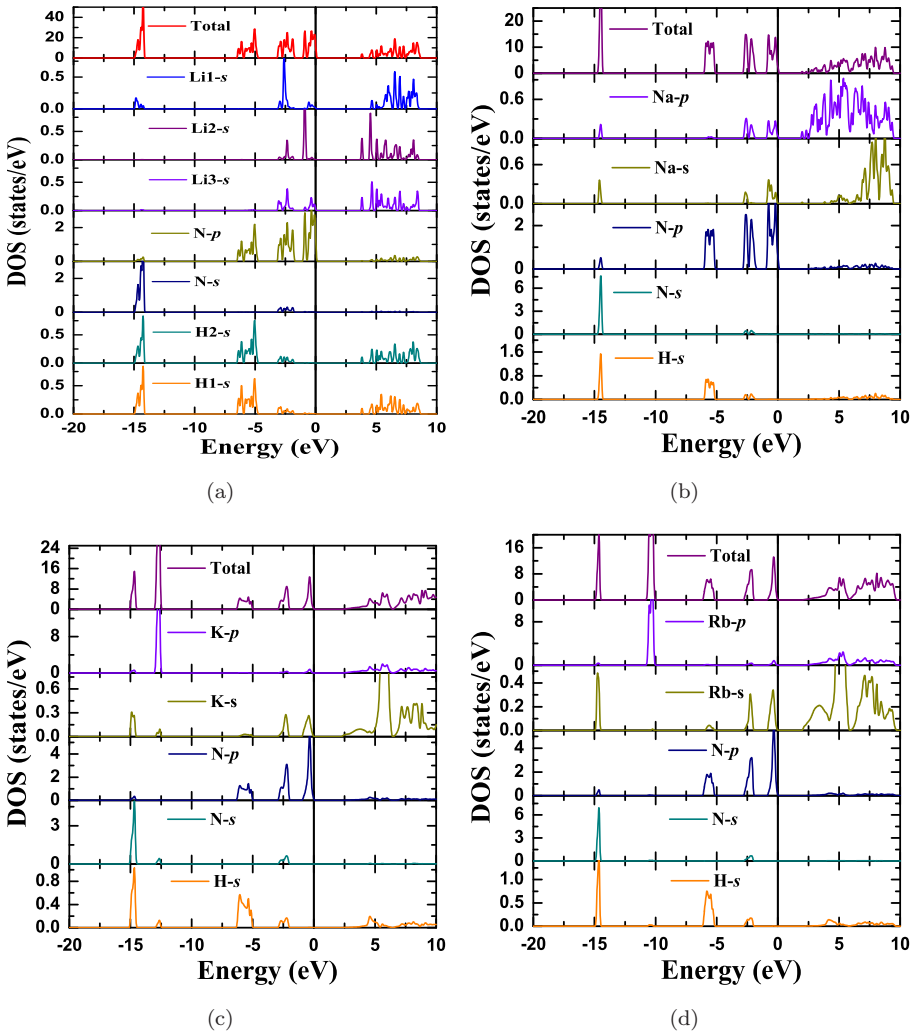

FIGURE 5.3: Total and Partial density of states of $LiNH_2$ (a), $NaNH_2$ (b), KNH_2 (c) and $RbNH_2$ (d).

accord with experiment we use TB-mBJ functional [29]. The calculated band gaps with TB-mBJ functional are 4.95 eV for $LiNH_2$, 3.55 eV for $NaNH_2$, 3.87 eV for KNH_2 and 3.60 eV for $RbNH_2$. There are no experimental data available on band gaps to compare the present results.

The total and partial density states of alkali metal amides are calculated and shown in Figure 5.3 (a), 5.3 (b), 5.3 (c) and 5.3 (d) respectively for $LiNH_2$, $NaNH_2$, KNH_2 and $RbNH_2$. It can be noticed that for all the compounds the valence band states are completely dominated by the states of $[NH_2]^-$ anion, a similar feature also observed in the other complex metal hydrides with a positive cation

TABLE 5.5: The calculated n(0), main peak of the absorption coefficient of optical absorption spectra, $\alpha(\omega)$ (in 10^5 cm^{-1}) and its corresponding energy (E) of alkali metal amides.

Compd	$LiNH_2$	$NaNH_2$	KNH_2	$RbNH_2$
$n_{[100]}(0)$	1.2590	1.3544	1.4549	1.4409
$n_{[010]}(0)$	1.2590	1.3737	1.3719	1.3440
$n_{[001]}(0)$	1.2582	1.3645	1.4124	1.3866
$\alpha_{[100]}$	13.93	16.05	12.51	10.48
$\alpha_{[010]}$	13.93	13.45	21.31	18.41
$\alpha_{[001]}$	11.46	15.51	19.39	16.48
$\alpha_{[100]}$ (E)	11.14	12.49	10.67	10.65
$\alpha_{[010]}$ (E)	11.14	10.89	12.03	11.77
$\alpha_{[001]}$ (E)	10.95	10.89	13.03	13.12

and anion complex where the hydrogen atom attached covalently with the other group element [3]. The states nearby the Fermi level are dominated by the N-p states of $[NH_2]^-$ anion complex. Therefore the 'p'- states of nitrogen atom play an important role in the conducting properties of these amides. A similar phenomena was also observed in the case of alkali metal azides [41, 42] which are analogous to alkali metal amides with a positive cation and negative anion.

Recently, there is an increased interest in the optical properties of metal hydrides because of their potential applications as switchable mirrors [43]. The optical properties of simple metal hydrides LiH, NaH, MgH_2, $LiAlH_4$, $NaAlH_4$, and $MgAlH_4$ were reported by using the first principles calculations combined with GW calculations [44]. The optical properties of NH_3BH_3 and $Ca(NH_3BH_3)_2$ were studied by our group [45, 46]. To the best of our knowledge, there are no reports available on the optical properties of alkali metal amides. Hence, in this present study efforts have been taken to study the optical properties such as complex di-electric function $\epsilon(\omega)$, refractive index $n(\omega)$, absorption $\alpha(\omega)$ and photo conductivity $\sigma(\omega)$ of alkali metal amides. To calculate these properties we have followed the procedure as outlined in the third chapter.

It is required a dense k-point mesh to calculate the optical properties and hence we have performed the calculations with a k-point mesh of 8x8x6, 8x7x8 for $LiNH_2$, $NaNH_2$, and 12x12x12 for KNH_2, $RbNH_2$ respectively. In Figure 5.4, we have shown the calculated imaginary part of the $\epsilon(\omega)$ as a function of photon energy up

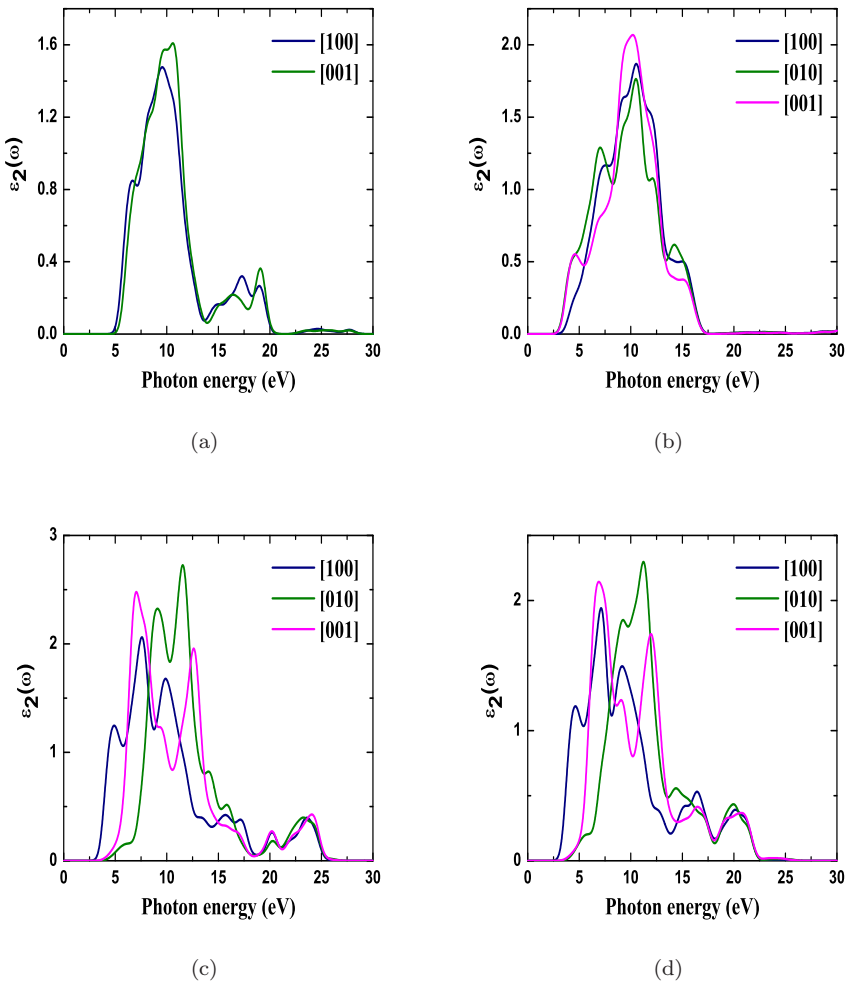

FIGURE 5.4: The imaginary part of the dielectric function $\epsilon_2(\omega)$ of alkali metal amides $LiNH_2$ (a), $NaNH_2$ (b), KNH_2 (c) and $RbNH_2$ (d) as a function of photon energy calculated within the PBE functional with a scissor operator of 1.61 eV for $LiNH_2$, 1.46 eV for $NaNH_2$, 1.8 eV for KNH_2, 1.8 eV for $RbNH_2$.

to 30 eV. A scissors correction to the PBE band gaps is applied in order to get the TB-mBJ values. The calculated spectra show different features for the compounds. For all the compounds the optical absorption starts at the band gap. The prominent peaks observed in the spectra are mainly due to the interband transitions of N-'p'$\rightarrow$ M-'s' states between the valence and conduction band respectively. The calculated $\epsilon_2(\omega)$ can be used to evaluate $\epsilon_1(\omega)$ through Kramer's-Kronig relations which further used to obtain n(ω), $\alpha(\omega)$ and $\sigma(\omega)$.

The calculated refractive index of the metal amides are shown in Figure 5.5. The

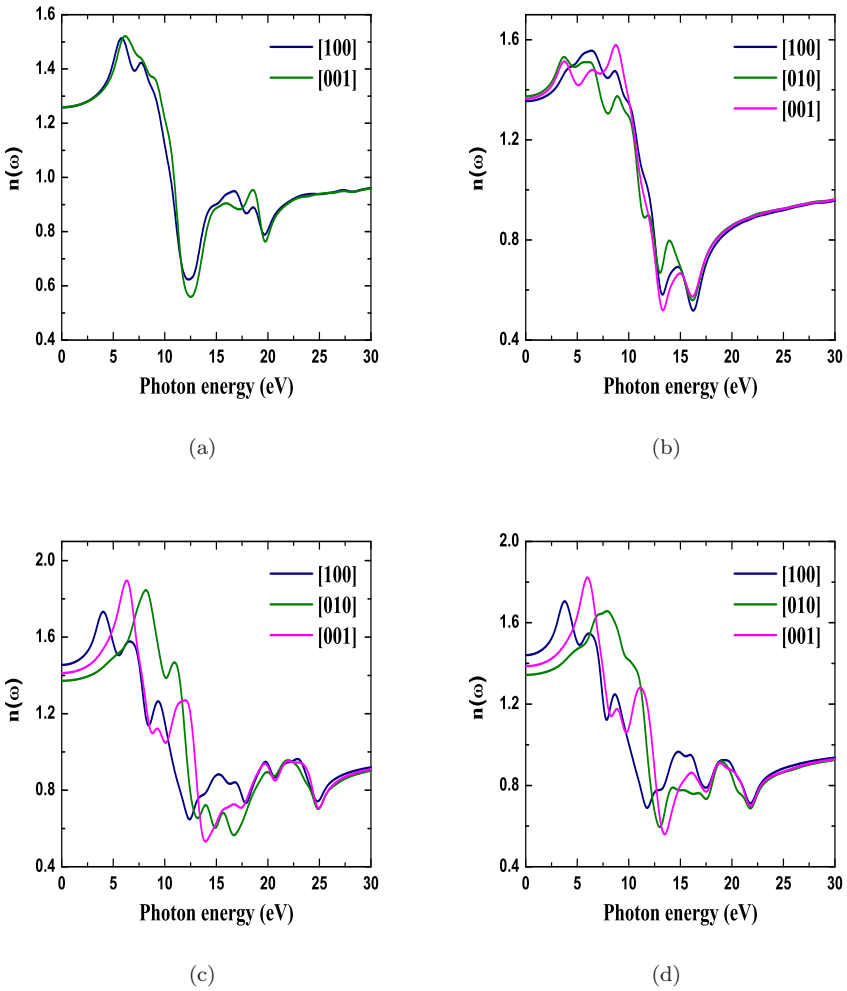

FIGURE 5.5: Refractive index n(ω) of alkali metal amides $LiNH_2$ (a), $NaNH_2$ (b), KNH_2 (c) and $RbNH_2$ (d) calculated as a function of photon energy within the PBE functional with a scissors scissor operator of 1.61 eV for $LiNH_2$, 1.46 eV for $NaNH_2$, 1.8 eV for KNH_2, 1.8 eV for $RbNH_2$.

values of n(0) along the crystallographic directions are presented in Table 5.4. Except $LiNH_2$, the calculated values are different along the three directions indicating the optical anisotropy of the materials. In the case of $LiNH_2$, both $n_{[100]}$ and $n_{[001]}$ are almost identical because of the similar electronic structure of $LiNH_2$ along [100] and [001] directions. We also find that $n_{[100]}(0) \neq n_{[010]}(0) \neq n_{[001]}(0)$ implying that the amides are bi-axial crystals.

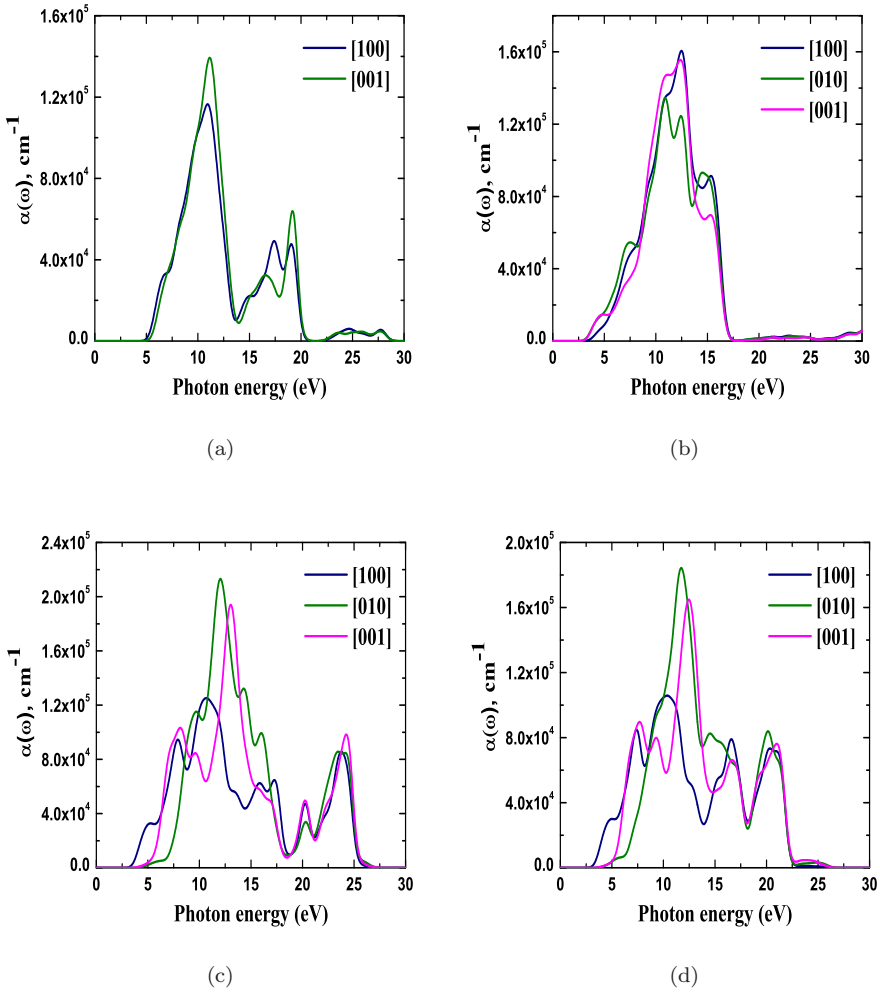

FIGURE 5.6: Optical absorption spectra of alkali metal amides $LiNH_2$ (a), $NaNH_2$ (b), KNH_2 (c) and $RbNH_2$ (d) calculated within the PBE functional with a scissor operator of 1.61 eV for $LiNH_2$, 1.46 eV for $NaNH_2$, 1.8 eV for KNH_2, 1.8 eV for $RbNH_2$.

The optical absorption spectra of alkali metal amides are shown in Figure 5.6. The magnitude of the absorption coefficient is found to be in the order of 10^5 cm^{-1}. The absorption coefficient is found to be maximum in [100] direction for $LiNH_2$, $NaNH_2$ and along [010] direction for KNH_2, $RbNH_2$ at different energies respectively as presented in Table 5.5. The optical absorption spectra of the alkali metal amides are similar to that of analogous alkali metal azides [41, 42]. Photo-conductivity is due to the increase in the number of free carriers when photons are absorbed. The calculated photo conductivity spectra are shown in Figure 5.7. The photoconductivity spectra displays a wide photocurrent response in the absorption

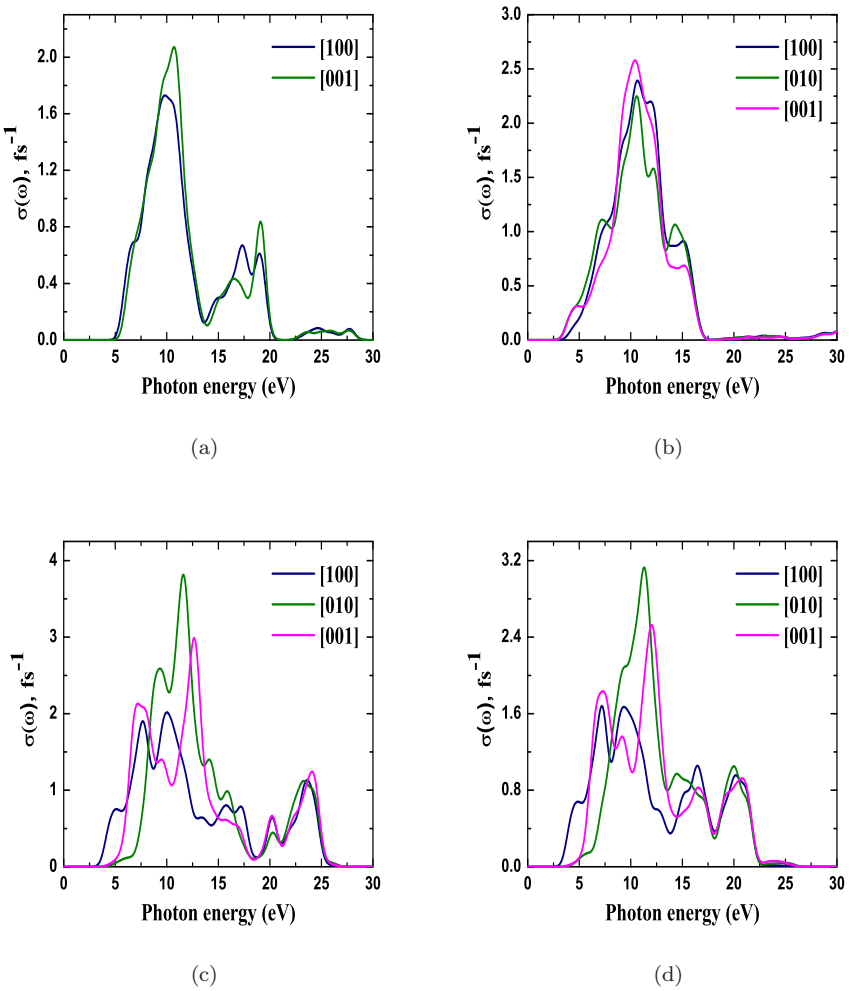

FIGURE 5.7: Optical photoconductivity of alkali metal amides $LiNH_2$ (a), $NaNH_2$ (b), KNH_2 (c) and $RbNH_2$ (d) calculated within the PBE functional with a scissor operator of 1.61 eV for $LiNH_2$, 1.46 eV for $NaNH_2$, 1.8 eV for KNH_2, 1.8 eV for $RbNH_2$.

region of the amides.

5.4 Conclusions

In conclusion, we have studied the structural, electronic, elastic and optical properties of alkali metal amides. We find that GGA functional with PBE parameterizations give better results when compared to the LDA functional. Among

the alkali metal amides $LiNH_2$ has larger bulk modulus due to which the material is stiffer when compared to the other amides. From the calculation of elastic constants, we conclude that all the materials are mechanically stable. Most importantly, the lattice are stiffer along a-axis over the other axis of the amides. The melting temperatures, Tm are calculated through the elastic constants and found that Tm follows the order of bulk moduli of the compounds. The electronic band structures are calculated by means of PBE and TB-mBJ functional and found that all the studied materials have nonconducting nature. The valence region of the band structure is entirely dominated by the states of $[NH_2]^-$ complex with p-states of nitrogen atoms at the Fermi level. The optical properties of the amides are calculated and analyzed. Our study show that the compounds show considerable optical anisotropy in the studied properties.

References

[1] S. A. Shevlin, Z. X. Guo, Chem. Soc. Rev. 38 (2009) 211.

[2] D. Pukazhselvan, V. Kumar, S. K. Singh, Nano Energy 10 (2012) 210.

[3] S. Orimo, Y. Nakamori, J. R. Eliseo, A. Züttel, C. M. Jensen, Chem. Rev. 107 (2007) 4111.

[4] I. P. Jain, P. Jain, A. Jain, J. All. Compd. 503 (2010) 303.

[5] T. Umegaki, J-M. Yan, X. Zhang, H. Shioyama, N. Kuriyama, Q. X, Int. J. Hyd. Ener. 34 (2009) 2303.

[6] P. Chen, Z. Xiong, J. Luo, J. Lin, KL. Tan, Nature 420 (2002) 302.

[7] Gay Lussac, Thènard, R. Phys. Chim. 1 (1809) 337.

[8] A. W. Titherley, J. Chem. Soc. 65 (1894) 504.

[9] L. Fieser, M. Fieser, Reagents for Organic Synthesis, Wiley: NewYork Vol. 1. (1967).

[10] R. E. Mulvey, Chem. Soc. Rev. 27 (1998) 339.

[11] X. Zhang, Z. Jiang, Y. Hou, L. Li, J. Phys.: Condens. Matt. 21 (2009) 275401.

[12] K. Miwa, N. Ohba, S. Towata, Y. Nakamori, S. Orimo, Phys. Rev. B. 71 (2005) 195109.

[13] J. F. Herbst, L. G. Hector, Phys. Rev. B. 72 (2005) 125120.

[14] N. Kamakura, Y. Takeda, Y. Saitoh, H. Yamagami, M. Tsubota, B. Paik, T. Ichikawa, Y. Kojima, T. Muro, Y. Kato, T. Kinoshita, Phys. Rev. B. 83 (2011) 033103.

[15] L. G. Hector Jr, J. F. Herbst, J. Phys.: Condens. Matt. 20 (2008) 064229.

[16] R. S. Chelleppa, D. Chandra, M. Somayazulu, S. A. Gramsch, R. J. Hemley, J. Phys. Chem. B. 111 (2007) 10785.

[17] Y. Zhong, H. Zhou, C. Hu, D. Wang, G. Rao, J. Alloys. Compd. 544 (2012) 129.

[18] D. L. V. K. Prasad, N. W. Ashcroft, R. Hoaffmann, J. phys. Chem. A. 116 (2012) 10027.

[19] X. Huang, D. Li, F. Li, X. Jin, S. Jiang, W. Li, X. Yang, Q. Zhou, B. Zou, Q. Cui, B. Liu, T. Cui, J. Phys. Chem. C. 116 (2012) 9744.

[20] A. Liu, Y. Song, J. Phys. Chem. B. 115 (2011) 7.

[21] Y. Zhong, H. Zhou, C. Hu, D. Wang, A. R. Oganov, J. Phys. Chem. C. 116 (2012) 8387.

[22] M. Segall, P. Lindan, M. Probert, C. Pickard, P. Hasnip, S. Clark, M. J. Payne, J. Phys.: Cond. Matt. 14 (2002) 2717.

[23] D. Vanderbilt, Phys. Rev. B. 41 (1990) 7892.

[24] D. M. Ceperley, B. J. Alder, Phys. Rev. Lett. 45 (1980) 566.

[25] J. P. Perdew, A. Zunger, Phys. Rev. B. 23 (1981) 5048.

[26] J. P. Perdew, K. Burke, M. Ernzerhof, Phys. Rev. lett. 77 (1996) 3865.

[27] H. J. Monkhorst, J. Pack, Phys. Rev. B. 13 (1976) 5188.

[28] S. Grimme, J. Comp. Chem. 27 (2006) 1787.

[29] F. Tran and P. Blaha, Phys. Rev. Lett. 102 (2009) 226401.

[30] D. J. Singh and L. Nordstrom, Planewaves, Pseudopotentials, and the LAPW Method, 2nd ed. (Springer Verlag, Berlin, (2006).

[31] P. Blaha, K. Schwarz, G. Madsen, D. Kvasnicka, and J. Luitz, WIEN2k, An Augmented Plane Wave + Local Orbitals Program for Calculating Crystal Properties (K. Schwarz, Tech. Univ. Wien, Austria, (2001).

[32] Von H. Jacobs, R. Juza, Z. Anorg. Allg. Chem. 391 (1972) 271.

[33] M. Nagib, H. Kistrup, H. Jacobs, Atomkernenergie. 26 (1975) 87.

[34] Nathaniel E. Brese, M. O'Keeffe, Structure and Bonding, 79 (1992) 309.

[35] S. Orimo, Y. Nakamori, A. Züttel, Mat. Sci. Eng. B. 108 (2004) 51.

[36] M. Born and K. Huang, Dynamical Theory of Crystal Lattices (Oxford: Oxford University Press) (1998).

[37] M. E. Fine, L. D. Brown, H. L. Marcus, Scr. Metal. 18 (1984) 951.

[38] R. Hill, Proc. Phy. Soc. Lond. A. 65 (1952) 349.

[39] X. Zhang, Z. Hou, Z. Jiang, Y. Hou, Phys. B. Cond. Matt. 406 (2011) 2196.

[40] S. F. Pugh, Phil. Mag. 45 (1954) 823.

[41] K. Ramesh Babu, G. Vaitheeswaran, Chem. Phys. Lett. 586 (2013) 44.

[42] K. Ramesh Babu, G. Vaitheeswaran, Solid Stat. Sciences. 23 (2013) 17.

[43] J. W. J. Kressemakers, S. J. van der Molen, N. J. Koeman, R. Gunther, R. Griessen, Nature. 406 (2000) 489.

[44] M. J. van Setten, V. A. Popa, G. A. de Wijs, G. Brocks, Phys. Rev. B. 83 (2011) 035422.

[45] Ch. B. Lingam, K. R. Babu, Surya P. Tewari, G. Vaitheeswaran, S. Lèbegue, Phys. Stat. Sol. Rap. Res. Lett. 5 (2011) 10.

[46] Ch. B. Lingam, K. R. Babu, Surya P. Tewari, G. Vaitheeswaran, S. Lèbegue, J. Phys. Chem. C. 115 (2011) 18795.

Chapter 6

High Pressure Study of monoclinic LiN_3 and tetragonal KN_3

Abstract

As chemically pure sources of nitrogen, alkali metal azides under high pressure have the ability to form polymeric nitrogen, an ultimate green high energy density material with energy density three times greater than that of known high energetic materials. With this motive, in this chapter we address the high-pressure behavior of LiN_3 and KN_3 by means of density functional calculations. We found that both LiN_3 and KN_3 are structurally stable up to the studied pressure range of 60 GPa and 20 GPa respectively. The compressibility of both the crystals is found to be anisotropic which is in good agreement with experiment. At ambient conditions both the materials are insulators with a gap of 3.48eV (LiN_3) and 4.08 eV (KN_3) and as pressure increases the band gap decreases and show semiconducting nature at high pressures. Our theoretical study proved that the materials may have the ability to form polymeric nitrogen because of the possible overlapping of N atomic orbitals.

6.1 Introduction

The high pressure behavior of alkali metal azides received much interest by the high energy materials research community because of their capability of forming the polymeric networks of single bonded nitrogen, which is considered to be a high energy density material with energy density nearly three times greater than those of conventional high explosive materials known today. By using sodium azide as starting material, Eremets et al. reported the formation of polymeric nitrogen by combined high pressure X-ray powder diffraction and Raman spectroscopy techniques [1]. Their study concluded that double bonded N atoms of the azide ion become single bonded N atoms at a pressure of 120 GPa. Since NaN_3 and LiN_3 are iso-structural at ambient conditions, it would be of interest to study the pressure effect on LiN_3 with the motive of formation of polymeric nitrogen. Recently Medvedev et al [2] reported the behavior of LiN_3 under high pressures. Their study revealed that the system is stable up to the pressure of 60 GPa, which is in contrast to that of sodium azide that undergoes a set of phase transitions below the pressures of 50 GPa [2]. Recently the compression experiments on heavier alkali metal azides such as CsN_3 and KN_3, which are iso-structural with each other, have been performed. The high pressure experiment on CsN_3 reveals that the system undergoes a sequence of phase transitions starting from ambient tetragonal to high pressure monoclinic structure [3]. In the case of KN_3 the high pressure experiments are carried out up to the pressure of 37 GPa and found that the system may undergo phase transition at around 15.5 GPa [4]. Medvedev et al. performed a combined experimental study of powder X-ray diffraction and Raman spectroscopy and claimed that the system is structurally stable up to the pressure of 20 GPa despite the softening of the E_g librational mode [5].

It is well known that theoretical studies based on density functional theory are accurate to predict the high pressure behavior of different kind of materials. Since the high pressure behavior of LiN_3 and KN_3 is quite different compared to that of iso-structural NaN_3 and CsN_3 respectively, the density functional theory study of high pressure behavior of LiN_3 and KN_3 would be desirable. In addition to understand the behavior of LiN_3 and KN_3 under high pressure, it is essential to study the physical and chemical properties of the systems under high pressure.

As we have discussed earlier in chapter 3, the van der Waals interactions play a major role in crystal binding of the azides therefore in this present chapter we present the study of high pressure behavior of monoclinic LiN_3 and tetragonal KN_3 using first principles density functional theory calculations including van der Waals interactions. In particular, we aim to explain the structural properties, electronic band structure and vibrational properties of the azides and the changes brought in them by the application of pressure as they are very important in understanding the formation of polymeric nitrogen.

6.2 Computational details

All the calculations are performed within density functional theory using CASTEP code which uses a plane wave expansion in reciprocal space [6, 7]. The kinetic energy cut-off value for plane wave expansion is selected as 520 eV. The energy calculations in the first irreducible Brillouin zone are performed with a 5x8x5 k-point mesh using Monkhorst-Pack scheme [8]. Vanderbilt type ultrasoft pseudopotentials are employed to represent the Coulomb interaction between the valence electrons and ion core [9]. The exchange-correlation energy is evaluated with the generalized gradient approximation (GGA) of Perdew-Burke-Ernzerhof method [10]. To treat the vdW forces we have used semi-empirical dispersion correction scheme proposed by Grimme with PBE functional (PBE+G06) [11].

We performed the calculation by adopting the experimental crystal structure of LiN_3 [12], a=5.627$\mathring{A}$, b=3.319$\mathring{A}$, c=4.979$\mathring{A}$, and β=107.4^0 as the initial structure and it is relaxed to allow the ionic configurations, cell shape, and volume to change at ambient pressure. Starting from the optimized crystal structure of lithium azide at ambient pressure, we applied hydrostatic pressure up to 60 GPa. The external pressure was gradually increased by an increment of 1 GPa in each time. Under a given pressure, the internal co-ordinates and unit cell parameters of the lithium azide crystal were determined by minimizing the Hellmann-Feynmann force on the atoms and the stress on the unit cell simultaneously. In the case of KN_3, the calculations were performed by adopting the experimental crystal structure of KN_3

[13], a=6.113 $\mathring{A}$, c=7.094 $\mathring{A}$ with four molecules per unit cell (two units per primitive cell) as the initial structure, and it is relaxed to allow the ioinc configurations, cell shape, and volume to change at ambient pressure. Starting from the optimized crystal structure of KN_3 at 0 GPa, we applied hydrostatic pressure up to 20 GPa. Under a given pressure, the internal co-ordinates and unit cell parameters of the potassium azide were determined by minimizing the Hellmann-Feynmann force on the atoms and the stress on the unit cell simultaneously. In the geometry relaxation, the self-consistent convergence on the total energy is 5x10^{-7}eV/atom and the maximum force on the atom is found to be 10^{-4}eV/$\mathring{A}$. The vibrational frequencies have been calculated from the response to small atomic displacements within the linear response approach as implemented in CASTEP code [14, 15].

6.3 Results and discussion

6.3.1 Structural properties of LiN_3 and KN_3 under high pressure

In order to study the pressure effect on LiN_3 and KN_3 systems, we have taken the ambient optimized crystal structure and applied hydrostatic pressure of 60 GPa on monoclinic LiN_3 system with successive intervals of 5 GPa and 20 GPa to the tetragonal KN_3 system with successive intervals of 2 GPa, respectively. The calculated equation of state (EOS) of both LiN_3 and KN_3 are compared with available experimental data in Figure 6.1 (a) and 6.1 (b). For both the compounds the volume compression upon pressure with DFT+D method (PBE+G06 functional) is found to be in excellent agreement with experimental volume reduction. In particular, the calculated EOS of KN_3 with DFT+D is in excellent agreement with experiment over the entire studied pressure range. This clearly shows that DFT+D describe the KN_3 system accurately than that of usual DFT [16–18].

The bulk modulus, B_0, and its pressure derivative B_0' can be deduced from the pressure and volume data of the crystal. In the present study, the calculated pressure-volume data of LiN_3 and KN_3 using the PBE+G06 functional are fitted to the Murnaghan's equation of state and the corresponding values are presented

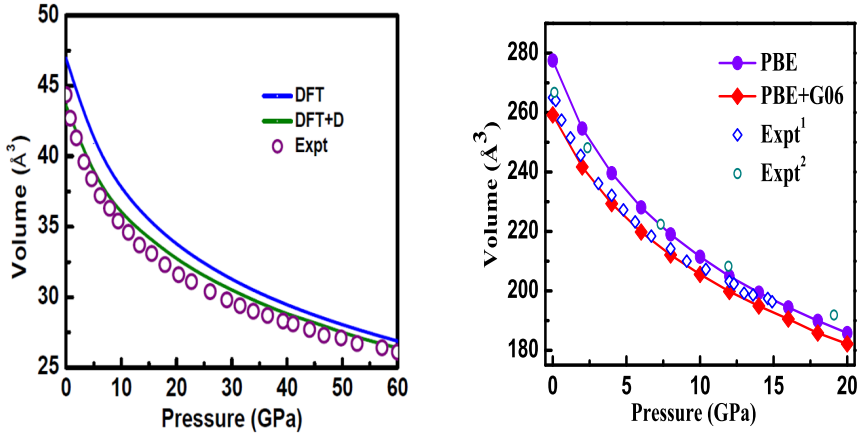

(a) (b)

FIGURE 6.1: (a) Equation of state of LiN_3. Experimental values are taken from ^{2}Ref[2] (b) Equation of state of KN_3. Experimental values are taken from ^{1}Ref [4] and ^{2}Ref [5]

Table 1. The bulk modulus and its pressure derivative for LiN_3, are found to be 36.3 GPa and 4.108, respectively whereas for KN_3 the calculated values are 26.3 GPa and 3.93 respectively. When compared with the experimental value of B_0 = 19.1± 1.4 GPa and $B_0' = 7.3\pm 0.5$ [2], the calculated value of B_0 for LiN_3 is higher which can be attributed to the fact that the equilibrium volume is lower by -1.8 % compared to experiment. And also, the experimental B_0' value is higher than the present theoretical value which might also affect the bulk modulus value. Since the experimental values are resulted from four measurements, we would expect that that still some more experiments are required in determining the bulk modulus value of LiN_3. On the other hand the present theoretical values of B_0 and B_0' for KN_3 are in good comparison with the experimental values of 27.4 GPa and 4.4.

Over the studied pressure range of both the compounds, we could not observe any discontinuity in the calculated EOS indicating that both the systems are structurally stable with no phase transition. In Figure 6.2 (a) we have shown the pressure dependence of lattice parameters of LiN_3. Qualitatively our calculations reproduce the trend of reduction of lattice parameters upon pressure. The deviation from the experimental data is found to be more for the c-axis with both the DFT and DFT+D methods. The reason for this behaviour might be due to

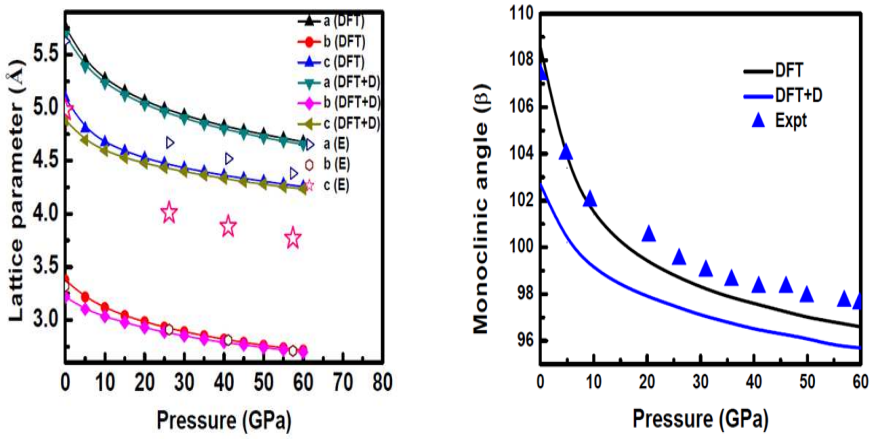

(a) (b)

FIGURE 6.2: (a) Lattice parameters variation of LiN_3 with pressure (b) Monoclinic angle variation of LiN_3 with pressure. Experimental values are taken from [2]

the fact that error in our ambient pressure value of 'c' lattice parameter is more compared to that of the other axis.

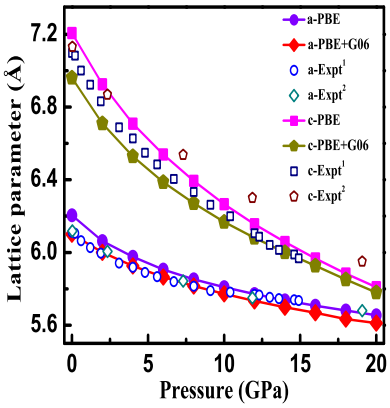

(a)

FIGURE 6.3: Lattice parameters variation of KN_3 with pressure along with experimental data taken from [1]Ref[4] and [2]Ref[5]

The pressure dependence of lattice parameter 'b' is found to be very good agreement with our calculations using DFT+D with error less than 0.5 over the entire pressure range. It can be observed that the b-axis is the most compressible which is also consistent with experimental finding. In chapter 3, we have predicted that

C_{22} is lowest among the three principal elastic constant values indicating that the lattice would be more compressible along the b-axis of the monoclinic LiN_3 crystal. This fact is confirmed by the present high pressure study of LiN_3. This also reveals the fact that the knowledge of elastic constants is essential to know about the compressibility behavior of the solids. In Figure 6.2 (b) we have shown the pressure dependence of monoclinic angle β in comparison with experiment. We can see that the error is quite lower with DFT than that of DFT+D. Overall, our high pressure study on LiN_3 suggests that the compressibility of LiN_3 is anisotropic as the lattice parameters have different compression behaviour with pressure, which is in good accord with experiment.

The pressure dependence of lattice parameters of KN_3 along with experimental data is shown in Figure 6.3. Clearly, the lattice parameter 'a' calculated with DFT+D is found to be in close agreement with experiment when compared to c-axis. Our calculations clearly show that the compressibility of KN_3 is anisotropic as the c-axis is more compressible than a-axis. This result is also consistent with both the experiments. From the calculated elastic constants of KN_3, we came to the conclusion that c-axis more compressible than a-axis as the value of C_{33} is lower than that of C_{11} as discussed in chapter 3.

6.3.2 Electronic Structure of LiN_3 and KN_3 under pressure

The calculated electronic band structures of LiN_3 and KN_3 at 60 GPa and 16 GPa are shown in Figure 6.4 (a) and 6.4 (b) respectively. In Figure, the solid and filled circles represent the band structure obtained from DFT (PBE) and DFT+D (PBE+G06) methods. Clearly, the band energies calculated from DFT and DFT+D are found to be same in both the compounds under pressure. This is may be due to the fact that as pressure increases the overlapping of N-p orbitals increases which in turn diminishes the dispersion forces between the azide ion layers.

The pressure dependence of the band gap values of LiN_3 and KN_3 calculated through the DFT and DFT+D are presented in Figure 6.5 (a) and 6.5 (b) respectively. The magnitude of the band gap is decreasing monotonically as pressure increases in both the compounds implying the possibility of these compounds

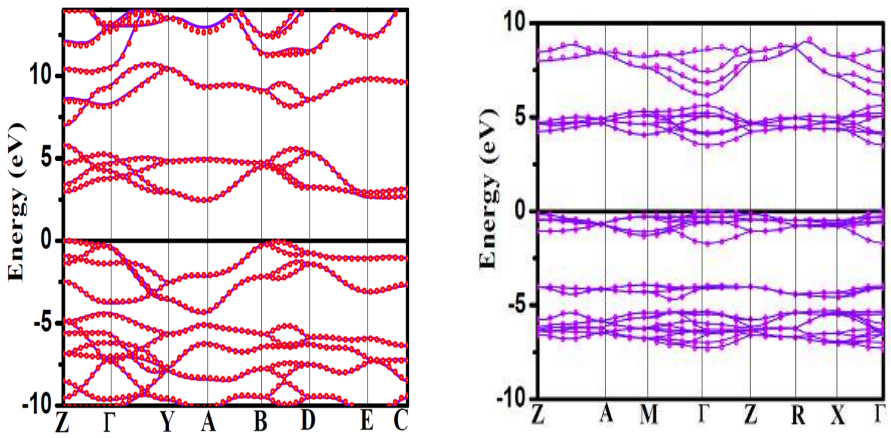

(a) (b)

FIGURE 6.4: (a) Electronic band structure of LiN_3 calculated at pressure of 60 GPa (b) Electronic band structure of KN_3 calculated at pressure of 16 GPa.

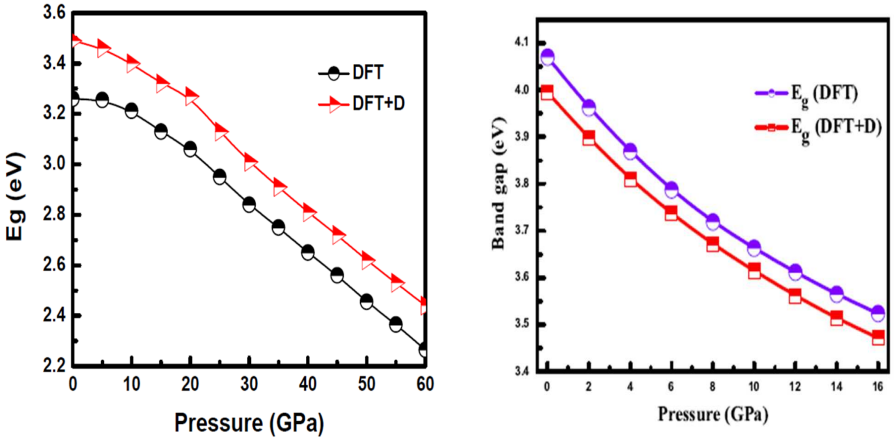

(a) (b)

FIGURE 6.5: Band gap variation of (a) LiN_3 (b) KN_3 with pressure

becoming semiconductors at high pressures. The same is also true with the calculated band gap values using the TB-mBJ functional. This is a significant feature in achieving the polymeric nitrogen which is found to be semiconductor in nature.

We have calculated the total and partial density of states of LiN_3 and KN_3 within the DFT+D (PBE+G06) method. As discussed in Figure 3.4 (a) and 3.5 (a) of chapter 3, in both the compounds the states in valence band including the bands at the Fermi level are entirely due to the '*p*'-states of N atoms and those in

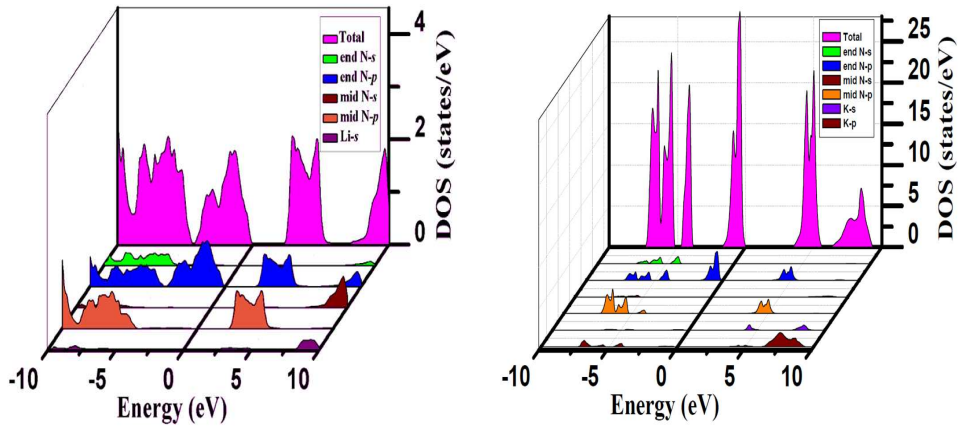

(a) (b)

FIGURE 6.6: (a) The total and partial density of states of LiN_3 calculated at 60 GPa (b) The total and partial density of states of KN_3 calculated at 16 GPa

conduction band are from the '*s*-states of metal atom respectively. In detail, the states at the Fermi level are due to '*p*'-states of end N atom whereas the states lying at -5 eV are due to the p-states of mid N atom. The metal atom states do not play much role in the valence band indicating that in both the compounds ionic bonding is dominating, which is a well-known feature of the materials having a positive cation and a negative anion similar to that of known alkali halides, a well-known ionic compounds. As pressure increases, the states of end N and mid N are delocalizing as shown in Figure 6.6 (a) and 6.6 (b) for LiN_3 and KN_3 respectively. One can also notice that the width of the energy interval of p-states increases in the valence band. This is due to the fact that as pressure increases the intra molecular interactions between the N atoms of the azide ion enhances and therefore the states become broadened. A significant feature of the calculated DOS under pressure is that the contribution of metal atom states in the conduction band increases. Over all, from the study of DOS of LiN_3 and KN_3 we came to the conclusion that the azide ion plays a major role in bonding properties of the alkali metal azides.

6.3.3 Effect of pressure on phonon frequencies of LiN_3 and KN_3

In order to understand the intramolecular and intermolecular interactions under compression, we calculated the vibrational frequencies for the optimized crystal structures of LiN_3 up to the pressure of 60 GPa at a pressure step of 5 GPa and are shown in Figure 6.7. It can be clearly observe that as pressure increases all the vibrational frequencies of all modes from M1 to M9 increases with increase in pressure, except the bending modes of azide ion from M6 to M7 which decreases and have minima at about 20 GPa. This clearly shows that the intramolecular interaction enhances under the application of pressure. In Table 6.1, we have shown the coefficients for the pressure-induced shifts of the vibrational frequencies of all vibrational modes of LiN_3 from M1 to M9. These values are obtained by a linear fit of the vibrational frequencies with respect to pressure. From the calculated values it is clear that different vibrational modes show distinctly different pressure dependent behavior. The pressure-coefficients for lattices modes are found to be higher than that of internal modes, indicating that the lattice modes show most significant shift over internal modes. The lattice mode M5 has high pressure coefficient of 5.1 cm^{-1}/GPa and among the internal modes, the asymmetric stretching modes of azide ion M9 has high pressure coefficient of 3.1 cm^{-1}/GPa. Over all the behavior of vibrational modes under compression indicates that the intermolecular and intramolecular interactions increases. The observed frequency shifts are more for lattice modes compared to the internal modes under compression. This implies that intermolecular interaction is affected more significantly than the intramolecular interaction under compression.

The knowledge of the volume dependencies of the vibrational modes allows to calculate the Grüneisen parameters (γ_i) associated with them. The Grüneisen parameter of i^{th} vibrational mode can be defined as

$$\gamma_i = -\frac{\partial(ln\nu_i)}{\partial(lnV)} \tag{6.1}$$

The calculated Grüneisen parameters (γ_i) of LiN_3 resulting from a linear fit of the ln ν as a function of ln V are listed in Table 6.1. It can be observed from

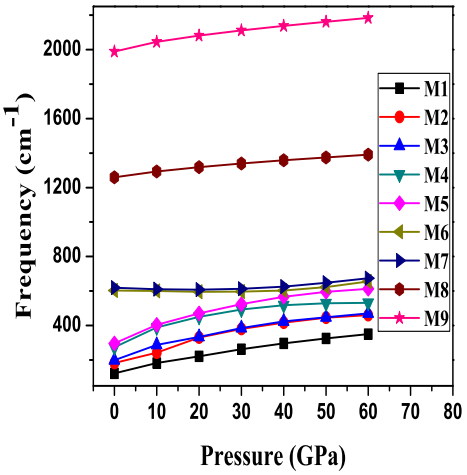

FIGURE 6.7: (Colour online) Pressure-induced shifts of vibrational frequencies of LiN_3.

TABLE 6.1: The calculated pressure coefficients (PC) (cm^{-1}/GPa) and Grüneisen parameters (γ) of the vibrational frequencies of the vibrational modes of monoclinic LiN_3 from the linear fit of the present GGA results.

Mode	Symmetry	PC (cm^{-1}/GPa)	γ
M1	B_u	3.7	0.9
M2	B_g	4.7	1.1
M3	A_g	4.3	1.4
M4	A_u	4.1	1.3
M5	B_u	5.1	1.5
M6	B_u	0.7	1.6
M7	A_u	0.9	1.6
M8	A_g	2.1	1.7
M9	B_u	3.2	1.8

Table 6.1 that the calculated γ is high for lattice modes and the values are low for internal modes which are entirely due to the azide ion vibrations. This also implies that the change in lattice parameters and thereby the volume with pressure has large affect on vibrational modes especially lattice modes whereas the vibrational frequencies of azide ion has less influence by the pressure.

We now discuss about the pressure induced phonon frequency shifts of KN_3 under the application of hydro static compression. In Figure 6.8 (a) we have shown the pressure dependence of lattice modes E_g(T), E_g(R) and B_{1g} (R). The frequencies of all the external modes increases with pressure except librational E_g(T) mode. The E_g phonon mode, which is due to the translation of the K

metal ion in the plane perpendicular to the z-axis as shown in Figure 6.8 (b), becomes softening under pressure with a pressure coefficient of -0.26 with PBE and -1.01 with PBE+G06, as observed in experiment [5]. The pressure dependence of bending modes of azide ion is shown in Figure 6.9 (a).

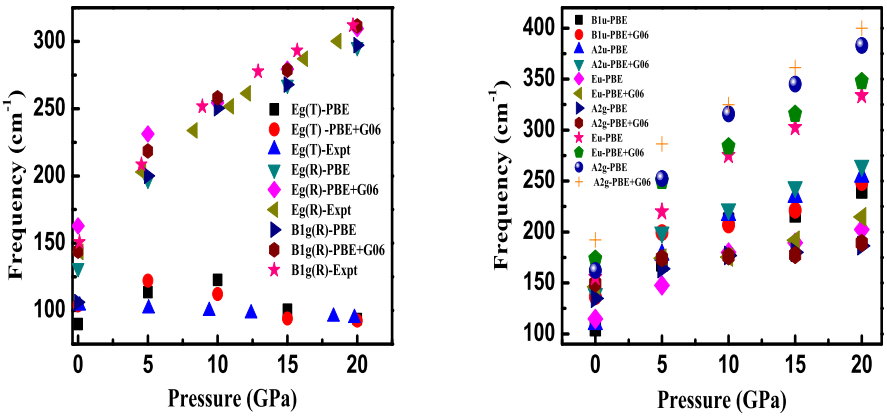

(a) (b)

FIGURE 6.8: (a) The dependence of E_g(T), E_g(R), and B_{1g}(R) mode frequencies of KN_3 with pressure. Also shown experimental data of Medvedev et al., [5] (b) Effect of pressure on external or lattice mode frequencies of KN_3.

We find an interesting feature of decrease in frequency of the A_{2u} symmetric bending mode with pressure and the normal mode representation of the mode along with the E_g mode of KN_3 is shown in Figure 6.10. This kind of decrease in symmetric bending mode frequency of the azide ion with pressure was earlier observed in the case of AgN_3 [19] and LiN_3 below a pressure of 30 GPa [16].

So the decrease in A_{2u} mode frequency is not surprising and it merely suggests that the pressure enhances the interaction between the N atoms in the azide ion. In Figure 6.9 (b) and 6.9 (c) we have shown the Infrared active asymmetric (E_u) stretching mode and the Raman active symmetric (B_{2g}, A_{1g}) stretching mode behavior of the azide ion under pressure. The frequency of these three stretching modes increases monotonically with pressure with a pressure coefficients as shown in Table 6.2. As observed in experiment [5] we could not find any discontinuity in these internal Raman active symmetric stretching modes under pressure. Overall from the study of vibrational frequencies of optical modes of KN_3, it is clear that the pressure coefficients of external modes are higher than that of internal

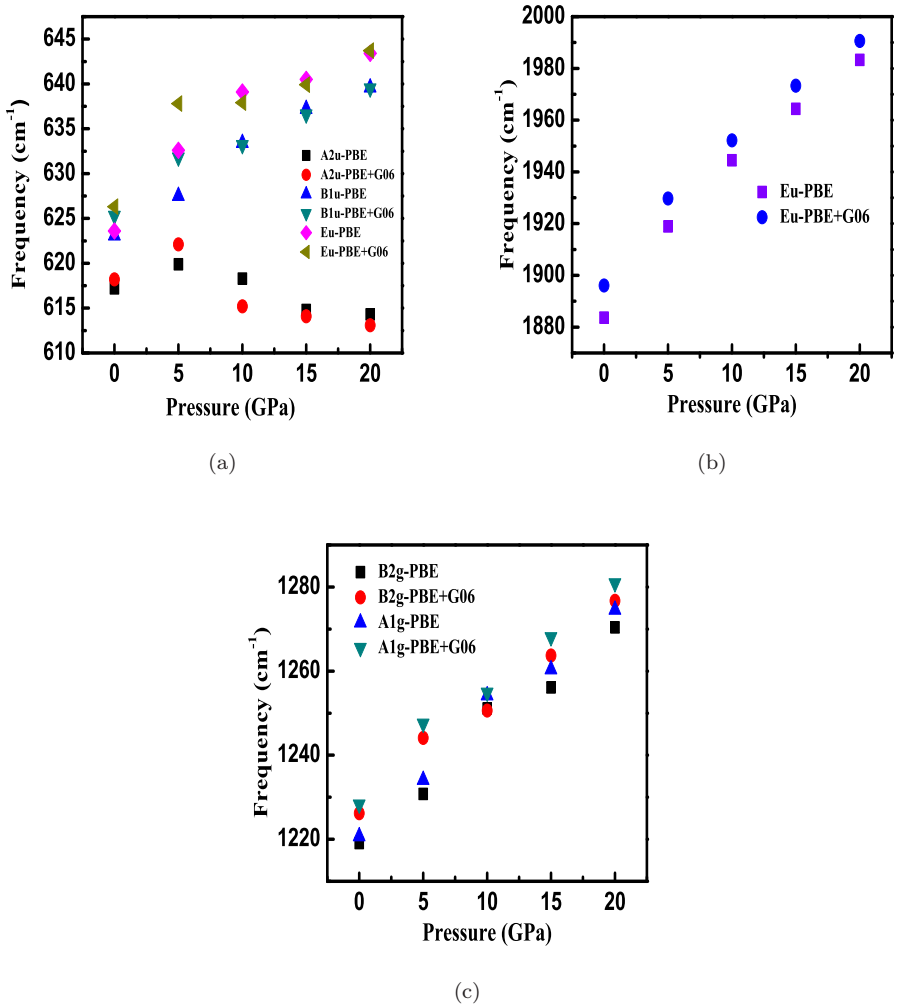

FIGURE 6.9: (a) Variation of bending mode frequencies of KN_3 with pressure (b) and (c) Pressure effect on stretching mode frequencies of KN_3.

modes implying the enhancement of intermolecular interactions under pressure and also the pressure study on phonon modes reveals that despite the softening of E_g(T) mode, the lattice is still stable due to the strong increase in intramolecular interactions under the studied pressure range. From our study we propose that for further compression the tetragonal KN_3 crystal may show lattice instability.

In order to understand the volume dependence of the vibrational modes we have calculated the Grüneisen parameter (γ_i) of each mode. The calculated γ_i for each mode is presented in Table 6.3. The γ_i for E_g(T) and A_{2u} mode are obtained to be negative whereas the value is positive for all the other modes. It can also be

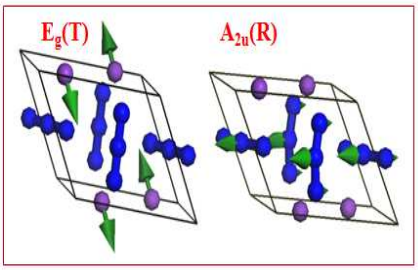

FIGURE 6.10: Normal mode representation of two softening modes E_g (T) and A_{2u} of KN_3.

TABLE 6.2: The calculated pressure coefficients, P_c in (cm^{-1}/GPa) tetragonal KN_3 within PBE and PBE+G06 functionals. T and R corresponds to Translational and Rotational vibrations respectively. IA and RA infers the Infrared active and Raman active modes of KN_3.

Mode Sym	P_c	
	PBE	PBE+G06
E_g(T) (RA)	-0.26	-1.01
$B_{1u}(T)$	6.36	4.92
B_{1g}(R) (RA)	8.98	7.89
A_{2u}(T) (IA)	5.91	6.91
E_u(T) (IA)	4.35	3.11
E_g(R) (RA)	7.99	6.88
A_{2g}(T)	2.38	1.66
E_u(T) (IA)	8.78	8.29
A_{2g}(R)	10.67	9.80
A_{2u} (IA)	-0.21	-0.37
B_{1u}	0.85	0.66
E_u	0.95	0.74
B_{2g} (RA)	2.56	2.41
A_{1g} (RA)	2.68	2.52
E_u (IA)	4.89	4.24

TABLE 6.3: The calculated Grüneisen parameters (γ) of all vibrational modes of tetragonal KN_3 within PBE and PBE+G06 functionals.

Mode Symmetry	Grüneisen parameter (γ)	
	PBE	PBE+G06
E_g(T) (RA)	-0.13	-0.37
$B_{1u}(T)$	2.05	1.38
B_{1g}(R) (RA)	2.54	1.88
A_{2u}(T) (IA)	2.09	1.57
E_u(T) (IA)	1.45	0.86
E_g(R) (RA)	2.03	1.54
A_{2g}(T)	0.79	0.52
E_u(T) (IA)	1.92	1.70
A_{2g}(R)	2.13	1.78
A_{2u} (IA)	-0.01	-0.02
B_{1u}	0.06	0.05
E_u	0.07	0.06
B_{2g} (RA)	0.10	0.09
A_{1g} (RA)	0.11	0.09
E_u (IA)	0.13	0.12

noticed that the magnitude of γ_i is larger for lattice modes than those of internal modes involving azide ion vibrations alone.

6.4 Conclusions

In conclusion we have studied the high pressure behavior of monoclinic LiN_3 and tetragonal KN_3 molecular crystals using density functional theory including van der Waals interactions. The calculated ground state properties are greatly improved by the DFT+D method over the usual DFT results. The calculated P-V relation for both the compounds is well reproduced by calculations with the DFT+D method. Our calculations clearly show that the compressibility of the materials is anisotropic which is also consistent with experiment. The calculated electronic band structure of LiN_3 and KN_3 clearly shows that both the compounds are insulators. We also found that dispersion interactions are largely affecting the band structure of KN_3 system over LiN_3 system and the band energies are enhanced with the inclusion of dispersion interactions. At high pressures dispersion

interactions does not play much role in these compounds. As pressure increases the band gap decreases implying possibility to become semiconductor which is a precursor for the formation of polymeric nitrogen. The total and partial density of states of LiN_3 and KN_3 are also supporting this fact. As pressure increases the states become broadening implying the delocalization of the azide ion states which is also a witness towards the formation of polymeric nitrogen.

References

[1] Eremets, M. I.; Popov, M. Yu.; Trojan, I. A.; Denisov, V. N.; Boehler, R.; Hemley, R. J. J. Chem. Phys. 120 (2004) 10618.

[2] Medvedev, S. A.; Trojan, I. A.; Eremets, M. I.; Palasyuk, T.; Klapötke, T. M.; Evers, J. J. Phys.: Condens. Matter, 21 (2009) 195404.

[3] Dongbin Hou, Fuxiang Zhang, Cheng Ji, Trevor Hannon, Hongyang Zhu, Jianzhe Wu, and Yanzhang Ma, Phys. Rev. B. 84 (2011) 064127.

[4] Cheng Ji, Fuxiang Zhang, Dongbin Hou, Hongyang Zhu, Jianzhe Wu, Ming-ChienChyu, Valery I.Levitas, YanzhangMaa, J. Phys. Chem. Solids 72 2011 736 .

[5] S. A. Medvedev, T. Palasyuk, I. A. Trojan, J. Evers, T. M. Klapötke and M. I. Eremets, Private communications (2011).

[6] M. C. Payne, M. P. Teter, D. C. Allan, T. A. Arias, J. D. Joannopoulos, Rev. Mod. Phys. 64 (1992) 1045.

[7] M. Segall, P. Lindan, M. Probert, C. Pickard, P. Hasnip, S. Clark, M. J. Payne, J. Phys:. Cond. Matt. 14 (2002) 2717.

[8] H. J. Monkhorst, J. Pack, Phys. Rev. B. 13 (1976) 5188.

[9] D. Vanderbilt, Phys. Rev. B. 41 (1990) 7892.

[10] J. P. Perdew, K. Burke, M. Ernzerhof, Phys. Rev. lett. 77 (1996) 3865.

[11] S. Grimme, J. Comp. Chem. 27 (2006) 1787.

[12] G. E. Pringle, D. E. Noake, Acta Crystallogr. B 24 (1968) 262.

[13] U. Z. M*ü*ller, Z. Anorg. Allg. Chem. 392 (1972) 159.

[14] X. Gonze, Phys. Rev. B. 55 (1997) 10337.

[15] K. Refson, P. R. Tulip, S. J. Clarke, Phys. Rev. B. 73 (2006) 155114.

[16] K. Ramesh Babu, Ch. Bheema Lingam, Surya P. Tewari, G. Vaitheeswaran, J. Phys. Chem. A. 115 (2011) 4521.

[17] G. Vaitheeswaran, K. Ramesh Babu, J. Chem. Sci 124 (2012) 1391.

[18] K. Ramesh Babu, G. Vaitheeswaran, Chem. Phys. Lett. 533 (2012) 35.

[19] W. Zhu, H. Xiao, J. Solid State Chem. 180 (2007) 3521.

Chapter 7

Structural and vibrational properties of nitogen rich Guanidinium-2-Methyl-5-nitraminotetrazolate

Abstract

We present density functional theory calculations on the crystal structure, equation of state, vibrational properties and electronic structure of nitrogen rich solid energetic material guanidinium 2-methyl-5-nitramino tetrazolate (G-MNAT). The ground state structural properties calculated with dispersion corrected density functionals are in good agreement with experiment. The computed equilibrium crystal structure is further used to calculate the equation of state and zone-center vibrational frequencies of the material.

7.1 Introduction

Energetic materials have wide range of applications in both civilian and military sectors. For example, energetic materials are used in agriculture, mining, building demolition, pyrotechnics, coal blasting, tunneling, welding etc. Most importantly they are useful in fire fighting in war heads and as rocket boosters in aero space applications [1–4]. In general, energetic materials contain both fuel and oxidizer and reacts readily with the release of huge chemical energy stored within their molecular structures upon external stimulus such as heat, impact, shock, electric spark etc. The amount of energy released from an energetic material within a short time is considerably large when compared to the normal materials [5].

The detonation products of most of the energetic materials are water vapour, carbon monoxide CO, and carbon-di-oxide CO_2 [5, 6]. These are well known green house gases that greatly affect the temperature of the earth. The best remedy for this problem is to have energetic materials that only give environmentally clean and eco-friendly detonation products. Nitrogen-rich compounds meet these demands quite well as they tend to show a high energy content and most importantly, their detonation products are pure nitrogen gas which is environment friendly [6]. Eremets et al., have synthesized polymeric nitrogen which is considered to be a green high energy density material [7]. Very recently, Fendt et al., synthesized tetrazole based nitrogen rich energetic materials whose performance characteristics are found to be in good accord with well known high explosives [8].

High pressure study of energetic materials is a challenging task both from theory and experiment. In a laboratory it is very difficult to perform high pressure experiments on high energetic materials due to safety reasons. On the other hand, an effective way of studying high pressure behavior of energetic materials can be achieved through computer simulations [9–11]. Density Functional Theory (DFT) is a successful tool in simulating and predicting the physical and chemical properties of a wide spectrum of energetic materials [12, 13]. However, most of the energetic materials have complicated crystal structures with weak inter molecular interactions and hence the investigation of different physical and chemical properties of energetic materials through DFT is really a challenging task [14]. In

recent years, the advances in DFT methods have enabled us to describe effectively the materials with weak dispersive interactions [15, 16]. There are few theoretical studies available based on dispersion corrected density functional methods to study the structural properties of various energetic materials [14].

For any energetic material, the physical and chemical properties such as band structure, bonding and vibrational properties are very important in order to understand the stability and thereby the sensitivity of the materials. These properties are directly related to the molecular packing, symmetry of the crystal structure and most importantly the crystal density. Therefore it is quite essential to know about the crystal structure of the energetic materials and the structural modifications that occur upon the application of high pressures. To the best of our knowledge there are no theoretical reports available to study the crystal structure, equation of state and vibrational properties of crystalline guanidinium 2-methyl-5-nitraminotetrazolate (G-MNAT). It is a well known fact that the electronic band gap plays a major role to understand the sensitivity of energetic materials [17]. Hence, we also aim to study the energy band structure and also the variation of band gap with pressure. The remainder of the paper is organized as follows: A brief description of our computational details is presented in section 2. The results and discussion are presented in section 3 followed by summary of our conclusions in section 4.

7.2 Computational details

The calculations are performed using plane wave pseudo potential method based on DFT [18]. The interactions between the ions and electrons are described by using Vanderbilt ultrasoft pseudo potentials [19]. For all the calculations we have included the $1s^1$ electrons for hydrogen, $2s^2$, $2p^2$ electrons for carbon, $2s^2$, $2p^3$ electrons of nitrogen and the $2s^2$, $2p^4$ states of oxygen. Both local density approximation (LDA) of Ceperley and Alder [20] parameterized by Perdew and Zunger (CA-PZ) [21] and also the generalized gradient approximation (GGA) with the Perdew-Burke-Ernzerhof (PBE) [22] parameterizations are used for the exchange-correlation potentials. The calculations are performed using an energy cut-off of

640 eV for the plane wave basis set. Integrations in the Brillouin zone are performed according with a 5x3x2 Monkhorst-Pack grid scheme [23] k-point mesh. The changes in the total energies with the number of k-points and the cut-off energy were tested to ensure the convergence within one meV per atom. To treat vdW interactions efficiently, we have used the vdW correction to the exchange-correlation functional of standard density functional theory at semi empirical level. In the present study we have used the recently developed schemes by Grimme [15], Tkatchenko - Scheffler [16] approaches in GGA. These semi-empirical approaches provide the best compromise between the cost of first principles evaluation of the dispersion terms and the need to improve non-bonding interactions in the standard DFT description.

7.3 Results and discussion

7.3.1 Structural properties

At ambient pressure, solid G-MNAT exists in monoclinic structure with space group $P2_1$ and contain two molecules per unit cell (z=2) as shown in Figure 7.1 (a) [8]. The molecular structure of G-MNAT is shown in Figure 7.1 (b). The experimental crystal structure is taken as starting in put for the calculations and then we apply usual density functionals LDA (CA-PZ), GGA (PBE) and also the dispersion corrected density functionals PBE+TS and PBE+G06. The calculated lattice parameters are presented in Table 7.1 together with the experimental values [8].

The computed crystal volume is underestimated by -8.3% using CA-PZ functional and overestimated by 7.1% with PBE computation. This large discrepancy is due to the fact that the present studied compound is a molecular solid with weak dispersion forces which the usual LDA and GGA functionals are inadequate to treat these forces. On the other hand, the computation carried out by dispersion corrected density functionals describe well the crystal structure and the computed volume result in low errors. The equilibrium crystal volume is overestimated by 1.7% using PBE+TS functional and underestimated by -0.6% with PBE+G06 functional. Clearly, the dispersion corrected density functionals are efficient to

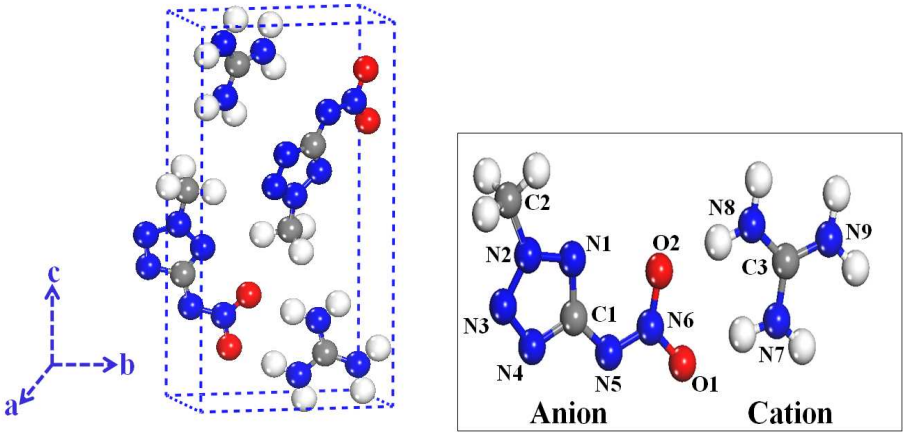

FIGURE 7.1: Crystal structure of G-MNAT (a), Molecular structure of G-MNAT (b). In figure grey ball, white ball, blue ball and red ball indicates, carbon, hydrogen, nitrogen and oxygen atoms respectively.

TABLE 7.1: Ground state structural properties of crystalline G-MNAT calculated using various exchange-correlation functionals. Experimental data have been taken from Fendt et. al [8]

XC functional	a (Å)	b (Å)	c (Å)	β^0	ρ	V (Å^3)
CA-PZ	3.5167	7.8685	13.7515	94.447	1.7785	379.38
PBE	4.7258	7.6277	15.1658	105.96	1.2837	525.608
PBE+TS	3.7123	8.0569	14.1369	95.4297	1.6029	420.91
PBE+G06	3.6111	8.0296	14.2334	95.35	1.642	410.909
Expt	3.6562	8.1552	13.9458	95.919	1.6314	413.606

	B_0	B_0'
PBE+G06	15.3	4.657

describe the crystal structure of G-MNAT. In particular, the PBE+G06 functional describes the system with less error compared to PBE+TS functional. Thus, for all rest of the calculations we use PBE+G06 functional.

The equation of state for G-MNAT crystal is obtained by performing the hydrostatic compression simulation and shown in Figure 7.2 (a). From the figure, it can be seen that the volume decreases monotonically with $V/V_0 = 77\%$ at 10GPa. The lattice constants as a function of pressure are shown in Figure 7.2 (b). Among the three lattice parameters, the reduction in lattice parameter 'a' with pressure is found to be more when compared to other with $a/a_0 = 86\%$ while $b/b_0 = 98\%$. This implies that the G-MNAT lattice is more compressible along a-axis

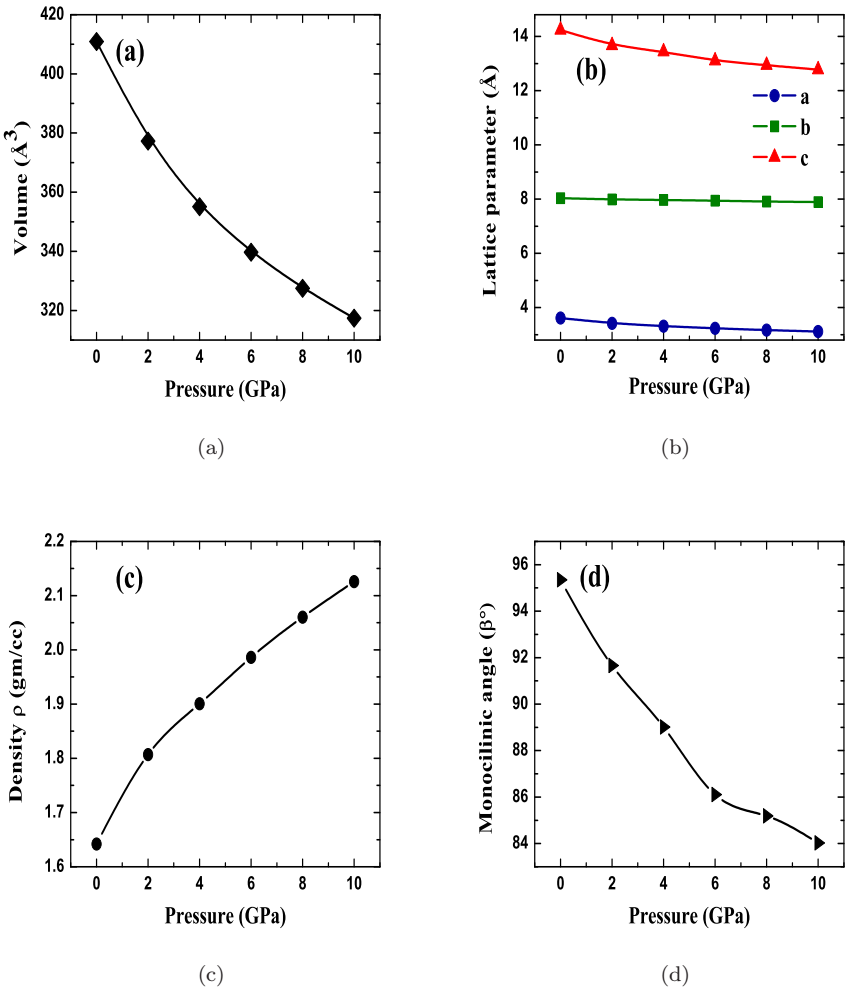

(a) (b) (c) (d)

FIGURE 7.2: Pressure dependance of solid G-MNAT (a) variation of lattice parameters with pressure (b) density as function of pressure (c) and pressure dependance of monoclinic angle (d).

and least compressible along b-axis. From this we conclude that the compressibility of G-MNAT lattice is anisotropic. In Figure 7.2 (c), the variation of the crystal density, ρ (gm/cc) with pressure is shown. Clearly, ρ increases with pressure (as volume decreases) which indicates that the inter molecular interactions enhance under pressure and thereby the lattice become more stiffer at high pressure. The monoclinic angle decreases with pressure to a value of 84.02^0 at 10 GPa as shown in Figure 7.2 (d).

The calculated equation of state of solid G-MNAT can be used to obtain the bulk modulus, B_0, and its pressure derivative B_0' by fitting the pressure-volume data to the Murnaghan's equation of state. The calculated values of B_0 and B_0' are found to be 15.3 GPa and 4.657, respectively and are presented Table 7.1. Although G-MNAT is a soft material due to low B_0 value but when compared to the bulk modulus value of other high energetic solids, for example, B_0 = 9.1 GPa for PETN [24], B_0 = 11.9 GPa for RDX [25], B_0 = 12.5 GPa for HMX [26], B_0 = 14.6 GPa for TAG-MNT [27], G-MNAT is stiffer material.

7.3.2 Vibrational properties

The vibrational properties are calculated within the framework of density functional perturbation theory (DFPT) [28–30]. We use norm-conserving pseudo potentials for the calculation of zone-center phonon frequencies with an energy cut-off of 800eV. The Brillouin zone integration is performed for 5x3x2 grid of k-points. The unit cell of the solid G-MNAT contains 46 atoms giving rise to a total of 138 vibrational modes. The $P2_1$ space group, which describes the monoclinic symmetry, has two irreducible representations namely, A and B. A group-theoretical analysis gives the following decomposition of vibrational representation into its irreducible components at the Γ-point: Γ-tot = 69A + 69B. Out of these modes, three (A + 2B) are acoustic modes and the remaining 135 modes are optical modes. All these modes are found to be both infrared and Raman active.

The calculated vibrational frequencies along with irreducible representation and mode assignment are presented in Table 7.2, Table 7.3 and Table 7.4 respectively. The vibrational modes that are situated between the frequency range from 74.2 cm^{-1} to 188.2 cm^{-1} are due to the collective vibrations from the cation and anion, thus these modes are designated as lattice modes and are presented in Table 7.2. The modes that involve vibrations of the internal molecular geometry of cation and anion are in between the frequency range from 192.8 cm^{-1} to 1687.9 cm^{-1} and are given in Table 7.2 and Table 7.3. The wagging vibrations of NH_2 cation are lying at 192.8 cm^{-1}, 223.5 cm^{-1}, 523.8 cm^{-1} to 633.8 cm^{-1} and at 774.2 cm^{-1}. The modes situated at 715.2 cm^{-1} and 715.8 cm^{-1} are due to the wagging of the N=C of anion. The stretching vibrations of tetrazole ring are found to present between

TABLE 7.2: The vibrational frequencies (cm^{-1}) of G-MNAT crystal calculated within PBE+G06 functional. Here LM represents lattice mode vibrations, ω, δ, ρ stands for wagging, bending, and rocking of the modes respectively.

Freq	IrrRep	Mode Assignment	Freq	IrrRep	Mode Assignment
74.2	A	LM	188.2	A	
78.3	A		192.8	A	ω NH_2
83.9	B		195.3	B	
87.7	A		212.2	B	ω NH_2, ρ CH_3
94.8	B		218.5	B	
99.7	A		223.5	A	
106.3	B		240.4	A	
108.5	A		244.1	B	
116.1	B		256.6	A	
118.4	A		257.5	B	
133.5	B		348.1	B	
137.5	A		354.6	A	
141.9	B		383.7	A	ρ NH_2, δ N=N-N
145.9	A		384.5	B	
146.9	B		425.5	B	δ NH_2
152.9	A		437.7	A	
154.9	B		445.8	A	
167.3	B		447.2	B	
168.5	A		465.8	B	
174.2	B		468.1	A	ω NH_2, ω CH_3, δ N=N-N
178.5	A				

1011.3 cm^{-1} to 1027.8 cm^{-1} which are in good agreement with the experimental observed range of 1011 cm^{-1} to 1026 cm^{-1}. The -C=N stretching vibration of the tetrazole ring is calculated to be 1687.9 cm^{-1}, which is in good agreement with experimental frequency of 1698 cm^{-1}. The other important vibrational modes are due to the C-H stretching vibrations of the methyl group attached to the tetrazole ring and N-H stretching vibrations of the amino groups of the cation.

The calculated stretching vibration frequencies of C-H and N-H modes G-MNAT are presented in Table 7.4. According to experiment [8], the C-H stretching modes are situated at 2956 cm^{-1} to 2970 cm^{-1} while the symmetric and asymmetric stretching of N-H modes are observed in the range from 3238 cm^{-1} to 3484 cm^{-1}. From the present PBE+G06 calculations, we find the frequency of stretching of

TABLE 7.3: The vibrational frequencies (cm^{-1}) of G-MNAT crystal calculated within PBE+G06 functional. The symbols ν, ω, δ, ρ stands for stretch, wagging, bending, and rocking of the modes respectively. IR-irreducible representation MA-mode assignment

Freq	IR	MA	Freq	IR	MA
523.8	A	ω NH_2	1177.1	B	ν N-N, ω NH_2
532.8	B		1180.4	A	
557.6	A		1189.6	B	
567.4	B		1190.7	A	δ ring
585.8	A		1198.8	B	
600.1	B		1199.1	A	
606.6	A		1235.9	B	δ N-CH_3, δ C=N-N
633.8	B		1236.1	A	
643.3	B	δ N-C-N, δ C-N-N	1297.1	B	δ NO_2, δ N-CH_3
650.9	B	δ N=N-N, δ N-N-C	1303.1	A	ν NO_2, ν N=N
657.3	A		1315.4	B	
683.8	A	δ N-C-N, ω NH_2	1318.1	A	
687.2	B		1330.5	A	ω NH_2, δ C-N-N
704.9	B		1332.1	B	
715.2	A	ω N=C	1350.6	A	δ N-C-H, ν C-N
715.8	A		1357.9	B	
716.7	B	ν N-C-N,δ NO_2	1408.2	B	
727.5	B		1421.9	A	δ C-N-N, ω NH_2
727.6	A		1435.7	B	
729.1	A		1445.4	A	
730.6	B		1451.3	A	δ N-C-H, ν C-N
774.2	A	ω NH_2	1452.8	B	
797.6	B		1463.8	A	
848.1	B	ν N-C-N,ν C=N,ν N-CH_3,	1464.3	B	
854.4	A		1554.9	B	ν C=N
864.4	A		1555.8	A	
864.6	B		1574.9	A	δ NH_2, δ C=N-N
977.9	A	ν C-N, ρ NH_2	1577.5	B	
978.8	B		1608.1	A	
995.9	A		1656.1	B	δ NH_2, ν C-N, δ C-N-H
996.9	B		1666.6	B	
1010.3	A	ν N-N, ν NO_2, ω C-H	1672.6	A	
1010.5	B	δ N-C-N, ω NH_2	1678.9	B	
1027.8	A		1687.9	A	ν C=N
1030.6	B				
1066.5	B				
1069.4	A	ν N-N, ω C-NH_2			
1078.6	B				
1091.5	A				
1109.7	A				
1110.7	B				

TABLE 7.4: The stretching vibrational frequencies (cm^{-1}) of C-H and N-H modes of G-MNAT crystal calculated within PBE+G06 functional.

Freq	IrrRep	Mode Assignment
2963.5	A	ν_{sym} C-H
2965.1	B	
3051.2	B	
3051.9	A	
3056.9	B	
3062.8	A	
3077.3	B	
3078.1	A	
3140.9	B	ν_{asy} C-H
3143.8	A	
3180.8	B	
3196.7	A	
3242.8	B	ν_{sym} N-H
3246.9	A	
3279.9	A	
3316.7	B	ν_{asy} N-H
3473.4	A	
3483.3	B	

C-H modes are situated between 2963.5 cm^{-1} to 3196.7 cm^{-1}. On the other hand, symmetric stretching frequencies of N-H mode of cation are found to present between 3242.8 cm^{-1} to 3279.9 cm^{-1} and the asymmetric stretching N-H modes are situated at 3316.7 cm^{-1} to 3483.3 cm^{-1}. Overall, the present study of vibrational properties based on dispersion corrected density functional PBE+G06 could reproduce well the observed vibrational frequencies of G-MNAT crystal. This confirms the fact that vdW corrected density functionals are essential to compute the structural and vibrational properties of solid energetic systems.

7.4 Conclusions

In conclusion we have studied crystal structure, equation of state, electronic structure and vibrational properties of solid G-MNAT. We found that PBE+G06 functional gives accurate structural results when compared to CA-PZ, PBE and

PBE+TS functionals. The optimized crystal structure with the PBE+G06 functional was then used for the calculation of electronic band structure and vibrational properties. We found that the compressibility of solid G-MNAT is anisotropic and the lattice is more compressible along a-axis and least compressible along b-axis. The complete zone-center frequencies are calculated and each mode was assigned according to their molecular vibration. The calculated vibrational frequencies are in good agreement with experimental data. The present study confirms that dispersion corrected density functionals are efficient to describe the structural and vibrational properties of energetic solids.

References

[1] J. P. Agrawal, High Energy Materials, Propellants, Explosives and Pyrotechniques, Wiley-VCH Verlag, Germany.

[2] Thomas M Klapötke, Chemistry of High Energy Materials, (2011).

[3] J. Akhavan, The Chemistry of Explosives,(2011) Royal Society of Chemistry: Cambridge, UK.

[4] H. D. Fair, and R. F. Walker, Energetic Materials, vol 1, (1977) Plenum Press, New York.

[5] D. M. Badgujar, M. B. Talawar, S. N. Asthana, P. P. Mahulikar, J. Hazard. Mater 151 (2008) 289–305.

[6] M. B. Talawar, R. Sivabalan, T. Mukundan, H. Muthurajan, A. K. Sikder, B. R. Gandhe and A. S. Rao, J. Hazard. Mater 161 (2009) 589-607. 2009, 161, 589–607.

[7] M. I. Eremets, A. G. Gavriliuk, I. A.Trojan, D. A. Dzivenko, , R. Boehler, Nat. Mater 3 (2004) 558.

[8] T. Fendt, N. Fischer, T. M. Klapotke, J. Stierstorfer, Inorganic Chemistry 50 (2011) 1447.

[9] I. I. Oleynik, M. Conroy, S. V. Zybin, L. Zhang, A. C. van Duin, W. A. Goddard III, C. T. White, Shock Compression of Condensed Matter CP 845 (2005) 573.

[10] W. F. Perger, S. Vutukuri, Z. A. Dreger, Y. M. Gupta, K. Flurchick, Chem. Phys. Lett 422 (2006) 397-401.

[11] W.F. Perger, J. Zhao, J. M. Winey, Y. M. Gupta, Chem. Phys. Lett 428 (2006) 394-399.

[12] E. F. C. Byrd, B. M. Rice, J. Phys. Chem. C 111 (2007) 2787.

[13] E. F. C. Byrd, G. E. Scuseria, C. F. Chabalowski, J. Phys. Chem. B 108 (2004) 13100.

[14] D.C. Sorescu, B. M. Rice, J. Phys. Chem. C 114 (2010) 6734.

[15] S. Grimme, J. Comp. Chem. 27 (2006) 1787.

[16] A. Tkatchenko, M. Scheffler, Phys. Rev. Lett 102 (2009) 073005.

[17] W. Zhu, H. Xiao, Struct. Chem 21 (2010) 657-665.

[18] M. Segall, P. Lindan, M. Probert, C. Pickard, P. Hasnip, S. Clark, M. J. Payne, J. Phys.: Cond. Matt. 14 (2002) 2717.

[19] D. Vanderbilt, Phys. Rev. B. 41 (1990) 7892.

[20] D. M. Ceperley, B. J. Alder, Phys. Rev. Lett. 45(1980) 566.

[21] J. P. Perdew, A. Zunger, Phys. Rev. B. 23 (1981) 5048.

[22] J. P. Perdew, K. Burke, M. Ernzerhof, Phys. Rev. lett. 77 (1996) 3865.

[23] H. J. Monkhorst, J. Pack, Phys. Rev. B. 13 (1976) 5188.

[24] M. W. Conroy, I. I. Oleynik, S. V. Zybin, C. T. White, Phys. Rev. B 77 (2008) 094107.

[25] J. J. Haycraft, L. L. Stevens, C. J. Eckhardt, J. Chem. Phys 124 (2006) 024712.

[26] H. L. Cui, G. F. Ji, X. Chen, W. Zhu, F. Zhao, Y. Wen, D. Wei, J. Phys. Chem. A 114 (2010) 1082-1092.

[27] R. S. McWilliams, Y. Kadry, M. F. Mahmood, A. F. Goncharov, J. C. Jenkins, J. Chem. Phys 137 (2012) 054501.

[28] X. Gonze, Phys. Rev. B. 55 (1997) 10337.

[29] K. Refson, P. R. Tulip, S. J. Clarke, Phys. Rev. B. 73 (2006) 155114.

[30] S. Baroni, S. de Gironcoli, A. Dal Corso and P. Giannozzi, Rev. Mod. Phys. 73 (2001) 515.

Chapter 8

Summary and Future direction

The goal of this thesis was to explore the fundamental physical properties such as structural, elastic, electronic, optical and vibrational properties of nitrogen based energetic materials alkali, alkaline-earth metal azides and alkali metal amides. We have also studied the effect of hydrostatic pressure on these properties for lithium azide and potassium azide. In addition, the equation of state and vibrational properties of nitrogen rich secondary energetic material G-MNAT was also studied. All the calculations were carried out with advanced density functional theory methods. The calculated results are in good agreement with experiment and we strongly believe that the calculated results are accurate predictions where the experimental data are not available. The main results of the thesis work are summarized as follows:

We have studied the role of van der Waals interactions in describing the crystal structure of alkali, alkaline-earth metal azides, alkali metal amides and G-MNAT. Our study found that although the studied materials are ionic solids, the vdW interactions play a major role in crystal binding and the structure related properties computed using PBE+G06 functional are in good agreement with experiment compared to standard CA-PZ and PBE functionals. The present study on alkali metal amides confirms that the vdW interactions is more predominant in $LiNH_2$ when compared to the other metal amides. In the case of G-MNAT crystal, the

vdW interactions are predominant and thus confirming the importance of dispersion corrected density functionals to describe the secondary energetic molecular solids.

The electronic band structure of alkali, alkaline-earth metal azides and alkali metal amides are calculated and found that all the studied materials are wide band gap insulators. The calculated band gaps are improved to a greater extent by using the recently developed TB-mBJ functional which is known to give accurate band gaps that are in good accord with experiment. There are no experimental band gaps available to compare the present results. The study of density of states reveals that the 'p'-states of end nitrogen atom are dominant at Fermi level in case of alkali and alkaline-earth metal azides with no overlap of metal atom states in the valence band region implying that the bonding in these materials is predominantly ionic. Whereas in the case of alkali metal amides, the 'p'-states of nitrogen atom and also a minor contribution of the 's'-states of metal atom are present at the Fermi level. There is a strong hybridization of 's'-states of hydrogen atom and the states from nitrogen atom in the deep valence band region. These facts reveals that the bonding in the metal amides is predominantly ionic with small covalent nature.

The optical properties such as complex di-electric function, refractive index, optical absorption and photoconductivity are also calculated. Alkali metal azides and alkaline-earth metal azides have broad photo response over a broad spectrum in ultra-violet light. In the case of alkali metal amides, the calculated optical properties show a strong optical anisotropy. The elastic constants and thereby the bulk mechanical properties of alkali, alkaline-earth metal azides and alkali metal amides are calculated and found that all are mechanically stable. Among the alkali metal azides, LiN_3 is found be stiffer material while $Ca(N_3)_2$ is stiffer in the case of alkaline earth metal azides. Overall among the studied metal azides, $Ca(N_3)_2$ is stiffest material. In the case of alkali metal amides, $LiNH_2$ is found to be stiffer with large elastic moduli.

The high pressure behavior of monoclinic LiN_3 and tetragonal KN_3 are studied and found that the calculated P-V relation for both the compounds is well

reproduced by calculations including the DFT+D correction. The present study clearly show that the compressibility of the materials is anisotropic which is also consistent with experiment. As pressure increases the band gap decreases implying possibility to become semiconductor which is a precursor for the formation of polymeric nitrogen. The total and partial density of states of LiN_3 and KN_3 are also supporting this fact. As pressure increases the states broaden implying the delocalization of the azide ion states which is also a witness towards the formation of polymeric nitrogen. In addition, the equation of state and vibrational frequencies of nitrogen rich secondary energetic material G-MNAT is studied. The compressibility of the material is found to be anisotropic. The computed bulk modulus from the equation of state indicates that the material is stiffer than the known high explosives RDX, HMX. The calculated vibrational frequencies are in good accord with available experimental data.

The present work gives a broad understanding of the important physical properties of the metal azides, amides and G-MNAT. The potential application of the studied metal azide compounds is towards the synthesis of single bonded networks of nitrogen under high pressures. In this work we could able to study the high pressure behavior of LiN_3 and KN_3 up to limited pressure range. In practice it is required to go even high pressures to see the structural stability and the ability of formation of single bonded networks of nitrogen of the all the metal azides. We believe this would be a potential future direction for further studies on metal azides. In most of the organic and inorganic energetic materials, the decomposition of the material starts from the region called 'hot spots' which are nothing but the defect area of the crystalline lattice. So to understand the microscopic mechanism of decomposition of the energetic solids it is required to have more studies on defect structures. The changes brought in electronic structure and bonding would be required. We leave this topic for future studies on the metal azides and amides.